Statistical Characterization of UWB Channels for Wireless Personal Area Networks Applications

Javier Dacuña Santos

Supervisor: prof. dr. ir. Gerard J.M. Janssen
Mentor: ir. Zoubir Irahhauten

TUDelft
Delft University of Technology

UPC epsc Escola Politècnica Superior de Castelldefels
UNIVERSITAT POLITÈCNICA DE CATALUNYA

Statistical Characterization of UWB Channels for Wireless Personal Area Networks Applications

Master's Thesis in Electrical Engineering

Wireless Mobile Communications group
Electrical Engineering, Mathematics, and Computer Science
Technische Universiteit Deflt

Javier Dacuña Santos
Universitat Politècnica de Catalunya

25th August 2005

Author

Javier Dacuña Santos

Title

Statistical Characterization of UWB Channels for Wireless Personal Area Networks Applications

MSc presentation

24th August 2005

Graduation Committee

Dr. ir. G. J. M. Janssen
Technische Universiteit Deflt

Ir. Z. Irahhauten
Technische Universiteit Deflt

Dr. ir. H. Nikookar
Technische Universiteit Deflt

Abstract

Ultra Wide Band is a new technology, which has been recently introduced for wireless communications systems. The restrictions in the maximum radiated power imposed by the FCC makes this technology suitable for Wireless Personal Area Networks (WPAN). Design and implementation of UWB systems for WPAN application need accurate channel models and a good understanding of the propagation characteristics of the UWB radio channel. For some applications like in WPAN, the distances between the transmit and the receive antenna can be very small. Thus a serious problem has to be mentioned namely, that the far field conditions of the antennas may be not satisfied. Different effects as extra losses, higher fields or pulse waveform distortion may appear and they have to be taken into account. This thesis wants to present an analysis of the near field effect for UWB systems by investigating two important parameters: link budget and pulse shape. Derivations are carried out in order to model these parameters. Simulations using several electromagnetic simulator are performed and compared with the derivations and measurements. Finally a set of time domain measurements for very small distances between transmit and receive antennas is performed. The link budget and pulse shape is analyzed in the measurements as well as the most important channel parameters.

Ultra Wide Band es una tecnología introducida recientemente para comunicaciones. Las restricciones en la máxima potencia radiada impuestas por la FCC hace que UWB sea una tecnología apta para redes de área personal (WPAN). El diseño e implementación de sistemas UWB para redes de área personal precisa de un buen conocimiento de las características de propagación del canal. Para algunas aplicaciones, la distancia entre las antenas puede ser muy pequeña y esto lleva a tener que analizar un serio problema, concretamente, las condiciones de propagación de campo lejano de las antenas pueden no cumplirse. Varios efectos como pérdidas extras o distorsiones para distancias muy cortas pueden producirse y tienen que ser analizados. El objetivo principal de esta tesis es analizar los efectos de campo cercano para sistemas UWB investigando principalmente dos parámetros: pérdidas del enlace y distorsión. El análisis de dichos efectos se ha llevado a cabo analíticamente y mediante simulaciones para luego ser comparado con las medidas realizadas. Las pérdidas en el enlace, distorsiones y otros parámetros importantes del canal han sido extraídos y analizados.

To my girlfriend

Preface

The requirements of high data rate connections between mobile devices as telephones, PDA and laptops for short distances are becoming more and more necessary.

UWB technology combines all the necessary features to be used in such applications, namely, high data rates, low consumption, relatively low cost, etc. In order to use UWB technology in such applications, the radio channel for short distances has to be characterized accurately.

The investigation of the UWB radio channel for very short distances in order to achieve an accurate channel model will allow a better design and implementation of UWB systems.

This thesis presents the results of the work performed at Delft University of Technology (TU Delft) during six months as a part of my MSc degree.

I would like to express my sincere gratitude to all who have given me the opportunity to carry out my work, finishing my MSc degree at Delft University of Technology.

First and foremost, I am deeply grateful to my mentor ir. Zoubir Irahhauten, for helping me wherever needed.

I would like to thank also my supervisor dr. ir Gerard J. M. Janssen for his useful advices and corrections of my work.

I am also grateful to dr. ir. Homayoun Nikookar for his corrections and comments about this thesis.

Finally I want to thank my family for encouraging me with their unconditional support during all my student life.

Javier Dacuña Santos

Delft, The Netherlands

25th August 2005

Contents

Preface **vii**

List of figures **xiii**

List of tables **xix**

List of symbols **xxi**

1 Introduction **1**

1.1 UWB definition 1

1.2 State of the art 3

1.3 Objectives of the thesis 3

1.4 Thesis framework 4

2 UWB overview **5**

2.1 UWB channel modelling 5

2.1.1 Channel model 6

2.1.2 Parameters 6

2.2 UWB antennas 10

2.2.1 Electric and magnetic antennas 11

2.2.2 Constant gain vs. constant aperture 11

2.2.3 Regions of radiation 12

3 Near field effects **17**

3.1 Multiple reflections between antennas 17

3.1.1 Reradiated power 19

3.1.2 Model of mutual coupling between antennas for narrow-band signals 20

3.1.3 Extension of the model for UWB 24

3.1.4 Simulations 29

3.2 Phase error 34

3.2.1 Phase error for a dipole 35

3.2.2 Phase error between two dipoles 42

3.2.3 NEC simulations for a wire-simulation bi-conical antenna 52

3.2.4 Real measurements 52

3.2.5 XFDTD simulation for a planar diamond antenna 54

3.3 Radiating and reactive fields 55

3.3.1 Differences between radiating and reactive fields 56

3.3.2 Simulations of a diamond antenna 58

3.4 Conclusions 58

4 Models **61**

4.1 Link budget model 61

4.1.1 Simulations 62

4.2 Multipath reception 66

4.2.1 Far field reflections 66

4.2.2 Near field reflections 68

4.2.3 Model 71

5 Measurements **73**

5.1 Link budget measurements 73

5.1.1 Big bi-conical antenna 73

5.1.2 Middle bi-conical antenna 75

5.1.3 Small bi-conical antenna 75
5.2 Pulse shape 76
5.2.1 Big antenna pulse shape distortion 76
5.2.2 Middle antenna pulse shape distortion 77
5.2.3 Small antenna pulse shape distortion 79
5.3 Data processing 80
5.4 Channel measurements 80
5.4.1 Path loss 80
5.4.2 K-factor 87
5.4.3 RMS delay spread 92

6 Conclusions and Future Work 97
6.1 Conclusions 97
6.2 Future Work 98

Bibliography 99

A Algorithms comparison 101
A.1 Introduction 101
A.2 Algorithms description 102
A.2.1 ESPRIT algorithm 104
A.2.2 CLEAN algorithm 106
A.2.3 INV+CLEAN algorithm 106
A.3 Simulations 107
A.3.1 Coarse multipath without noise 107
A.3.2 Coarse multipath with noise 112
A.3.3 Dense multipath without noise 116
A.3.4 Dense multipath with noise 122
A.4 Conclusions 128

List of Figures

1.1 UWB spectral mask 2

2.1 Fading effect illustration 7

2.2 Time decay constant 7

2.3 Dispersive antennas 10

2.4 Radiation regions for phase error criterion 12

2.5 Derivation of the far-field criterion 13

2.6 Critical frequency for phase error criterion 13

2.7 Critical distance for phase error criterion 14

2.8 Radiation regions for radian-distance criterion 15

2.9 Radiation regions for radian-distance criterion 15

3.1 Antenna terminated in impedance Z_t and its equivalent circuit . . . 18

3.2 Multiple reflections between two antennas 18

3.3 Multiple reflections between antennas 21

3.4 Multiple reflections between antennas, convergence condition . . 23

3.5 Power received as a function of the distance 24

3.6 Power received as a function of the frequency 24

3.7 Two ports model of the antennas 25

3.8 Transfer function as a function of frequency for several distances . 27

3.9 Differences with Friis transmission equation 28

3.10 Continuous transition of the transfer function vs. distance 28

3.11 Continuous transition of the transfer function (phase shift of $\pi/4$. 29

3.12 Received waveform distortion 30

3.13 Resonances in the channel transfer function 30

3.14 Received time domain waveform 31

3.15 Gain of the antenna vs. frequency 31

3.16 Received waveform with measured antennas 32

3.17 Structure of the simulated diamond antenna 33

3.18 Reflection coefficient and gain of the diamond antenna 33

3.19 Received pulses for different distances 34

3.20 Receive dipole 35

3.21 Uniform current distribution dipole 36

3.22 Sinusoidal current distribution dipole 37

3.23 Radiation pattern distortion 37

3.24 Electric and magnetic fields from a dipole 38

3.25 Magnitude of the electric field vs. frequency normalized to the distance 39

3.26 Magnitude of the magnetic field vs. frequency normalized to the distance 40

3.27 Comparison between calculated and simulated data 40

3.28 Current (magnitude) distribution along the dipole 41

3.29 Current (phase) distribution along the dipole 41

3.30 Phase error between two dipoles 42

3.31 Open-circuit voltage at the receive antenna 44

3.32 Schematic of the simulations in NEC 44

3.33 Equivalent circuit for the coupling between two antennas 45

3.34 Comparison between the open-circuited voltages simulated and calculated 46

3.35 Normalized received power vs. distance at 937.5 MHz 46

3.36 Normalized received power vs. distance at 2.5 GHz 47

3.37 Power received vs. distance and frequency 47

3.38 Normalized received power vs. distance 48

3.39 Normalized spectrum of the Gaussian pulse 48
3.40 Normalized received power vs. distance for different pulses 49
3.41 Normalized spectrum of the pulses 49
3.42 Reflection coefficient and gain of bi-conical antenna 51
3.43 Electric field expansion 51
3.44 Received power as a function of the frequency for several distances 52
3.45 Normalized frequency response for several distances 53
3.46 Normalized power vs. distance 53
3.47 Comparison between measured and simulated received power . . 54
3.48 Model used in the NEC simulations 54
3.49 Normalized received power vs. distance for diamond antennas . . 55
3.50 Radiating and reactive terms vs. distance 57
3.51 Variations of the reflection coefficient as a function of the distance between atennas 58
3.52 Comparison between bi-conical antennas of different sizes 59
3.53 Comparison between two different resonant dipoles 60

4.1 Simulation vs. model 62
4.2 L_{nf} for different antenna sizes 62
4.3 Bi-conical antennas dimensions 63
4.4 Phase error effect for different antennas sizes and a single frequency 63
4.5 Simulations and exponential model for different antenna sizes . . 64
4.6 τ_d as a function of the antenna size 65
4.7 Comparison between measurement, simulation and model 65
4.8 Far field reflections 67
4.9 Near field reflection 68
4.10 Incident and reflected angle 69
4.11 Multiple division of the reflecting object 69
4.12 Near field reflection situation 71

5.1 Situation of the antennas 74

5.2 Normalized received power as a function of the distance 74
5.3 Normalized received power as a function of the distance 75
5.4 Normalized received power as a function of the distance 76
5.5 Time domain distortion 76
5.6 Frequency domain distortion 77
5.7 Time domain distortion 78
5.8 Frequency domain distortion 78
5.9 Time domain distortion 79
5.10 Frequency domain distortion 79
5.11 Relative received power vs. distance 81
5.12 Exponential path loss model 82
5.13 Path loss exponent vs. bandwidth 83
5.14 Path loss exponent vs. frequency 83
5.15 Relative received power vs. distance 84
5.16 Path loss exponent vs. bandwidth 85
5.17 Path loss exponent vs. frequency 86
5.18 Relative received power vs. height 86
5.19 Relative received power vs. distance 87
5.20 Path loss exponent vs. bandwidth 88
5.21 Path loss exponent vs. frequency 88
5.22 CDF of the K factor 89
5.23 Variation of the K factor vs. distance 89
5.24 CDF of the K factor 90
5.25 Variation of the K factor vs. distance 90
5.26 CDF of the K factor 91
5.27 Variation of the K factor vs. distance 91
5.28 CDF of the RMS delay spread 92
5.29 Variation of the RMS delay spread vs. distance 93
5.30 CDF of the RMS delay spread 93

5.31 Variation of the RMS delay spread vs. distance 94

5.32 CDF of the RMS delay spread 94

5.33 Variation of the RMS delay spread vs. distance 95

A.1 Simulation of the channel response 102

A.2 Frequency domain of the channel response 103

A.3 Problem of the inverse filtering algorithm 103

A.4 CDF of RDS for coarse multipath, no noise and 50 dB threshold . 107

A.5 CDF of K factor for coarse multipath, no noise and 50 dB threshold 108

A.6 CDF of number of paths for coarse multipath, no noise and 50 dB threshold 108

A.7 CDF of total power for coarse multipath, no noise and 50 dB threshold 109

A.8 RDS vs. threshold for coarse multipath and no noise 109

A.9 K factor vs. threshold for coarse multipath and no noise 110

A.10 Number of paths vs. threshold for coarse multipath and no noise . 110

A.11 Total power vs. threshold for coarse multipath and no noise 112

A.12 CDF of RDS for coarse multipath, with noise and 50 dB threshold 112

A.13 CDF of K factor for coarse multipath, with noise and 50 dB threshold 113

A.14 CDF of number of paths for coarse multipath, with noise and 50 dB threshold 113

A.15 CDF of total power for coarse multipath, with noise and 50 dB threshold 114

A.16 RDS vs. threshold for coarse multipath with noise 114

A.17 K factor vs. threshold for coarse multipath with noise 115

A.18 Number of paths vs. threshold for coarse multipath with noise . . 115

A.19 Total power vs. threshold for coarse multipath with noise 116

A.20 CDF of RDS for dense multipath, without noise and 50 dB threshold 118

A.21 CDF of K factor for dense multipath, without noise and 50 dB threshold 118

A.22 CDF of number of paths for dense multipath, without noise and 50 dB threshold 119

A.23 CDF of total power for dense multipath, without noise and 50 dB threshold . . . 119

A.24 RDS vs. threshold for dense multipath and no noise . . . 120

A.25 K factor vs. threshold for dense multipath and no noise . . . 120

A.26 Number of paths vs. threshold for dense multipath and no noise . 121

A.27 Total power vs. threshold for dense multipath and no noise 121

A.28 CDF of RDS for dense multipath, with noise and 50 dB threshold 123

A.29 CDF of K factor for dense multipath, with noise and 50 dB threshold 123

A.30 CDF of number of paths for dense multipath, with noise and 50 dB threshold . . . 124

A.31 CDF of total power for dense multipath, with noise and 50 dB threshold . . . 124

A.32 RDS vs. threshold for dense multipath with noise . . . 125

A.33 K factor vs. threshold for dense multipath with noise . . . 125

A.34 Number of paths vs. threshold for dense multipath with noise . . . 126

A.35 Total power vs. threshold for dense multipath with noise 126

List of Tables

5.1 Measurement description 81

A.1 Simulation results for coarse multipath without noise 111
A.2 Simulation results for coarse multipath with noise 117
A.3 Simulation results for dense multipath without noise 122
A.4 Simulation results for dense multipath with noise 127

List of Symbols

η	Free space impedance
Γ	Reflection coefficient
γ	Path loss exponent
Λ	Cluster arrival rate
λ	Wavelength
$\mathscr{E}$	Instantaneous electric field
$\mathscr{H}$	Instantaneous magnetic field
$\mathscr{W}$	Instantaneous Poynting vector
ω	Angular frequency
ϕ	Azimuth angle with respect to the x-axis
σ	Scattering cross section
τ_d	Distance decay constant
τ_{rms}	RMS delay spread
θ	Elevation angle with respect to the z-axis
A	Antenna apperture
a	Amplitude of the multipath components
A_{eff}	Effective area of the antenna
BW	Bandwidth of the signal
c	Speed of light
D	Largest antenna dimension

d	Distance
d_0	Reference distance
E	Electric field
f	Frequency
f_c	Center frequency
f_H	Highest frequency
f_L	Lower frequency
G	Gain
G_{RX}	Gain of the receive antenna
G_{TX}	Gain of the transmit antenna
H	Magnetic field
h	Channel impulse response
I	Intensity
I_0	Current at the feed point
K	Rician K factor
k	Wave number
l	Length of a dipole
L_{nf}	Near field losses
P	Power delay profile
p	Pulse shape
P_{ant}	Power dissipated in the antenna impedance
P_{load}	Power dissipated in the load impedance
P_{rad}	Radiated power
P_{RX}	Received power
P_{TX}	Transmitted power
PL	Path loss
r	Radial distance

R_L	Loss resistance
R_r	Radiation resistance
R_t	Real part of Z_t
R_A	Real part of Z_A
S_i	Incident power flux
t	Time
V	Voltage
W	Poynting vector
Z_0	Reference impedance
Z_A	Antenna impedance
Z_t	Terminal impedance
Z_m	Mutual impedance

Chapter 1

Introduction

UWB is a technique that has received a lot of attention recently. It is based (usually) on the transmission of very short pulses that leads to a very wide spectrum. This in turn allows a low power spectral density.

One of the benefits of UWB is that due to its low power spectral density, it is able to share the spectrum with other narrowband or wideband systems. It allows a very high data rate for communications. Due to its high time resolution the self-interference in an UWB network is very low. Another related benefit is that UWB is very tolerant to multipath fading. Also UWB can provide very accurate position and ranging (even $<$ 1 cm).

These are only some of the benefits that UWB can provide but it also has disadvantages. Some of the disadvantages are that even with its low power spectral density, UWB may cause or suffer interference to/from other systems, and it needs an accurate time synchronization.

This chapter is organized as follows. Section 1.1 gives an introduction of UWB technology. Section 1.2 presents the current state of the UWB channel modelling. Section 1.3 introduces the objectives of this work. Finally in section 1.4 the framework of this thesis is defined.

1.1 UWB definition

Ultra wideband usually describes a technology based on the transmission of very short duration pulses (from several tens of picoseconds to a few nanoseconds), with relatively low energy. This technology is also called “carrier-free” or “impulse” technology. However, the UWB definition proposed by the FCC[1] is any signal that occupies a bandwidth larger than 500 MHz or a fractional bandwidth larger than

---

[1] Federal Communication Commission

0.2. Thus UWB is any signal that fulfills the following condition, whether or not it has a carrier frequency.

$$BW \geq 500\ MHz, \text{or} \tag{1.1}$$

$$B_f = \frac{BW}{f_c} = 2\frac{f_H - f_L}{f_H + f_L} \geq 0.2, \tag{1.2}$$

where f_H and f_L are the highest and the lowest frequency at -10 dB, BW is the signal bandwidth and f_c is the centre frequency.

This huge bandwidth allows a very high capacity, processing gains and large number of users. It has, also, other desirable capabilities like accurate location and ranging, lack of significant fading, high multiple access, covert communications, and material penetration. Due to its huge bandwidth, UWB has to share the spectrum with other narrowband systems and may cause or suffer interference. FCC has determined the EIRP[2] allowed [1] for each frequency band (see figure 1.1, where the solid line means the maximum radiated power measured with 1 MHz resolution and the dotted red line mean the maximum radiated power measured with 1 kHz resolution).

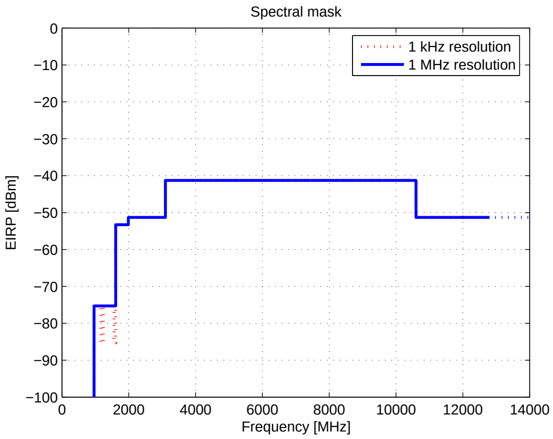

Figure 1.1: UWB spectral mask

Moreover, the base-band technology neither requires an IF stage in the receiver nor transmitter, and no mixers are needed. Nevertheless, UWB systems require a very accurate synchronization.

The main techniques used to generate UWB signals [2] are: time modulated UWB (TM-UWB) and direct sequence UWB (DS-UWB). The former is based on the transmission of very short pulses (mono-cycles) while the second one is based on a technique similar to CDMA. A pseudo-noise sequence is multiplied by an impulse sequence at a duty cycle approaching a sinusoidal carrier, providing spectrum spreading, channelization and modulation. However there are other techniques to generate UWB signals that are not based on impulse transmission as for example multi-band orthogonal frequency division multiplexing (MB-OFDM) based on the aggregation of several narrow band carriers.

---

[2] Effective Isotropic Radiated Power

UWB technology allows a very high data rate between two or more devices at short distances. An example of an application would be the data transmission between a digital camcorder and a personal computer. These kinds of applications are subject to place the devices very close to each other (distances even smaller than 20 cm). The fact that the devices are very close to each other means that the transmission between them can be within the near field region of the antennas. In most of the transmission models it is assumed that the far field condition of the antennas is fulfilled, so, for these kinds of applications, these models may not be valid.

1.2 State of the art

Several measurement campaigns have been reported in the literature in order to model the UWB channel for indoor scenrios. In [3] measurements for UWB channels in indoor scenarios are analyzed but not very short distances are covered. In [4] the human body effect in UWB signal propagation is investigated, but only for the receive antenna near the body and with transmit antenna in the far field. In [5] UWB channel measurements for a BAN[3] are presented where transmit and receive antenna are placed directly on the body and only 3-6 GHz bandwidth was measured.

No literature have been reported investigating the near field effects when the antennas are close to each other. UWB communications are suitable for short range communications and in such situations the antennas can be situated within the near field region of each other.

Design and implementation of UWB systems for WPAN applications needs accurate channel models for very short distances.

1.3 Objectives of the thesis

The effects of near field transmission are analyzed by investigating two important parameters, namely link budget and pulse shape.

---

[3] Body Area Network

Theoretical analysis, simulations and measurements are carried out in order to obtain a model to predict these effects.

Statistical methods based on real channel measurements for different scenarios are used in order to obtain the channel parameters to model the UWB short range channel.

The effect of the body in the UWB channel is analyzed based on measurements with a body obstructing the direct path.

Also different deconvolution algorithms are presented and tested with simulations in order to obtain the best one to be used in the performed measurements.

1.4 Thesis framework

This thesis is structured as follows:

Chapter 2: A brief overview about UWB channel modelling, presenting the most important parameters and models, is given. Also an introduction of the main types and characteristics of UWB antennas is presented.

Chapter 3: In this chapter, the different effects that can appear in the near field of the antennas are explained. These effects comprise multiple reflections between antennas, phase error and the reactive fields. Derivations in order to characterize the effects are done. Also conclusions about the repercussions of these effects in UWB transmission are given.

Chapter 4: This chapter presents some models of the behavior of the UWB channel for short distances.

Chapter 5: The results of a set of time domain measurements are presented in this chapter. These measurements comprise link budget measurements, pulse shape distortion measurements as well as channel measurements in order to characterize the statistical parameters of the channel. Also a BER performance comparison is presented to see the improvement of the BER as a function of the number of fingers using a Rake receiver.

Chapter 6: This chapter presents the conclusions extracted from the work carried out in this thesis. All the important concepts are reviewed. Also some advices for future related works are given.

Chapter 2

UWB overview

THis chapter wants to introduce the reader to some concepts about UWB channel modelling and antennas.

Different important parameters have to be known in order to model the UWB channel. These parameters are obtained from the channel impulse response and they measure the dispersion and attenuation suffered by the signal, among others.

On the other hand, antennas play a very important role in UWB communications due to their frequency dependent behavior. Also the behavior of the antenna may change as a function of the distance between transmit and receive antenna.

A brief description of UWB channel modelling and its main parameters is given in section 2.1. Section 2.2 presents an introduction of UWB antennas and their behavior.

2.1 UWB channel modelling

An accurate channel model is needed to design an UWB system and to predict maximum ranges and transmission rates.

There are several ways to characterize the UWB channel: deterministic and statistical methods. When the channel is influenced by some unknown factors, exact prediction with deterministic models is not possible. Statistical models are based on measurements and they give us the channel behaviour with some confidence interval.

2.1.1 Channel model

The impulse response of the channel at instant t, can be expressed as:

$$h(\tau,t) = \sum_{n=1}^{N(t)} a_n(t)\delta(\tau - \tau_n(t)), \tag{2.1}$$

where the parameters of the nth path a_n and τ_n are amplitude and delay and N is the number of relevant multipath components, respectively. τ indicates the delay. In the following sub-sections the parameters that characterize the channel will be presented.

2.1.2 Parameters

In this section some important parameters of the UWB channel are exposed.

Power delay profile (PDP)

The power delay profile (PDP) is the received power as a function of the excess delay. It is defined as:

$$P(\tau) = \sum_{n=1}^{N} a_n^2\delta(\tau - \tau_n), \tag{2.2}$$

where a_n is the coefficient of the nth multipath component and N is the number of relevant multipath components.

In common narrowband systems, the resolution in time is small, this means that we cannot resolve different multipath components arriving within a time less than $1/BW$ where BW is the bandwidth of the signal. The interference of several multipath components with different relative phase may be constructive or destructive causing multipath fading as illustrated in figure 2.1.

In UWB systems, the time resolution is higher due to its large bandwidth. Thus it is possible to resolve more multipath components and the likelihood of interference between two or more multipath components is lower than in narrowband systems. Therefore UWB systems are more robust to multipath fading than narrowband systems. The higher number of resolved multipath components is also important because the UWB receiver can take advantage of it, gathering several multipath components coherently (Rake receiver).

One parameter of the PDP is the time decay constant, τ . The time decay constant is a measure of the exponential decay of the power delay profile with the excess time delay. It is illustrated at figure 2.2.

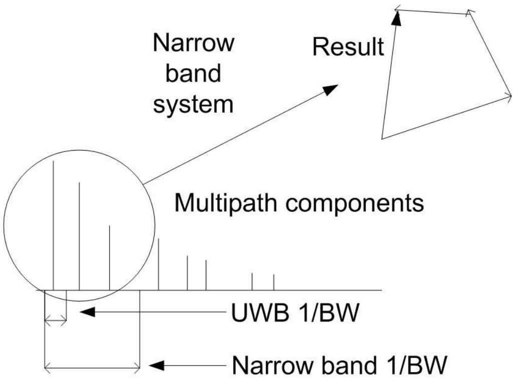
Narrow
band
system
Result
Multipath components
UWB 1/BW
Narrow band 1/BW

Figure 2.1: Time resolution of UWB and Narrowband systems and illustration of fading effect.

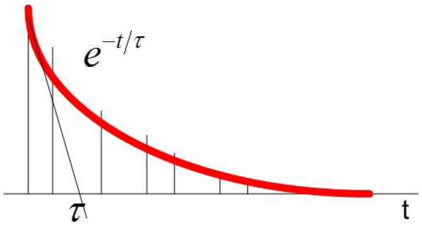

Figure 2.2: Time decay constant

In [6] it is reported that the time decay constant (TDC) seems to follow a log-normal distribution with mean of 39.8 ns and standard deviation of 1.27 dB (1.34 ns) in an office building. The same report shows a mean TDC of 29–35 ns and 41–56 ns for LOS[1] and NLOS[2], respectively.

Also the correlation between the time decay constant and the transmitter to receiver distance is investigated, but they conclude that it is in fact independent.

The time decay constant is important because it limits the maximum pulse rate that can be used without overlapping.

Another related parameter is the RMS[3] delay spread. The RMS delay spread (or RDS) is a measure of the amount of signal dispersion in the channel. RDS is defined as the square root of the second central moment of the power delay profile as:

$$\tau_{rms} = \sqrt{\overline{\tau^2} - \bar{\tau}^2}, \tag{2.3}$$

where:

$$\bar{\tau} = \frac{\sum_n a_n^2 \tau_n}{\sum_n a_n^2} = \frac{\sum_n P(\tau_n)\tau_n}{\sum_n P(\tau_n)}, \qquad \text{and} \tag{2.4}$$

$$\overline{\tau^2} = \frac{\sum_n P(\tau_n)\tau_n^2}{\sum_n P(\tau_n)}. \tag{2.5}$$

Several studies have shown that τ_{rms} increases with the transmitter to receiver distance [7]. Moreover, τ_{rms} is normally distributed with a standard deviation independent of the distance [7].

Time of arrival

In [8] a Saleh-Valenzuela (S-V) approach is used to model the time of arrival of the multipath components, showing multipath arriving in clusters. This is due to the clustering of the objects causing the multipath.

In this model "cluster arrival rates" and "ray arrival rates" are distinguished. The first cluster starts at time $t = 0$, and the following rays are arriving with a rate given by a Poisson process with rate λ.

Then, the impulse response is described as:

$$h_i(t) = X_i \sum_{l=0}^{L} \sum_{k=0}^{K} \alpha_{k,l}^i \delta(t - T_l^i - \tau_{k,l}^i), \tag{2.6}$$

---

[1] Line of Sight

[2] Non Line of Sight

[3] Root Mean Square

where $a^i_{k,l}$ are the multipath gain coefficients, T^i_l is the delay of the lth cluster, $\tau^i_{k,l}$ is the delay of the kth multipath component relative to the lth cluster arrival time (T^i_l) and i refers to the ith realization.

Defining:

- T_l, the arrival time of the first path of the lth cluster.
- $\tau_{k,l}$, the delay of the kth path within the lth cluster relative to the first path arrival time, T_l.
- Λ, the cluster arrival rate.
- λ, the ray arrival rate.

Then, the distribution of cluster and ray arrival time is:

$$p(T_l \mid T_{l-1}) = \Lambda \exp[-\Lambda(T_l - T_{l-1})], \qquad l > 0, \tag{2.7}$$

$$p(\tau_{k,l} \mid \tau_{(k-1),l}) = \lambda \exp[-\lambda(\tau_{k,l} - \tau_{(k-1),l})], \qquad k > 0. \tag{2.8}$$

The channel coefficients are defined as a product of small-scale and large-scale fading coefficients, and fit best the log-normal distribution rather than the Rayleigh distribution (that was used in the original S-V model). This is because the high time resolution (high bandwidth), reduces the likelihood of interference between two or more multipath components.

Path loss

Path loss generally increases exponentially with distance. The mean path loss for Tx-Rx separation distance of d is:

$$PL_{[dB]}(d) = PL_{[dB]}(d_0) + 10\gamma \log_{10}\left(\frac{d}{d_0}\right), \tag{2.9}$$

where d_0 is the reference distance and γ is the path loss exponent.

The path loss exponent is closely related with the environment.

In [9], a path loss exponent of 1.7 with standard deviation of 0.3 and 3.5 with standard deviation of 0.97 is exposed for LOS and NLOS scenarios respectively. The fact that the path loss exponent for LOS scenario was less than for the free space (path loss exponent of 2), is because the behavior of the channel is like in a wave guide; the power is not spreading out over a sphere.

In [10], a "Dual-Slope Powerloss" model is presented to model the path loss. In this model, a breakpoint d_{bp} is defined. This breakpoint separates the path loss in two regions. One of them, for distances smaller than d_{bp}, with slope of $-\Omega\, dB/dec$ and the other, for distances larger than d_{bp}, with slope of $-20\, dB/dec$ (free space). Where $\Omega/10$ is the path loss exponent of the first region and 2 is the path loss exponent of the second region.

2.2 UWB antennas

There are several kinds of antennas that cover huge bandwidth, like the band from 535 kHz to 1705 kHz of AM[4] (a fractional bandwidth greater than 1), but normally, this kind of antennas are "multi-narrowband" antennas instead of "ultra wide band" antennas optimized to receive a single coherent signal across their entire operating bandwidth.

The ideal UWB antenna would be an antenna capable to receive all frequencies with the same relative phase and gain, this means that the antenna behaviour has to be stable over the entire band, and it must have a linear phase to prevent pulse distortion. However the ideal antenna is not feasible and the system has to be tolerant to some imperfections.

For example, log-periodic antennas (typical broad band antenna) are dispersive, since, large components radiate low frequencies and small components radiate high frequencies. This causes a non-linear phase (not constant group delay) and a distortion of the pulse waveform [11]. Figure 2.3 shows the effect of a not constant group delay in the pulse waveform when a Gaussian pulse is sent.

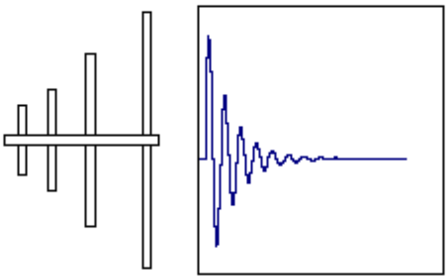

Figure 2.3: Illustration of the dispersive waveform of log-periodic antennas

Moreover, this distortion can be different for different angles of radiation. This kind of antenna is suitable to receive or transmit several different channels within a large bandwidth, but not a single channel with a large bandwidth.

---

[4] Amplitude Modulation

There are several kinds of antennas suitable for UWB indoor communications systems like the bow-tie, diamond, butterfly and vivaldi antennas. Frequency independent antennas like spiral and sinuous are also appropriate for this application. The principal characteristics of these antennas are their compact size and large bandwidth.

Other antennas, like the bi-conical and discone, have a large bandwidth as well, but they are less compact.

2.2.1 Electric and magnetic antennas

Electric antennas are characterized by a high electric field components near the antenna while magnetic antennas are characterized by high a magnetic field components close to it. Normally, electric antennas are more prone to couple with close objects, thus magnetic antennas are suitable for applications with embedded antennas.

2.2.2 Constant gain vs. constant aperture

The link behavior of the antennas in free space and far field is governed by Friis' Law:

$$P_{RX} = P_{TX} G_{TX} G_{RX} \left(\frac{\lambda}{4\pi r} \right)^2 = P_{TX} G_{TX} G_{RX} \left(\frac{c}{4\pi r f} \right)^2, \tag{2.10}$$

where P_{RX} is the received power, P_{TX} is the transmitted power, G_{TX} and G_{RX} are the transmit and receive antenna gain, respectively. The last term is commonly known as the free space path loss. The free space does not attenuate signals in a manner inversely proportional to the square of the frequency; actually the term $1/f^2$ is because the antenna gain G is defined in terms of antenna aperture A as [11]:

$$G(f) = \frac{4\pi A(f)}{\lambda^2}, \tag{2.11}$$

constant gain antennas should have a constant aperture in units of wavelength (i.e. the antenna aperture varies inversely proportional to the frequency). On the other hand, a “constant aperture” antenna is one whose antenna aperture is constant with the frequency, so its gain is not constant.

In constant aperture antennas, the size of the aperture in units of wavelength increase as f^2 and the gain of the antenna also increase accordingly. This is the behavior of many directive antennas.

Then in a link with two constant gain antennas (transmit and receive), the received power roll-off as $1/f^2$ in band. A constant aperture receive antenna would cancel this roll-off and yield a flat received power in band [11].

2.2.3 Regions of radiation

The space surrounding an antenna is commonly subdivided into three regions [12]: reactive near field, radiating near field (Fresnel), and far field (Fraunhofer).

The boundaries separating these regions are not unique; various criteria have been established and are commonly used to identify the regions.

The reactive near field region is "that portion of the near-field region immediately surrounding the antenna wherein the reactive field predominates." For most antennas, the outer boundary of this region is $R < 0.62(D^3/\lambda)^{1/2}$, where D is the largest dimension of the antenna and λ is the wavelength.

The radiating near field (Fresnel) region is defined as "that region of the field of an antenna between the reactive near-field region and the far-field region wherein radiation fields predominate and wherein the angular field distribution is dependent upon the distance from the antenna." The inner boundary of this region is $R \geq 0.62(D^3/\lambda)^{1/2}$ and the outer boundary is $R < 2D^2/\lambda$.

The far field (Fraunhofer) region is defined as "that region of the field of an antenna where the angular field distribution is essentially independent of the distance from the antenna." The inner boundary of this region is $R = 2D^2/\lambda$.

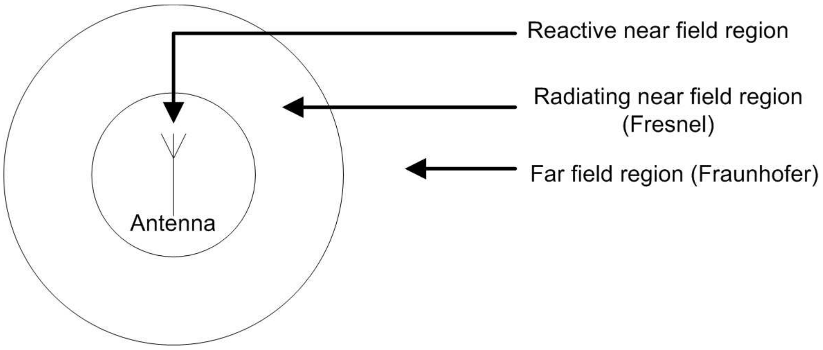
Reactive near field region
Radiating near field region (Fresnel)
Far field region (Fraunhofer)
Antenna

Figure 2.4: Radiation regions for phase error criterion

The above criteria are based on the requirement that the incident spherical wave differs from a uniform plane wave at the edges of the antenna by some portion of a wavelength (λ/k) [13], where k is a constant. The different regions of radiations are depicted in figure 2.4. In figure 2.5 the aforementioned criterion is shown, where the usual choice for the constant k is $k = 16$, whereby the far-field boundary becomes:

$$R \geq \frac{2D^2}{\lambda}. \tag{2.12}$$

Figure 2.6 shows the critical frequency (based on equation (2.12)) as a function of

R for a given antenna with $D = 10$ cm.

For a given distance R, some frequencies of the spectrum may fulfil the far field condition whereas other frequencies may not. In figure 2.7, the critical distance as a function of the frequency and the largest dimension of the antenna is shown.

Another criterion to define near and far field is the radian distance and radian sphere [12]. The radian sphere is a sphere surrounding the antenna with radius equal to the radian distance ($r = \lambda/2\pi$ or $kr = 1$ for an infinitesimal dipole). It defines the region within which the reactive power density is greater than the radiated power density. It represents the volume occupied mainly by the stored energy of the antenna's electric and magnetic fields.

The electric and magnetic fields for an infinitesimal dipole are given by [12]:

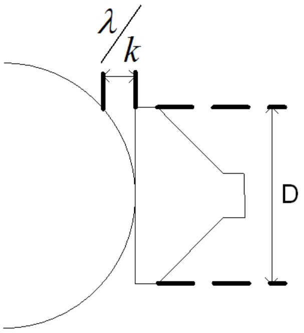

Figure 2.5: Derivation of the far-field criterion

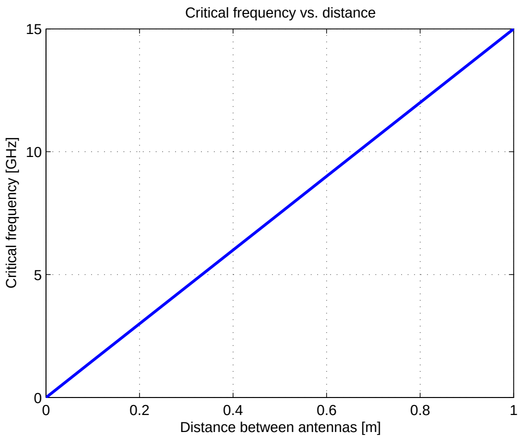

Figure 2.6: Critical frequency as a function of R (using phase error criterion)

$$H_r = H_\theta = 0, \tag{2.13}$$

$$H_\phi = j\frac{kI_0 l \sin\theta}{4\pi r}\left[1+\frac{1}{jkr}\right]e^{-jkr}, \tag{2.14}$$

$$E_r = \eta\frac{I_0 l \cos\theta}{2\pi r^2}\left[1+\frac{1}{jkr}\right]e^{-jkr}, \tag{2.15}$$

$$E_\theta = j\eta\frac{kI_0 l \sin\theta}{4\pi r}\left[1+\frac{1}{jkr}-\frac{1}{(kr)^2}\right]e^{-jkr}, \tag{2.16}$$

$$E_\phi = 0, \tag{2.17}$$

where k is the wave number ($2\pi/\lambda$), I_0 is the excitation current, η is the free space impedance (120π), l is the length of the dipole, θ is the elevation angle with respect to the axis of the dipole, assumed along the zenith, ϕ is the azimuth angle with respect to the x-axis in a rectangular coordinate system with its z-axis along the zenith, and r is the distance from the dipole.

Using this criterion (for an infinitesimal dipole) $kr \ll 1$ represents the near field region, $kr > 1$ represents the intermediate field region and the far field region begins at $kr \gg 1$ (or $r \gg 1/k$) (a deeper explanation of these regions is given in [12]). In figure 2.8 these regions are depicted.

In the near field region, E_r and E_θ are in time phase but they are in time phase quadrature to the H-field; therefore there is no time average power flow associated with them. This means that in the near field region there is no radiating power.

In the intermediate field region, the E-field components lose their in phase condition and approach time phase quadrature. They form a rotating vector in a plane

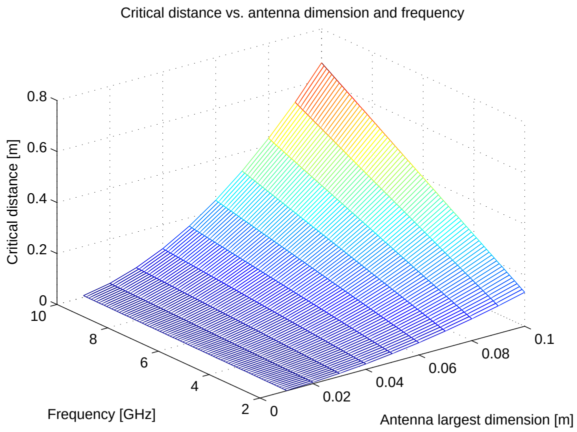

Figure 2.7: Critical distance as a function of R (using phase error criterion)

parallel to the direction of propagation. The E_θ and H_ϕ components approach time-phase, which is an indication of the formation of time average power flow in the radial direction (radiated power).

In the far field region, E and H field components are perpendicular to each other and transverse to the radial direction of propagation. They form a transverse electromagnetic (TEM) wave whose wave impedance is the intrinsic impedance of the medium (120π for free space).

The critical frequency as a function of the distance between antennas is shown in figure 2.9.

In figure 2.9, the far field region would be all the frequencies over the blue line ($kr = 10$). Under the blue line, the time average power flow in the radial direction is not completely formed because the H and E fields are not in phase.

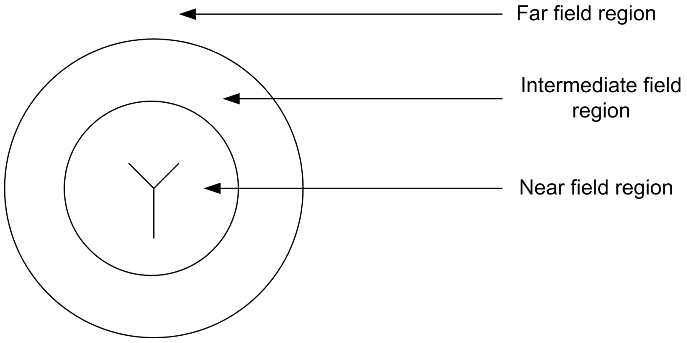

Figure 2.8: Radiation regions for radian-distance criterion

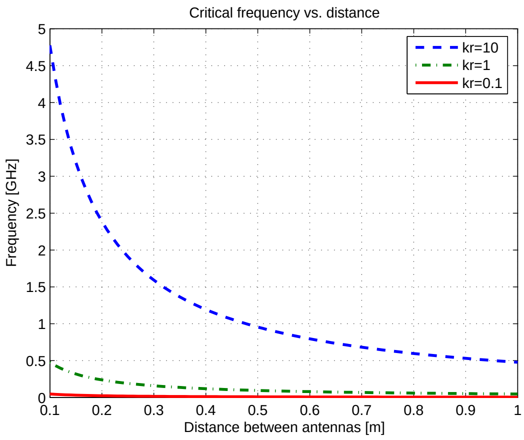

Figure 2.9: Radiation regions for radian-distance criterion

Chapter 3

Near field effects

Different *criteria have been given in chapter 2 in order to define the near field region. These criteria are based on different effects that can appear in such a region. In this chapter, these effects among others are explained and some models are derived. Also the possible repercussions in the transmission are dealt.*

The chapter is structured as follows. In section 3.1 the multiple reflection between transmit and receive antenna is explained. In section 3.2 the phase error produced when transmit and receive antenna are very close to each other is presented. Section 3.3 explains the difference between radiation and reactive fields. Section 3.4 gives some conclusions about each near field effect on transmission.

3.1 Multiple reflections between antennas

Referring to figure 3.1, the voltage induced in a receive antenna due to the electromagnetic field generated by a transmit antenna produces a current through both the antenna impedance Z_A and the load impedance Z_t.

Then, a part of the power picked up by the antenna will be absorbed by the terminal impedance Z_t and a part of the power will be dissipated in the antenna impedance Z_A. This produces a reradiation from the receive antenna than can be picked up by the transmit antenna and then reradiated again producing in the receive antenna some interference. The amount of power reradiated by the receive antenna depends on the scattering cross section of the antenna and the power reaching it (this power decreases with distance). The scattering cross section of the antenna may increase or decrease with the mismatching of the antenna and its gain and it depends also on the antenna physical structure.

In figure 3.2, the effect of the multiple reflections between antennas is depicted.

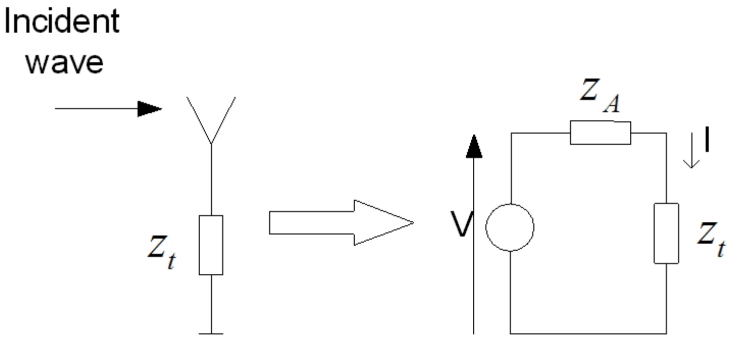
Incident
wave
Z_t
Z_A
I
V
Z_t

Figure 3.1: Antenna terminated in impedance Z_t and its equivalent circuit

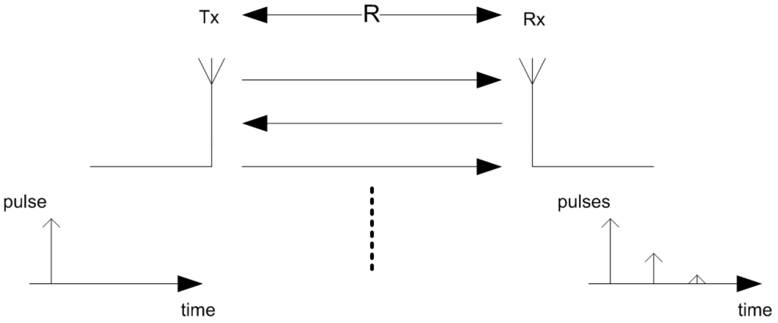
Tx
R
Rx
pulse
time
pulses
time

Figure 3.2: Multiple reflections between two antennas

For a given distance, the multiple reflections of the antennas may add constructively or destructively depending on the frequency and phase shift introduced by both antennas. This effect causes a variation of the received power as a function of the frequency. That means that the channel frequency response may change for different distances, not only the level, but also the shape and it will distort the received signal.

In this section the effect of multiple reflections between antennas is explained and expressions are derived to obtain the frequency response of the direct path channel taking into account these reflections. Finally this effect is studied for the UWB channel and some conclusions are given.

3.1.1 Reradiated power

Refering to figure 3.1, the power dissipated in the terminal impedance Z_t is given by:

$$P_{load} = I^2 R_t, \tag{3.1}$$

where R_t is the real part of the terminal impedance Z_t.

On the other hand, the power dissipated in the antenna impedance Z_A will be:

$$P_{ant} = I^2 R_A, \tag{3.2}$$

where R_A is the real part of the antenna impedance.

The real part of this impedance, R_A, has two components; the radiation resistance R_r and the loss resistance R_L ($R_A = R_r + R_L$). The loss resistance arises from the resistance of the antenna elements, and the power dissipated in this resistance is lost as heat (Joule effect).

Then the power dissipated in the radiation resistance R_r (power reradiated or scattered) is given by:

$$P_{rad} = I^2 R_r. \tag{3.3}$$

This reradiated or scattered power is analogous to the power that is dissipated in the output impedance of a generator. Thus, in a perfectly lossless conjugate matched antenna ($R_L = 0$ and $Z_A = Z_t{}^*$) the same power as delivered to the load will be reradiated from the antenna [14].

Assuming a lossless conjugate matched antenna, the scattered power is:

$$P_{load} = S_i A_{eff} = S_i \frac{\lambda^2 G}{4\pi}, \tag{3.4}$$

$$EIRP = G I^2 R_A = G \left| \frac{V}{Z_A + Z_t} \right|^2 R_A = G \frac{V^2}{4R_A} = G P_{load}, \tag{3.5}$$

$$EIRP = \frac{V^2}{4R_A} G = S_i \frac{\lambda^2 G^2}{4\pi}, \tag{3.6}$$

where P_{load} is the power delivered to the load, S_i is the power flux incident in the antenna, A_{eff} is the effective area of the antenna, G is the antenna gain, λ is the wave length, $EIRP$ is the reradiated power and V is the voltage generated in the antenna terminals.

For a not perfectly matched antenna, the reradiation can be larger or smaller than the power in equation (3.5). For example for a short-circuited thin $\lambda/2$ dipole (a parasitic antenna), the reradiated power will be four times larger than this power.

The power reradiated in a not matched antenna is:

$$EIRP_{notmatched} = GI^2R_A = G\left|\frac{V}{Z_A + Z_t'}\right|^2 R_A = G\frac{V^2}{|Z_A + Z_t'|^2}R_A, \tag{3.7}$$

$$\begin{aligned} EIRP_{notmatched} &= \frac{EIRP_{notmatched}}{EIRP}EIRP = \\ &\frac{G\frac{V^2}{|Z_A+Z_t'|^2}R_A}{\frac{V^2}{4R_A}}S_i\frac{\lambda^2 G}{4\pi} = \\ &\frac{4R_AR_A}{|Z_A+Z_t'|^2}S_i\frac{\lambda^2G^2}{4\pi} = S_i\left|\frac{2R_A}{Z_A+Z_t'}\right|^2\frac{\lambda^2G^2}{4\pi} = S_i\sigma, \end{aligned} \tag{3.8}$$

where $EIRP_{notmatched}$ is the power reradiated from the antenna, Z_t' is the new load impedance and σ is known as the scattering cross section of the antenna.

$$\sigma = \left|\frac{2R_A}{Z_A + Z_t'}\right|\frac{\lambda^2G^2}{4\pi}. \tag{3.9}$$

Notice that equation (3.9) express the part of the reradiated power due to the antenna an terminal impedance, but not the “structural” part. It will be the reradiation power of a thin dipole, but for other kinds of antennas, as for example planar antennas, the reradiated or reflected power due to the structure of the antenna can be very important. The exact value of the scattering cross section can not be obtained in an easy way and usually it needs the utilization of electromagnetic simulators.

From (3.8) it can be seen that for a short-circuited thin $\lambda/2$ dipole ($Z_A \approx 73\ \Omega$) the power reradiated is four times the power reradiated for the same matched antenna in (3.6).

3.1.2 Model of mutual coupling between antennas for narrowband signals

In [15] a model to calculate the mutual coupling between two horn antennas based on the multiple reflections between them is exposed.

Assuming transmit and receive antenna, with gains G_{tx} and G_{rx}, respectively. The two antennas are separated by a distance R, as illustrated in figure 3.3.

The power density in the receive antenna produced by the transmit antenna is given by:

$$S_{r1} = \frac{P_{tx}G_{tx}}{4\pi R^2}, \tag{3.10}$$

where S_{r1} is the power density in the receive antenna and P_{tx} is the transmitted power. The electric field intensity is then

$$E_{r1} = (Z_0 S_{r1})^{\frac{1}{2}}, \tag{3.11}$$

where Z_0 is the wave impedance in free space.

The power density in the transmit antenna produced by the first reflection in the receive antenna, is

$$S_{t1} = \frac{S_{r1}\sigma_{rx}}{4\pi R^2} = \frac{P_{tx}G_{tx}}{4\pi R^2}\frac{\sigma_{rx}}{4\pi R^2}, \tag{3.12}$$

where S_{t1} is the power density in the transmit antenna and σ_{rx} is the scattering cross section of the receive antenna. The electric field intensity will be

$$E_{t1} = (Z_0 S_{t1})^{\frac{1}{2}} e^{-j(kR+\phi_{rx})}, \tag{3.13}$$

where $k = 2\pi/\lambda$ is the wave number, and ϕ_{rx} is the phase introduced by the receive antenna in the reflection.

The transmit antenna reradiates a part of the received power reradiated by the receive antenna back to the receive antenna. The power density of this reflection in the receive antenna is

$$S_{r2} = \frac{S_{t1}\sigma_{tx}}{4\pi R^2} = \frac{P_{tx}G_{tx}}{4\pi R^2}\frac{\sigma_{rx}}{4\pi R^2}\frac{\sigma_{tx}}{4\pi R^2} = \frac{P_{tx}G_{tx}}{4\pi R^2}\frac{\sigma_{rx}\sigma_{tx}}{(4\pi R^2)^2}, \tag{3.14}$$

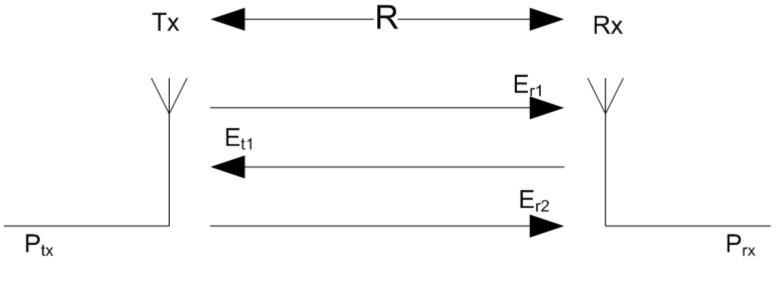

Figure 3.3: Multiple reflections between antennas

where σ_{tx} is the scattering cross section of the transmit antenna. And the electric field intensity is then

$$\begin{aligned}E_{r2} = (Z_0 S_{r2})^{\frac{1}{2}} e^{-j(2kR+\phi_{rx}+\phi_{tx})} = \\ \left(Z_0 \frac{P_{tx}G_{tx}}{4\pi R^2} \frac{\sigma_{rx}\sigma_{tx}}{(4\pi R^2)^2}\right)^{\frac{1}{2}} e^{-j(2kR+\phi_{rx}+\phi_{tx})} = \\ \left(Z_0 \frac{P_{tx}G_{tx}}{4\pi R^2}\right)^{\frac{1}{2}} \left(\frac{\sigma_{rx}\sigma_{tx}}{(4\pi R^2)^2}\right)^{\frac{1}{2}} e^{-j(2kR+\phi_{rx}+\phi_{tx})},\end{aligned} \quad (3.15)$$

where ϕ_{tx} is the phase shift introduced by the transmit antenna in the reflection.

By analogy, the electric field intensity in the receive antenna for the n-th reflection is

$$E_{rn} = \left(Z_0 \frac{P_{tx}G_{tx}}{4\pi R^2}\right)^{\frac{1}{2}} \left(\left(\frac{\sigma_{rx}\sigma_{tx}}{(4\pi R^2)^2}\right)^{\frac{1}{2}} e^{-j(2kR+\phi_{rx}+\phi_{tx})}\right)^{n-1}. \quad (3.16)$$

Then, the total electric field in the receive antenna is

$$\begin{aligned}E_r = \sum_{n=1}^{\infty} E_{rn} = \\ \left(Z_0 \frac{P_{tx}G_{tx}}{4\pi R^2}\right)^{\frac{1}{2}} \sum_{n=1}^{\infty} \left(\left(\frac{\sigma_{rx}\sigma_{tx}}{(4\pi R^2)^2}\right)^{\frac{1}{2}} e^{-j(2kR+\phi_{rx}+\phi_{tx})}\right)^{n-1}.\end{aligned} \quad (3.17)$$

The geometric summation in (3.17) can be reduced to [15]:

$$E_r = \left(Z_0 \frac{P_{tx}G_{tx}}{4\pi R^2}\right)^{\frac{1}{2}} \left(1 - \frac{(\sigma_{rx}\sigma_{tx})^{\frac{1}{2}}}{4\pi R^2} e^{-j(2kR-\phi_{rx}+\phi_{tx})}\right)^{-1}, \quad (3.18)$$

because $(\sigma_{rx}\sigma_{tx})^{\frac{1}{2}}/(4\pi R^2) < 1$ [15].

However, this assumption is not always fulfilled. The distances and frequencies for which this assumption is correct can be extracted from

$$\left|\frac{(\sigma_{rx}\sigma_{tx})^{\frac{1}{2}}}{4\pi R^2} e^{-j(2kR+\phi_{rx}+\phi_{tx})}\right| < 1. \quad (3.19)$$

For two ideal constant 2 dB gain antennas, the limit frequencies and distances are shown in figure 3.4.

Figure 3.4 shows the condition for the convergence of the geometrical summation in equation (3.17). For example, for a frequency of 1 GHz, the minimum distance to fulfil the condition is 3.8 cm.

Then, the received power in receive antenna can be expressed as:

$$P_{rx} = \frac{|E_r|^2}{Z_0} A_{eff_{rx}} = \\ P_{tx} GtxGrx \left(\frac{\lambda}{4\pi R} \right)^2 \left| 1 - \frac{(\sigma_{rx}\sigma_{tx})^{\frac{1}{2}}}{4\pi R^2} e^{-j(2kR+\phi_{rx}+\phi_{tx})} \right|^{-2}, \qquad (3.20)$$

where $A_{eff_{rx}}$ is the effective area of the receive antenna.

Using the definition of the scattering cross section in equation (3.9) and assuming a perfectly conjugate matching lossless antenna, the receive power will be:

$$P_{rx} = \frac{|E_r|^2}{Z_0} A_{eff_{rx}} = \\ P_{tx} G_{tx} G_{rx} \left(\frac{\lambda}{4\pi R} \right)^2 \left| 1 - G_{tx} G_{rx} \left(\frac{\lambda}{4\pi R} \right)^2 e^{-j(2kR+\phi_{rx}+\phi_{tx})} \right|^{-2}. \qquad (3.21)$$

Equation (3.21) shows that the received power for a given frequency is not only the power obtained with the Friis transmission formula because the multiple reflections between the antennas can be added constructively or destructively in the receive antenna.

Figure 3.5 shows the variation of the received power for a frequency of 1 GHz as a function of the distance for two identical 2 dB gain antennas and different phase shifts (to point out the effect of the phase shift), with transmitter power of 1 W.

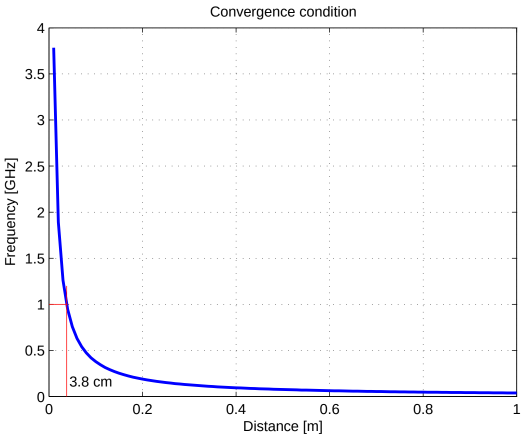

Figure 3.4: Condition for convergence of the geometrical summation

3.1.3 Extension of the model for UWB

The effect explained in section 3.1.2 is different for each frequency. Then for an UWB signal, it will be different for different frequencies in the spectrum and this may cause signal distortion.

In figure 3.6 the variation of the received power when the transmitted power is 1 W for each frequency, for a distance of 15 cm between two identical 2 dB gain antennas is shown.

In order to use this model in UWB systems, the frequency response of the entire band has to be calculated and then the impulse response can be obtained by appl-

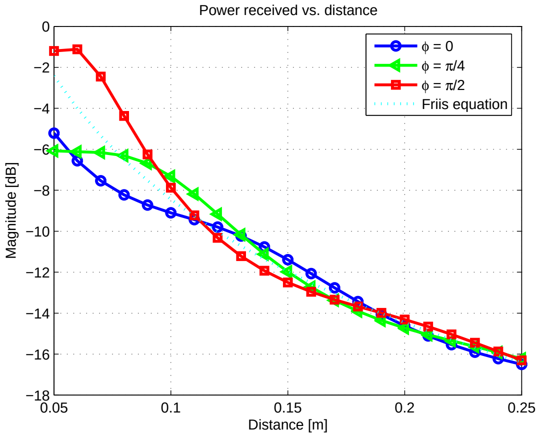

Figure 3.5: Power received as a function of the distance

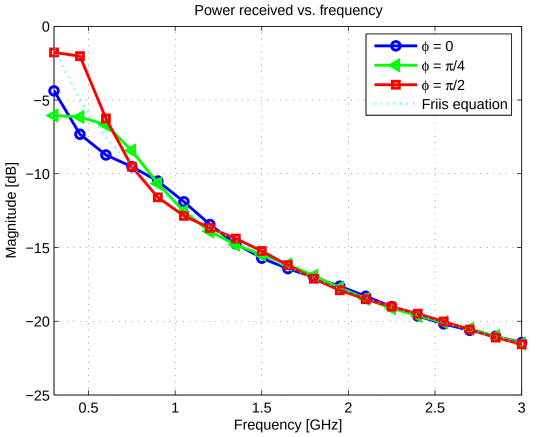

Figure 3.6: Power received as a function of the frequency

ying the inverse Fourier transform.

First of all, the frequency transfer function has to be calculated.

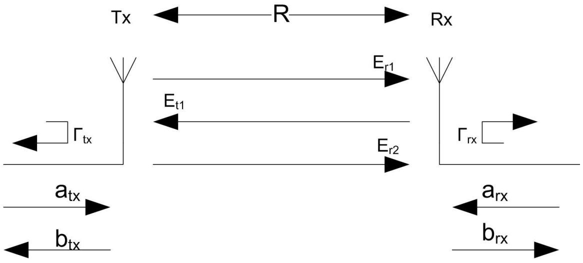

Figure 3.7: Two ports model of the antennas

In figure 3.7 a two ports model of the antennas is represented. Γ_{tx} and Γ_{rx} are the reflection coefficient of the transmit and receive antenna, respectively. a_{tx}, b_{tx}, a_{rx} and b_{rx} are the waves approaching and leaving the transmit and receive antennas, respectively.

The electric field intensity related to the incident wave a_{tx} can be derived in a similar form as done in section 3.1.2. Equation (3.22) is analogous to equation (3.11) but including the phase terms.

$$\begin{aligned}
E_{r1}(\omega) &= (Z_0 S_{r1}(\omega))^{\frac{1}{2}} e^{-j(kR+\phi_T(\omega))}, && (3.22)\\
E_{r1}(\omega) &= \left(Z_0 \frac{P_{tx}(\omega)G_{tx}(\omega)}{4\pi R^2}\right)^{\frac{1}{2}} e^{-j(kR+\phi_T(\omega))}, && (3.23)\\
E_{r1}(\omega) &= \sqrt{Z_0}\sqrt{G_{tx}(\omega)}\sqrt{P_{tx}(\omega)}\frac{e^{-j(kR+\phi_T(\omega))}}{\sqrt{4\pi}R}, && (3.24)\\
P_{tx} &= 1-|\Gamma_{tx}(\omega)|^2 a_{tx}(\omega)^2, && (3.25)\\
E_{r1}(\omega) &= \sqrt{Z_0}\sqrt{1-|\Gamma_{tx}(\omega)|^2 a_{tx}(\omega)^2}\sqrt{G_{tx}(\omega)}\frac{e^{-j(kR+\phi_T(\omega))}}{\sqrt{4\pi}R}, && (3.26)\\
E_{r1}(\omega) &= \sqrt{Z_0}\sqrt{1-|\Gamma_{tx}(\omega)|^2}a_{tx}(\omega)\sqrt{G_{tx}(\omega)}\frac{e^{-j(kR+\phi_T(\omega))}}{\sqrt{4\pi}R}, && (3.27)
\end{aligned}$$

where ϕ_T includes the phase shift introduced by the reflection coefficient and the transmission characteristic of the antenna, and ω represents the angular frequency dependency.

Then, the electric field intensity for the n-th reflection will be:

$$\begin{aligned}
E_{rn}(\omega) = \left(Z_0\left(1-|\Gamma_{tx}(\omega)|^2\right)G_{tx}(\omega)\right)^{\frac{1}{2}} a_{tx}(\omega)\frac{e^{-j(kR+\phi_T(\omega))}}{\sqrt{4\pi}R}\cdot \\
\left((\sigma_{tx}(\omega)\sigma_{rx}(\omega))^{\frac{1}{2}}\frac{e^{-j(2kR+\phi_{tx}(\omega)+\phi_{rx}(\omega))}}{4\pi R^2}\right)^{n-1}, \qquad (3.28)
\end{aligned}$$

and the total electric field intensity in the receive antenna is:

$$\begin{aligned}
E_r(\omega) = \sum_{n=1}^{\infty} E_{rn}(\omega) = \\
\left(Z_0(1-|\Gamma_{tx}(\omega)|^2)G_{tx}(\omega)\right)^{\frac{1}{2}} a_{tx}(\omega)\frac{e^{-j(kR+\phi_T(\omega))}}{\sqrt{4\pi}R} \cdot \\
\left(1-\frac{(\sigma_{tx}(\omega)\sigma_{rx}(\omega))^{\frac{1}{2}}}{4\pi R^2}e^{-j(2kR+\phi_{tx}(\omega)+\phi_{rx}(\omega))}\right)^{-1}.
\end{aligned} \tag{3.29}$$

As in section 3.1.2, the criterion for convergence of the geometric summation has to be evaluated. In this case, the criterion has to be evaluated for every frequency, and the limit distance will be the maximum distance obtained from all the frequencies.

The corresponding wave generated in the receive antenna can be expressed as:

$$\begin{aligned}
b_{rx}(\omega) = \left(\frac{A_{eff_{rx}}(\omega)}{Z_0}\right)^{\frac{1}{2}}\left(1-|\Gamma_{rx}(\omega)|^2\right)^{\frac{1}{2}} E_r(\omega)e^{-j\phi_R(\omega)} = \\
a_{tx}(\omega)\left(1-|\Gamma_{rx}(\omega)|^2\right)^{\frac{1}{2}}\left(1-|\Gamma_{tx}(\omega)|^2\right)^{\frac{1}{2}} \cdot \\
\frac{(G_{rx}(\omega)G_{tx}(\omega))^{\frac{1}{2}}\lambda}{4\pi R}e^{-j(kR+\phi_T(\omega)+\phi_R(\omega))} \cdot \\
\left(1-\frac{(\sigma_{tx}(\omega)\sigma_{rx}(\omega))^{\frac{1}{2}}}{4\pi R^2}e^{-j(2kR+\phi_{tx}(\omega)+\phi_{rx}(\omega))}\right)^{-1},
\end{aligned} \tag{3.30}$$

where ϕ_R is the phase shift introduced by the reflection coefficient and the receive characteristic of the antenna.

Finally, the transfer function of the system (S_{21}) is:

$$\begin{aligned}
H(\omega) = S_{21}(\omega) = \left.\frac{b_{rx}(\omega)}{a_{tx}(\omega)}\right|_{a_{rx}(\omega)=0} = \\
\left(1-|\Gamma_{rx}(\omega)|^2\right)^{\frac{1}{2}}\left(1-|\Gamma_{tx}(\omega)|^2\right)^{\frac{1}{2}} \cdot \\
\frac{(G_{rx}(\omega)G_{tx}(\omega))^{\frac{1}{2}}\lambda}{4\pi R}e^{-j(kR+\phi_T(\omega)+\phi_R(\omega))} \cdot \\
\left(1-\frac{(\sigma_{tx}(\omega)\sigma_{rx}(\omega))^{\frac{1}{2}}}{4\pi R^2}e^{-j(2kR+\phi_{tx}(\omega)+\phi_{rx}(\omega))}\right)^{-1},
\end{aligned} \tag{3.31}$$

where $H(\omega)$ represents the channel transfer function.

Substituting (3.9) into (3.31), $H(\omega)$ can be expressed as:

$$\begin{aligned} H(\omega) = {} & \left(1-|\Gamma_{rx}(\omega)|^2\right)^{\frac{1}{2}} \left(1-|\Gamma_{tx}(\omega)|^2\right)^{\frac{1}{2}} \cdot \\ & \frac{\left(G_{rx}(\omega)G_{tx}(\omega)\right)^{\frac{1}{2}}\lambda}{4\pi R} e^{-j(kR+\phi_T(\omega)+\phi_R(\omega))} \cdot \\ & \left(\begin{array}{c} 1-\left(\frac{\lambda}{4\pi R}\right)^2 G_{tx} \left|\frac{2R_{A_{tx}}(\omega)}{Z_{A_{tx}}(\omega)+Z_{L_{tx}}}\right| G_{rx} \cdot \\ \left|\frac{2R_{A_{rx}}(\omega)}{Z_{A_{rx}}(\omega)+Z_{L_{rx}}}\right| e^{-j(2kR+\phi_{tx}(\omega)+\phi_{rx}(\omega))} \end{array} \right)^{-1}, \end{aligned} \tag{3.32}$$

where $Z_{L_{tx}}$ and $Z_{L_{rx}}$ are the transmission line impedances of the transmit and receive antennas, respectively.

Figure 3.8 shows the different transfer functions from 300 MHz to 10 GHz for three distances (15 cm, 25 cm and 35 cm) using two constant 2 dB gain and 90 Ω input impedance antennas, assuming a zero phase shift.

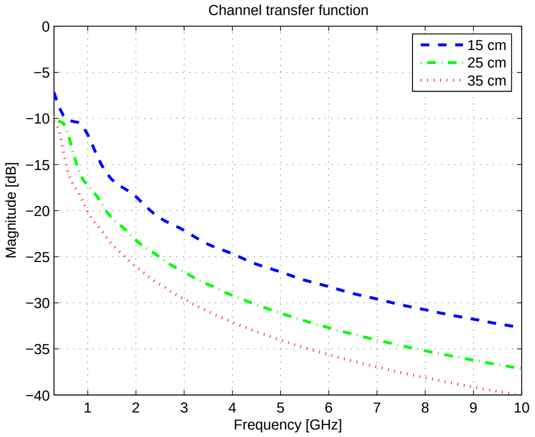

Figure 3.8: Transfer function as a function of frequency for several distances

The differences of the normalized channel transfer function and the Friis transmission equation are shown in figure 3.9. In this figure it can be seen that for frequencies beyond 3 GHz all the curves converge to zero.

The continuous transition of the transfer function versus the distance can be seen in figure 3.10.

If every antenna introduces a phase shift of $\pi/4$ in each reflection, then figure 3.10 becomes 3.11.

Comparing figure 3.10 and figure 3.11 we can conclude that the phase shift introduced by the antennas in each reflection is also an important parameter.

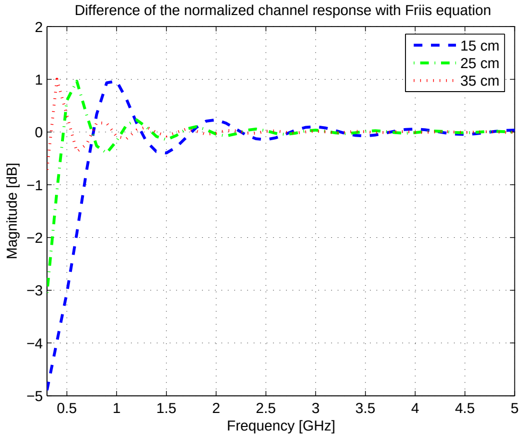

Figure 3.9: Differences with Friis transmission equation

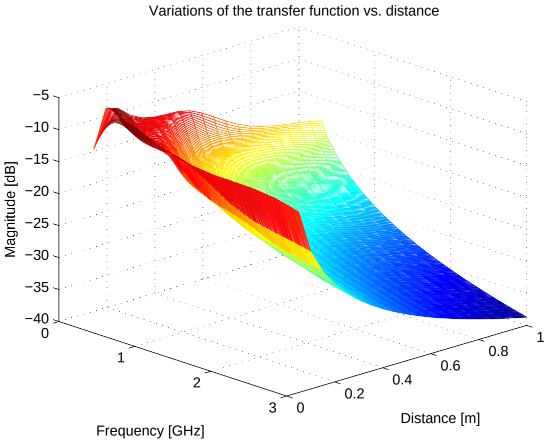

Figure 3.10: Continuous transition of the transfer function vs. distance

Thus, the impulse response of the system (only the direct path is assumed) will be the inverse Fourier transform of the channel frequency response.

3.1.4 Simulations

Several simulations have been done to assess the importance of this effect on UWB systems. The channel transfer function has been calculated for different kinds of antennas and several distances. A Gaussian pulse of 200 ps has been filtered with this transfer function. The inverse Fourier transform using a Blackman window has been calculated to obtain the pulse waveform in the receive antenna. The simulations have been done using the model explained in this chapter. This model is valid for antennas with low structural mode scattering cross section. For antennas with large flat surfaces, simulations using an electromagnetic simulator are required.

Constant 2 dB gain antennas from 300 MHz to 10 GHz

In this simulation two constant 2 dB gain antennas between 300 MHz and 10 GHz (and no gain outside this band) have been used. A 200 ps Gaussian pulse has been sent. The receive waveform for different distances is shown in figure 3.12.

An input impedance of 90 Ω in the entire band is assumed (S_{11} better than -10 dB).

In figure 3.12 distances beyond 0.5 m have been omitted because the response for such distances is almost the same. The main distortion is for distances below 0.5 m.

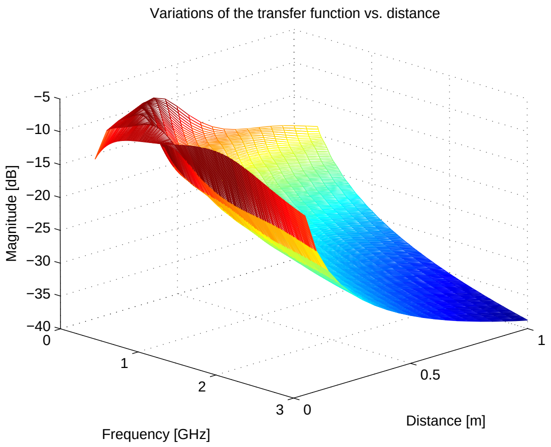

Figure 3.11: Continuous transition of the transfer function vs. distance with phase shift of $\pi/4$ in each reflection

Constant 6 dB gain antennas from 300 MHz to 10 GHz

If the gain of the antennas is increased, the effect is stronger; some resonances are produced for frequencies which fulfill the following condition (for these frequencies, the multiple reflections are added in phase in the receive antenna):

$$f = c\left(\frac{k}{2R} - \frac{\phi_{tx} + \phi_{rx}}{4\pi R}\right), \tag{3.33}$$

where c is the speed of light, and k is an integer greater than 0. This effect is shown in figure 3.13.

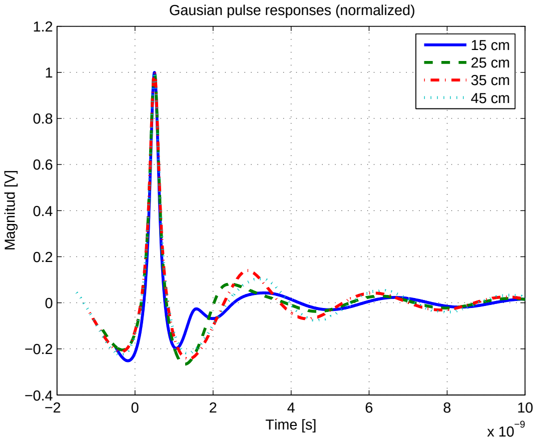

Figure 3.12: Received waveform distortion

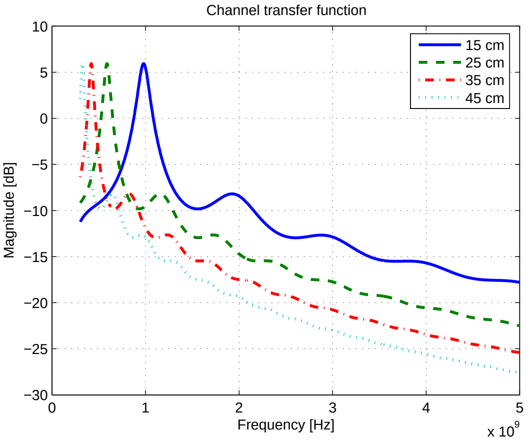

Figure 3.13: Resonances in the channel transfer function

The received waveform in this simulation is shown in figure 3.14.

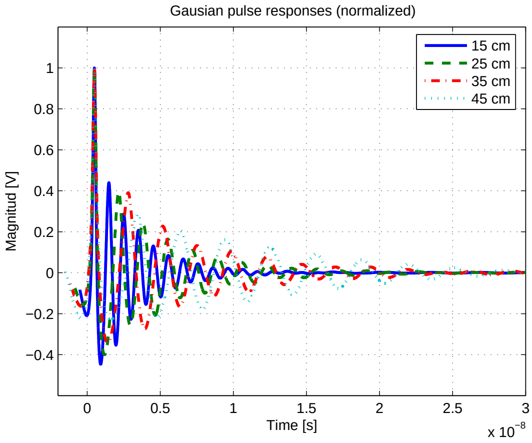

Figure 3.14: Received time domain waveform

Real measurements of an antenna

Simulations with real measurements of gain and impedance of a bi-conical antenna have been done. The gain of the antenna is shown in figure 3.15.

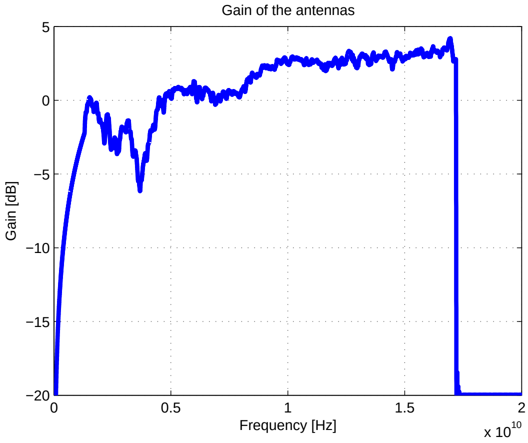

Figure 3.15: Gain of the antenna vs. frequency

Using the measured data of the gain and input impedance, the minimum distance for convergence of the model has to be calculated using equation 3.19. This condition has to be evaluated for each frequency, and then, the minimum distance for the convergence will be the more restrictive distance. In our case, this distance is 1.8 cm.

The measured data of the antenna (gain) was only available from 1.2 GHz to 17.2 GHz, so, the frequency band between 0 to 1.2 GHz was assumed to be as in figure 3.15.

The received waveform for this simulation is as in figure 3.16.

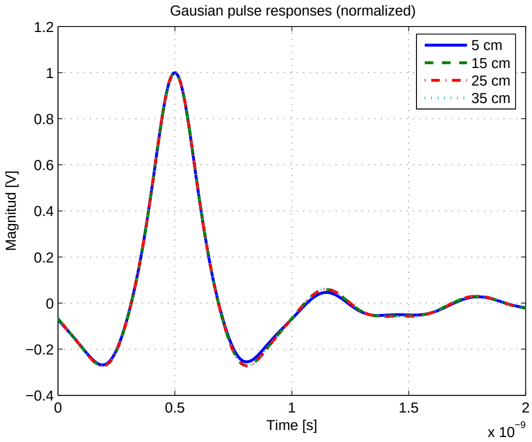

Figure 3.16: Received waveform with measured antennas

In figure 3.16 it can be seen that the received waveform is almost the same for all distances. This is because the gain for low frequencies (below 1 GHz) is very low.

Diamond antenna

Simulations using XFDTD[1] are performed in order to obtain the received pulse waveform for different distances, between two diamond antennas. A diamond antenna is a plannar antenna formed by two isosceles triangles as it can be seen in figure 3.17. The width and height of the triangles is about $\lambda/4$ of the center frequency. It is chosen 6 cm in order to have a higher reflection between the antennas to highlight the effect. For a smaller antenna the effect would be smaller, due to the dependence between the surface of the antenna and the structural mode of the scattering cross section.

Figure 3.18 shows the gain and reflection coefficients of the simulated antenna.

Figure 3.19 shows the received pulse waveform for different distances (3, 4 and

---

[1] Electromagnetic simulator based on the Finite Difference Time Domain method. Copyright ©1995-2003 Remcom Incorporated

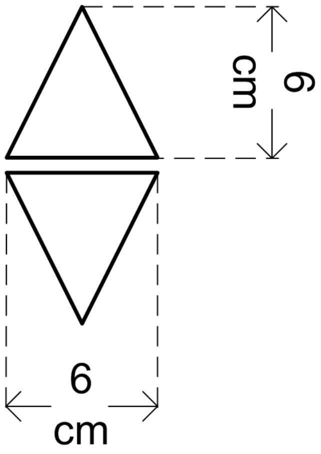

Figure 3.17: Structure of the simulated diamond antenna

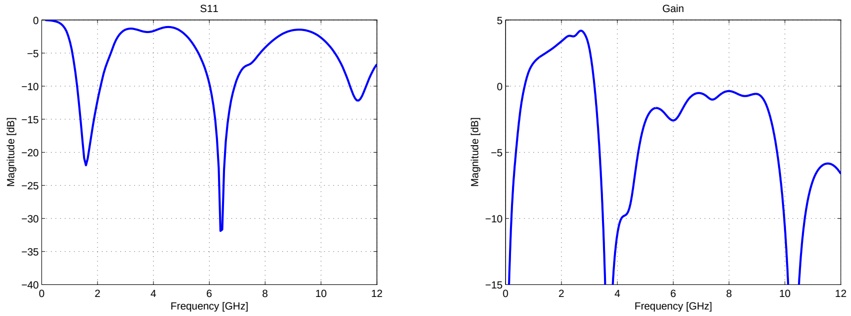

Figure 3.18: Reflection coefficient (left) and gain (right) of the simulated antenna

5 cm). Vertical green lines mark an interval equivalent to two times the distance between the antennas at the speed of light in order to have a reference of the "repetition" of the pulse due to the multiple reflections.

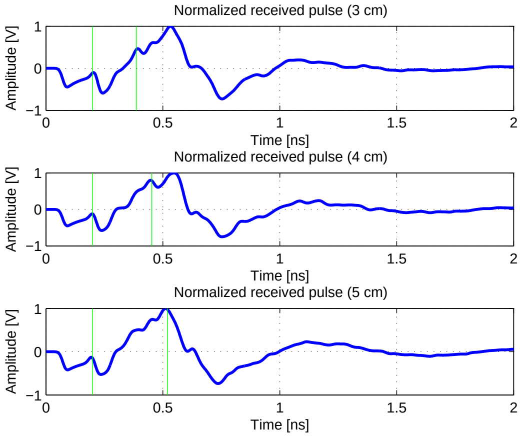

Figure 3.19: Received pulses for different distances

3.2 Phase error

In section 2.2.3 several criteria to determine the different radiation regions have been introduced. One of them is the phase error criterion that is based on the restriction that a spherical wave differs from a plane wave in a given fraction of λ (usually $\lambda/16$, or a phase error of $\pi/8$).

When two antennas are close to each other, the spherical wave produced by the transmit antenna reaches the receive antenna with some phase error (see figure 2.5). This phase error may cause the received power to be larger or smaller than the expected one because the different rays from transmit antenna have different phases, and may add constructively or destructively in the receive antenna.

The phase of each ray is a function of the distance between antennas, the frequency and the dimension of the antennas, so, the effect will be different for different distances, frequencies and antenna sizes. This effect causes some variations in the received power as a function of the distance between antennas and the frequency. Therefore this may cause distortion in the received signal (variation in the received pulse shape and/or power).

3.2.1 Phase error for a dipole

To start, the voltage in the terminals of a thin dipole will be calculated as a function of the distance.

In figure 3.20 the situation of the dipole is depicted,

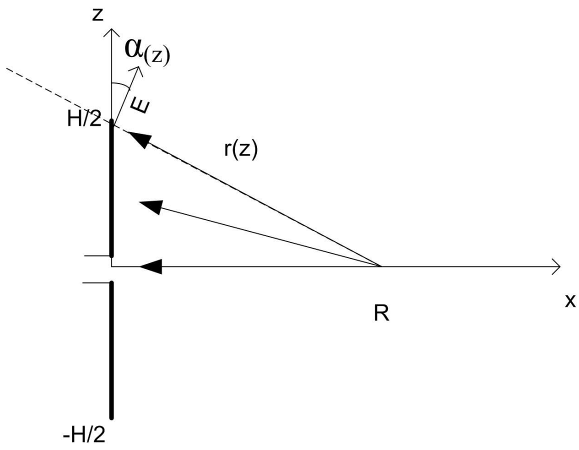

Figure 3.20: Receive dipole

where H is the length of the dipole, R is the position of a point source (infinitesimal dipole), $r(z)$ is the distance between the point source and every point of the dipole and α is the angle between the electric field E direction and the z axis.

Assuming this situation, the voltage in the terminals of the dipole will be:

$$V \propto \int_{-H/2}^{H/2} E_{rz}(z) I(z) \mathrm{dz}, \tag{3.34}$$

where $E_{rz}(z)$ is the z component of the electric field on the surface of the dipole and $I(z)$ is the current distribution on the surface of the dipole. For some constant c', then:

$$\begin{aligned} V = c' \int_{-H/2}^{H/2} I(z) \frac{e^{-jkr(z)}}{r(z)} \cos(\alpha(z)) \mathrm{dz} = \\ c' e^{-jkR} \int_{-H/2}^{H/2} I(z) \frac{e^{-jk(r(z)-R)}}{r(z)} \cos\left(\arctan\left(\frac{z}{R}\right)\right) \mathrm{dz}, \end{aligned} \tag{3.35}$$

where $k = 2\pi/\lambda$ is the wave number and z is the position along the dipole. Then, the voltage can be expressed as:

$$V = c'' \int_{-H/2}^{H/2} I(z) \frac{e^{-j\frac{2\pi}{\lambda}\left(\sqrt{R^2+z^2}-R\right)}}{\sqrt{R^2+z^2}} \cos\left(\arctan\left(\frac{z}{R}\right)\right) \mathrm{dz}, \tag{3.36}$$

where c'' is a constant different from c'.

Assuming a uniform current distribution ($I(z) =$ constant), the received power for several distances as a function of the frequency for a 16 cm dipole is shown in figure 3.21. From up to down, the curves correspond to 50, 10, 5, 2 and 1 cm.

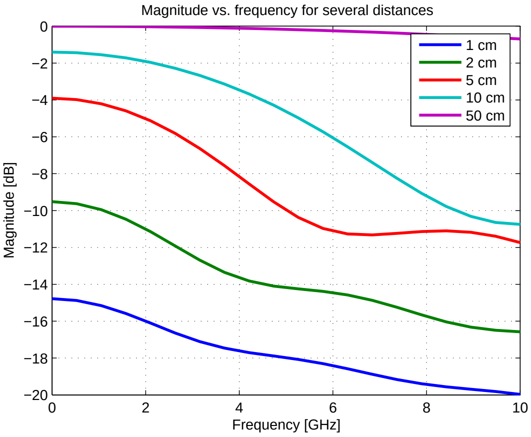

Figure 3.21: Magnitude vs. frequency for several distances, for a 16 cm uniform current distribution dipole

The received power ($20\log_{10}(V)$) is normalized to the distance assuming a distance dependence of $1/R$ ($1/R^2$ for the power), this means that for short distances the received power is less than the power expected assuming this law. The main reason is that for short distances, the different rays picked up by the antenna are not in-phase, and therefore the total received power is less. Another reason is that for short distances, the different distances covered for every ray are also different and larger than R, except for the center of the dipole.

Assuming a sinusoidal current illumination (it has been verified that the current in a center-feed wire antenna has sinusoidal form with nulls at the end points [12]), the receive power for several distances as a function of the frequency is shown for the same dipole in figure 3.22. The order of the curves at 1 GHz is the same as before (from up to down, the curves correspond to 50, 10, 5, 2 and 1 cm).

In this case, the normalized power received at short distances is also smaller than for large distances for low frequencies. Another effect is that the null points (in frequency) in the far field, are not null in the near field. This is because the radiation pattern in the near field is different from the radiation pattern in the far field. In figure 3.23 this effect is depicted.

Figure 3.23 shows two 2λ dipoles. The former (left) is situated in the far field, so, the receive voltage V_{FF} using equation (3.36) will be zero. In the second dipole (right), the receive voltage V_{NF} using the same equation has not to be zero.

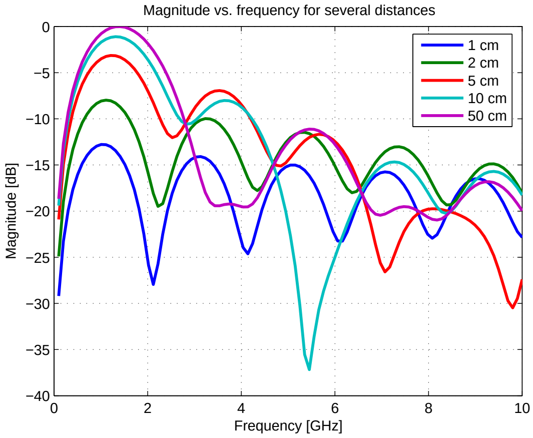

Figure 3.22: Magnitude vs. frequency for several distances, for a 16 cm sinusoidal current distribution dipole

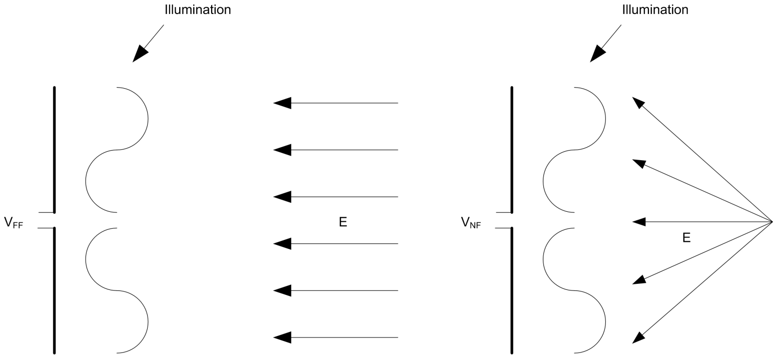
Illumination
Illumination
V_{FF}
E
V_{NF}
E

Figure 3.23: Radiation pattern distortion

It has been assumed, in the above formulas, that the electric field radiated from an infinitesimal dipole has model

$$E_\theta \propto \frac{e^{-jkr}}{r}\hat{\theta}, \tag{3.37}$$

where $\hat{\theta}$ is a unitary vector in the theta direction. But actually, this is an approximation of the electric field for far field regions. In the near field this approximation is not valid and the total electric field has to be calculated using the equations in section 2.2.3.

Considering the situation depicted in figure 3.24, the electric and magnetic fields at R in the z and y (entering into the paper) directions are:

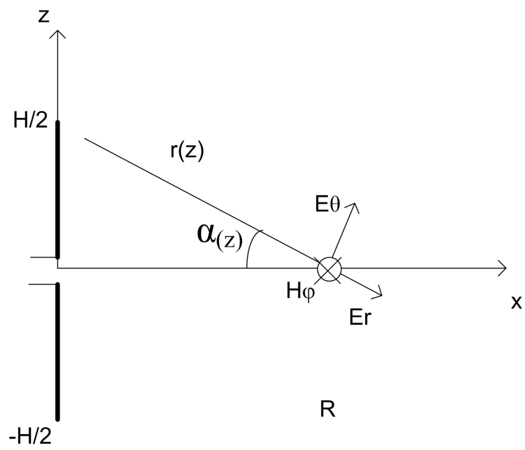

Figure 3.24: Electric and magnetic fields from a dipole

$$E_{rz} = \begin{bmatrix} \int_{-H/2}^{H/2} E_\theta(z)\cos(\alpha)\mathrm{dz}+ \\ \\ \int_{-H/2}^{H/2} E_r(z)\cos\left(\frac{\pi}{2}-\alpha\right)\mathrm{dz} \end{bmatrix}\hat{z} \tag{3.38}$$

$$H_{ry} = \left[\int_{-H/2}^{H/2} H_\phi(z)\mathrm{dz}\right]\hat{y}. \tag{3.39}$$

Using the fields described in equations (2.14) to (2.16), the total electric and magnetic fields can be expressed as

$$E_{rz} = \left[\begin{array}{l} \displaystyle\int_{-H/2}^{H/2} j\eta \frac{kI(z)l\sin\theta}{4\pi r(z)}\left[1+\frac{1}{jkr(z)}-\frac{1}{(kr(z))^2}\right]\cdot \\ \hfill e^{-jkr(z)}\cos(\alpha)\mathrm{d}z+ \\ \displaystyle\int_{-H/2}^{H/2} \eta \frac{I(z)l\cos\theta}{2\pi r(z)^2}\left[1+\frac{1}{jkr(z)}\right]\cdot \\ \hfill e^{-jkr(z)}\cos\left(\frac{\pi}{2}-\alpha\right)\mathrm{d}z \end{array}\right]\hat{z}, \tag{3.40}$$

$$H_{ry} = \left[\int_{-H/2}^{H/2} j\frac{kI(z)l\sin\theta}{4\pi r(z)}\left[1+\frac{1}{jkr(z)}\right]e^{-jkr(z)}\mathrm{d}z\right]\hat{y}. \tag{3.41}$$

Using the above equations, the electric and magnetic fields as a function of the frequency for several points along the x axis are shown in figures 3.25 and 3.26, respectively.

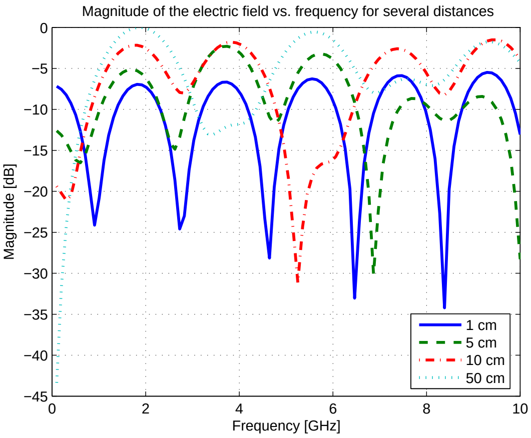

Figure 3.25: Magnitude of the electric field vs. frequency normalized to the distance

In order to validate this model, the obtained results are compared to the results obtained with simulations using NEC[2] (Numerical Electromagnetic Code). Figure 3.27 shows this comparison. From up to down (looking at the right side, 10 GHz) the curves correspond to 50, 1 and 5 cm.

For low frequencies the electric field is higher because the simulations have been done with a fixed transmission power for each frequency. The differences between

---

[2] NEC is a Method of Moments based code written by Jerry Burke and A. Poggio at Lawrence Livermore Labs in 1981, under contract to the US navy. NEC2 was later released to the public and is now available on most computing platforms.

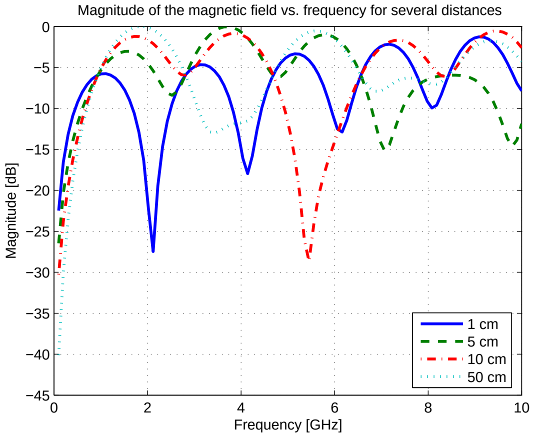

Figure 3.26: Magnitude of the magnetic field vs. frequency normalized to the distance

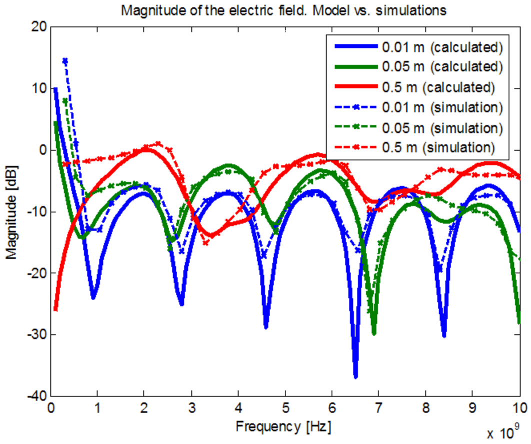

Figure 3.27: Comparison between calculated and simulated data

the calculated and simulated data are due to the differences in the current distribution (shape and magnitude). In the model a perfectly sinusoidal current has been assumed. In the simulations, the current distribution is calculated using the MoM (Method of Moments [12]). In figure 3.28 (magnitude) and figure 3.29 (phase) the current distribution for two frequencies are shown. In the magnitude figure, the sinusoidal shape corresponds to the 2 GHz frequency. In the phase figure, the 2 GHz distribution has -90 degrees phase except in the center (it has 90 degrees).

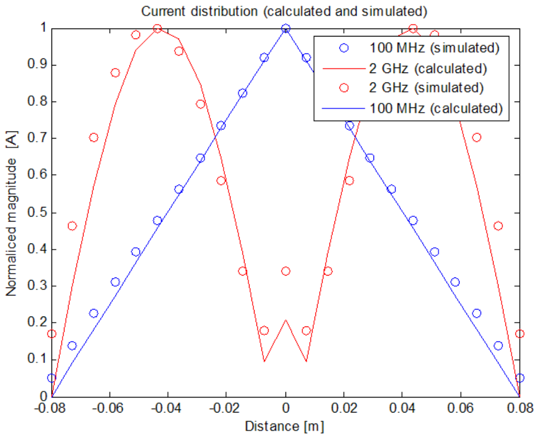

Figure 3.28: Current (magnitude) distribution along the dipole

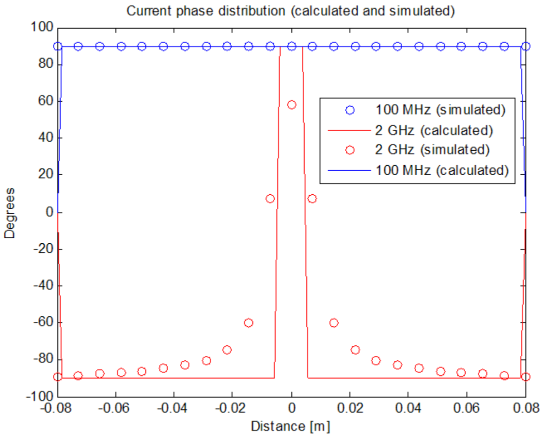

Figure 3.29: Current (phase) distribution along the dipole

3.2.2 Phase error between two dipoles

In the previous section, the phase error effect for one dipole has been evaluated, when the source is a point source. In this section the same effect will be derived when transmit and receive antenna are dipoles.

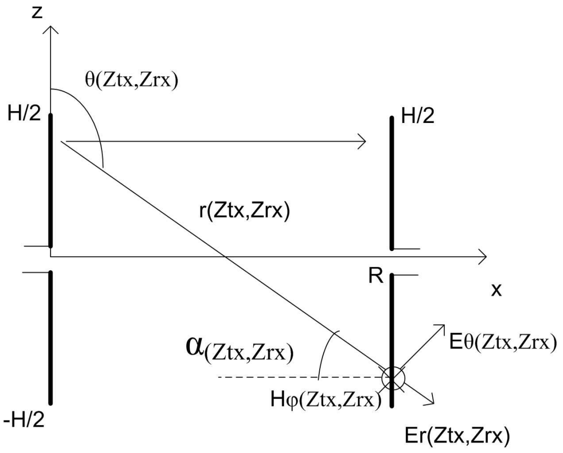

Figure 3.30: Phase error between two dipoles

Assuming the situation depicted in figure 3.30, the voltage in the receive dipole is given by [12]:

$$V_{rx} \propto \frac{1}{I_{rx_i}} \int_{-H/2}^{H/2} E_{rz}(z_{rx}) I_{rx}(z_{rx}) \mathrm{dz}_{\mathrm{rx}}, \tag{3.42}$$

where I_{rx_i} is the current at the feed point of the receive antenna, V_{rx} is the voltage at the terminals of the receiving dipole, I_{rx} is the current illumination of the receive dipole, and z_{rx} is the position along the receive dipole.

The electric field along the receive dipole is given by

$$E_{rz}(z_{rx}) = \begin{bmatrix} \int_{-H/2}^{H/2} E_\theta(z_{tx}, z_{rx}) \cos(\alpha(z_{tx}, z_{rx})) \mathrm{dz}_{\mathrm{tx}} + \\ \\ \int_{-H/2}^{H/2} E_r(z_{tx}, z_{rx}) \cos\left(\frac{\pi}{2} - \alpha(z_{tx}, z_{rx})\right) \mathrm{dz}_{\mathrm{tx}} \end{bmatrix} \hat{z}. \tag{3.43}$$

Substituting (2.15) and (2.16) in (3.43), the electric field along the dipole can be expressed as

$$E_{rz}(z_{rx}) = \left[\begin{array}{l}
\int_{-H/2}^{H/2} \Big(j\eta \frac{kI(z_{tx}) l \sin\theta(z_{tx}, z_{rx})}{4\pi r(z_{tx}, z_{rx})} \\
\quad \left[1 + \frac{1}{jkr(z_{tx}, z_{rx})} - \frac{1}{(kr(z_{tx}, z_{rx}))^2} \right] \\
\qquad e^{-jkr(z_{tx}, z_{rx})} \cos(\alpha(z_{tx}, z_{rx})) \Big) \mathrm{dz}_{\mathrm{tx}} + \\
\int_{-H/2}^{H/2} \Big(\eta \frac{I(z_{tx}) l \cos\theta(z_{tx}, z_{rx})}{2\pi r(z_{tx}, z_{rx})^2} \\
\quad \left[1 + \frac{1}{jkr(z_{tx}, z_{rx})} \right] \\
\qquad e^{-jkr(z_{tx}, z_{rx})} \cos\left(\frac{\pi}{2} - \alpha(z_{tx}, z_{rx}) \right) \Big) \mathrm{dz}_{\mathrm{tx}}
\end{array}\right] \hat{z}, \tag{3.44}$$

so, the voltage in the receive antenna is

$$V_{rx} \propto \frac{1}{I_{rx_i}} \int_{-H/2}^{H/2} \left[\begin{array}{l}
\int_{-H/2}^{H/2} \Big(j\eta \frac{kI(z_{tx}) l \sin\theta(z_{tx}, z_{rx})}{4\pi r(z_{tx}, z_{rx})} \\
\quad \left[1 + \frac{1}{jkr(z_{tx}, z_{rx})} - \frac{1}{(kr(z_{tx}, z_{rx}))^2} \right] \\
\qquad e^{-jkr(z_{tx}, z_{rx})} \cos(\alpha(z_{tx}, z_{rx})) \Big) \mathrm{dz}_{\mathrm{tx}} + \\
\int_{-H/2}^{H/2} \Big(\eta \frac{I(z_{tx}) l \cos\theta(z_{tx}, z_{rx})}{2\pi r(z_{tx}, z_{rx})^2} \\
\quad \left[1 + \frac{1}{jkr(z_{tx}, z_{rx})} \right] \\
\qquad e^{-jkr(z_{tx}, z_{rx})} \cos\left(\frac{\pi}{2} - \alpha(z_{tx}, z_{rx}) \right) \Big) \mathrm{dz}_{\mathrm{tx}}
\end{array}\right] I_{rx}(z_{rx}) \mathrm{dz}_{\mathrm{rx}}. \tag{3.45}$$

To calculate this, the "Induced EMF[3] Method" [12] can be used. This method is based on (3.42), but I_{rx} is assumed to be the ideal current distribution. Assuming an ideal sinusoidal current distribution, with value of 1 at the feed point, the voltage at the receive antenna will be as in figure 3.31.

---

[3] Electro Magnetic Fields

In figure 3.31, a distance of 5 cm between both dipoles has been assumed. The peaks at frequencies multiples of $1/H$ are due to the fact that the current distribution is normalized to 1 at the feed point for all the frequencies.

To validate this result, it is compared with a NEC simulation. To obtain the open-circuit voltage of a receive antenna due to a current in the transmit antenna using NEC, two simulations are needed (see figure 3.32).

In figure 3.32, the input impedance of the transmit dipole will be simulated for two situations. One with the second dipole open circuited, and the other with the second dipole short circuited.

Then, taking in mind the equivalent circuit for the coupling between two antennas [12] shown in figure 3.33, the mutual impedance between them can be obtained.

Where Z_{tx} is the impedance of the transmit antenna, Z_{rx} is the impedance of the

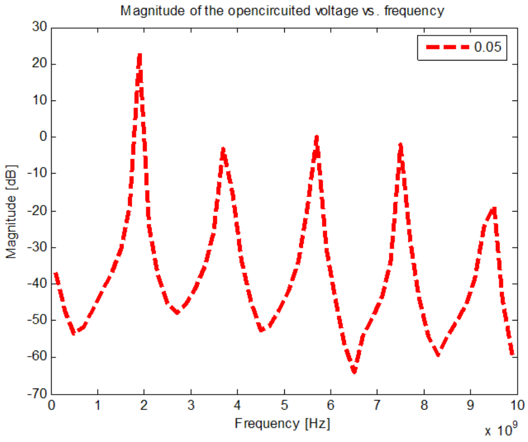

Figure 3.31: Open-circuit voltage at the receive antenna

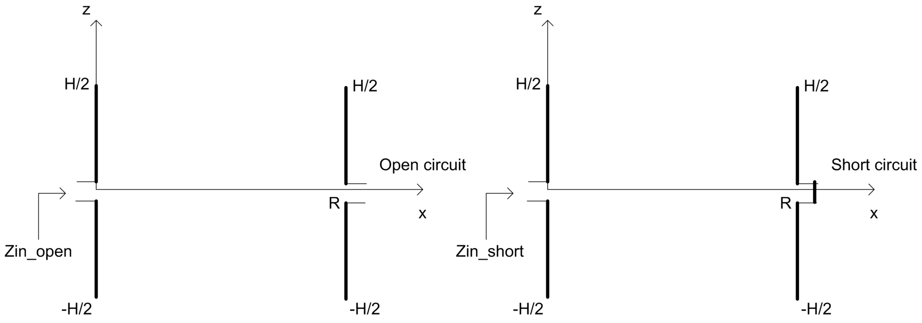

Figure 3.32: Schematic of the simulations in NEC

receive antenna, and Z_m is the mutual impedance between them.

According to figure 3.33 the input impedance of transmit antenna when the receive antenna is open-circuited will be Z_{tx}. Z_{rx} will be equal to Z_{tx} because both antennas are identical. Then, the input impedance of the transmit antenna when the receive antenna is short-circuited can be expressed as:

$$Z_{in\_short} = Z_{in\_open} - Z_m + \left(\frac{(Z_{in\_open} - Z_m)Z_m}{Z_{in\_open}}\right), \tag{3.46}$$

where Z_{in_short} is the input impedance of the transmit antenna when the receive antenna is short circuited, and Z_{in_open} is the input impedance when the receive antenna is open circuited. With some algebraic manipulation, the mutual impedance can be obtained,

$$|Z_m| = \left|\sqrt{-Z_{in\_short}Z_{in\_open} + Z_{in\_open}{}^2}\right|. \tag{3.47}$$

Assuming a constant input current in figure 3.33 as in the calculation to obtain figure 3.31, the open-circuit voltage at the terminals of the receive antenna will be proportional to Z_m.

The comparison between figure 3.31 and the results of the simulations with NEC are shown in figure 3.34.

The model has a good agreement with NEC simulation; hence this model can be used to estimate the variations in the received power within the near field region.

Now, the variations in the received voltage as a function of the distance will be analyzed.

In figure 3.35 the variations in the received power vs. distance for two 16 cm dipoles at 937.5 MHz ($\lambda/2$ dipole) are shown. The power has been normalized to the distance assuming a $1/r^2$ law (to appreciate the effect better).

For different frequencies, the effect is also different. In figure 3.36 the normalized received power for the same dipoles but for 2.5 GHz is shown.

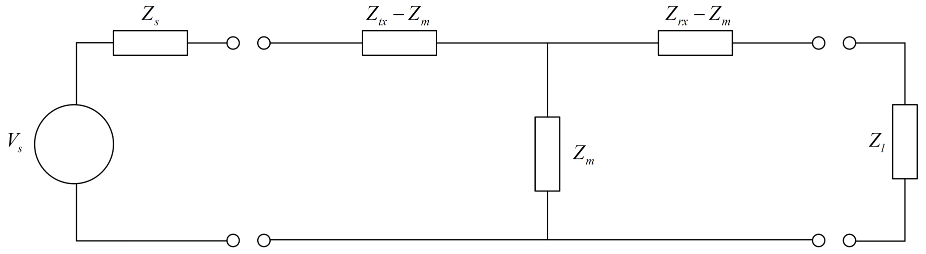

Figure 3.33: Equivalent circuit for the coupling between two antennas

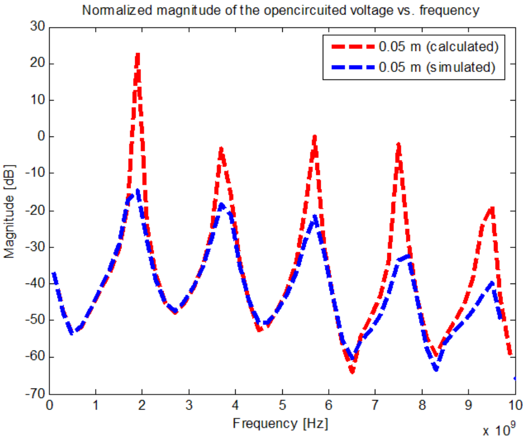

Figure 3.34: Comparison between the open-circuited voltages simulated and calculated

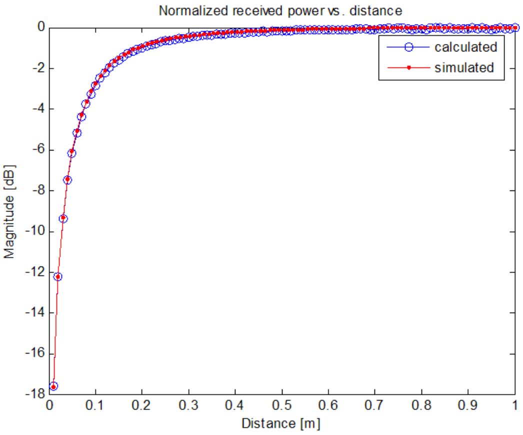

Figure 3.35: Normalized received power vs. distance at 937.5 MHz

The differences between the simulated and calculated data are due to the different current distribution.

The variation of the received power as a function of the distance and frequency is shown in figure 3.37. A constant power transmission for all the frequencies is assumed.

Now a Gaussian pulse of 200 ps is sent through the channel (antennas and free space). The received spectrum is integrated over the entire band (from 300 MHz to 10 GHz) to obtain the received power as a function of the distance (figure 3.38). The normalized spectrum of the Gaussian pulse is shown in figure 3.39.

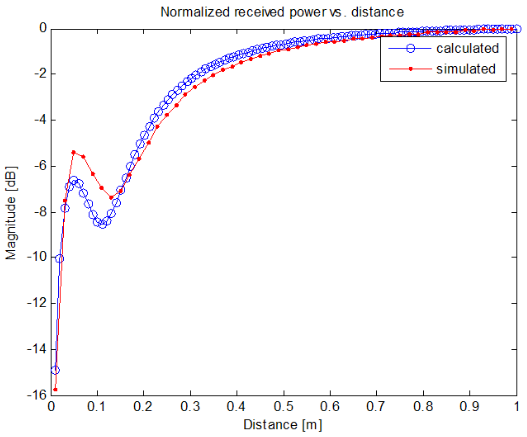

Figure 3.36: Normalized received power vs. distance at 2.5 GHz

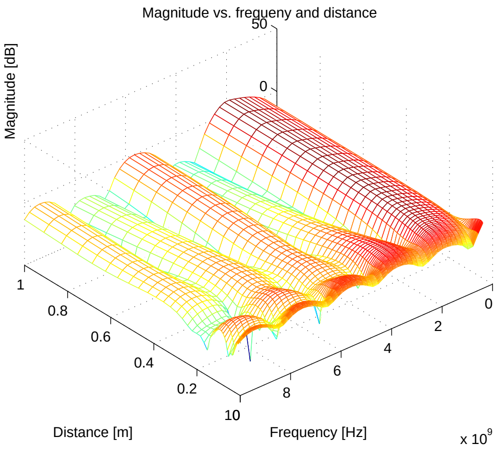

Figure 3.37: Power received vs. distance and frequency

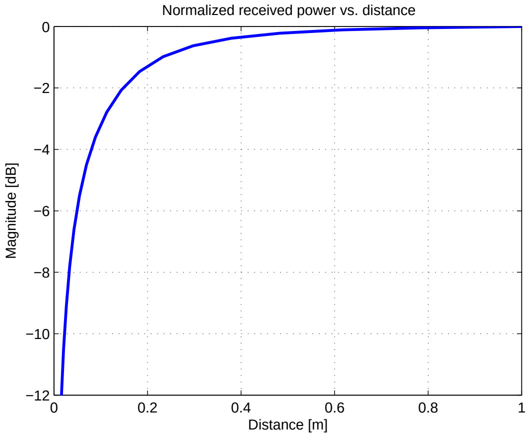

Figure 3.38: Normalized received power vs. distance

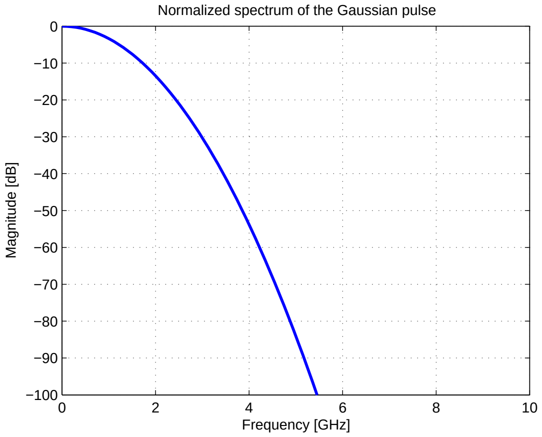

Figure 3.39: Normalized spectrum of the Gaussian pulse

In figure 3.38 we can see that the received power is smaller than the expected one for short distances, even with higher electric field terms near the antenna. The power has been normalized assuming a $1/r^2$ law, so, a flat response vs. distance means that the power decreases as $1/r^2$.

In figure 3.38 the frequency response of the antenna has not been taken into account, only the effect of the phase error and the contribution of the higher order terms of the electric field. For different pulse shapes (first Gaussian derivative and second Gaussian derivative), the normalized received power as a function of the distance is shown in figure 3.40. In figure 3.41, the spectrum of the different pulses is shown.

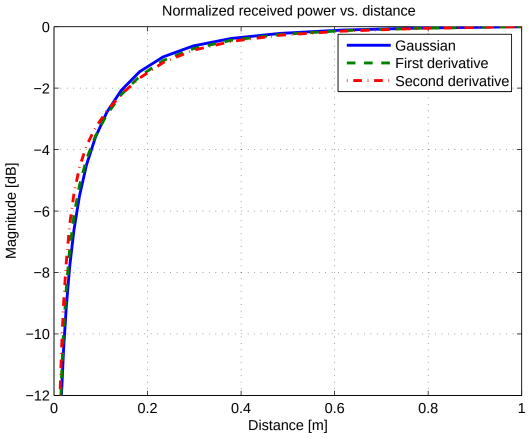

Figure 3.40: Normalized received power vs. distance for different pulses

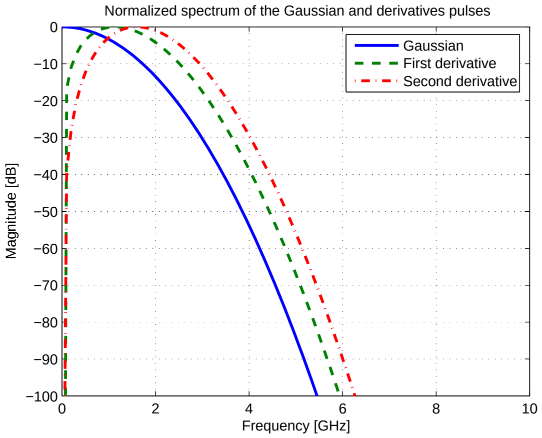

Figure 3.41: Normalized spectrum of the pulses

In figure 3.40 it can be seen that the effect is almost the same for Gaussian, first Gaussian derivative and second Gaussian derivative pulses. This is due to the fact that the behavior of the channel response in figure 3.37 is almost the same for the different frequency bands covered by the different pulses.

In figure 3.40, the normalized power decreases for small distances, but depending on the size of the antenna it can increase as well.

When the dipoles are smaller than the wavelength, the current distribution on its surface (ideally sinusoidal) is of the same sign, so the maximum power transfer occurs when the electric field on the surface of the dipole has the same phase in every point and in the near field the normalized received power will be smaller. When the dipole is larger than the wavelength, the current distribution on its surface can have different sign in different positions. In the near field, the phase difference of the electric field on the surface of the dipole may compensate the changes of sign of the current distribution and the normalized received power may be higher.

The higher order terms in the electric field are quite important for low frequencies because they are proportional to the wavelength. They are also important for very small antennas, because for small antennas the phase error is smaller but the higher order terms are the same.

However, for different kinds of antennas, the effect can be different. An important decision before to proceed with the simulations and measurements for two bi-conical antennas, is to decide which point of the antennas is taken as reference point in order to measure the distance between the antennas. For far field measurements, usually the reference would be the center of the antenna (due to the symmetry of the antenna), but in fact the reference for far field measurements is trivial. For near field measurements, the exact point is very important.

In order to decide the reference point, simulations with XFDT are done. A model of a bi-conical antenna is designed and compared with the real one used in the measurements (16 cm of diameter and 6.5 cm height). The comparison of the reflection coefficient and gain of the simulated and measured antenna ratify the agreement of the simulations with the measurements as it can be seen in figure 3.42.

According to Friis equation, the free space losses are proportional to $1/4\pi r^2$ and they are due to the spherical expansion of the radiated power. Then a good choice is to take as a reference, the point where the electro-magnetic wave begin to expand as an spherical wave. Figure 3.43 shows the electric field for different instants surrounding the antenna when a Gaussian pulse is sent.

It can be seen that inside the antenna, the wave is propagated likely an horn antenna or a waveguide. In this region, the expansion of the wave is not spherical, so the losses in that region are not the free space losses proportional to $1/4\pi r^2$. The point where the wave starts to expand as a spherical wave is the edge of the antenna,

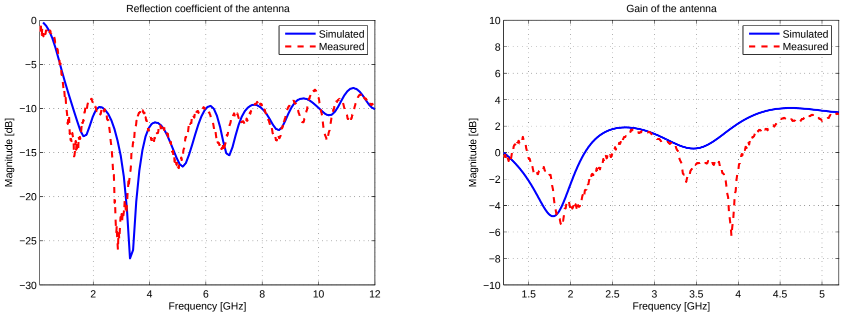

Figure 3.42: Reflection coefficient and gain of bi-conical antenna

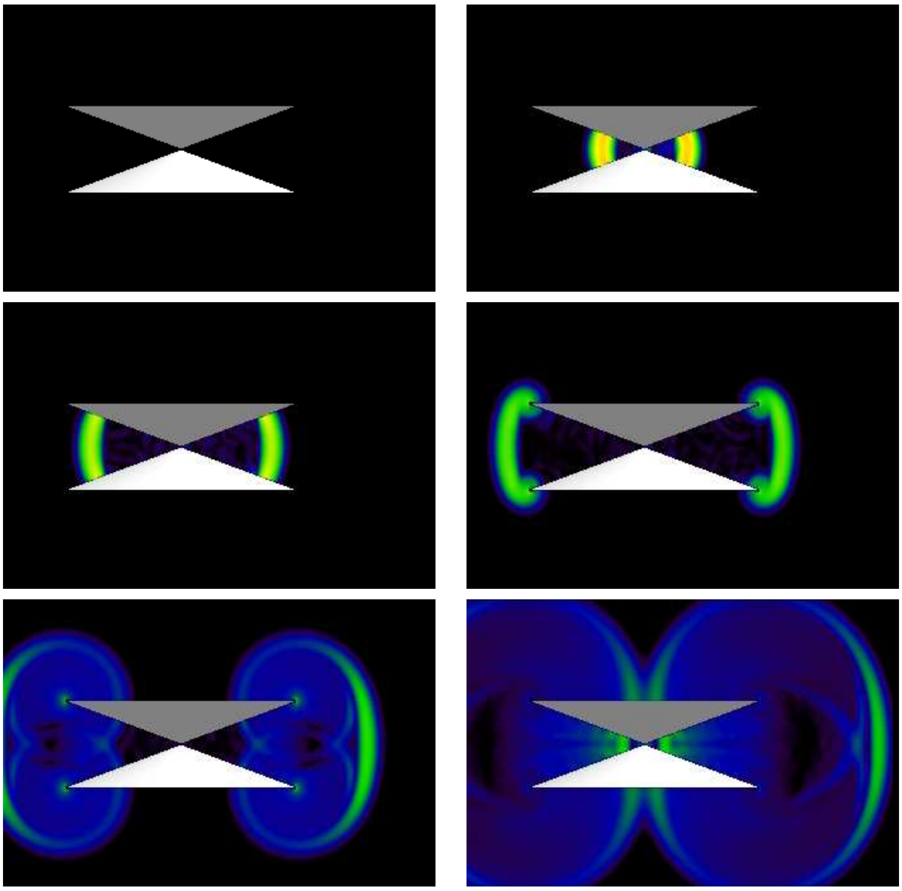

Figure 3.43: Electric field expansion

so in the simulations and measurements, the distance is referred to the edge of the antennas (the minimum distance between them).

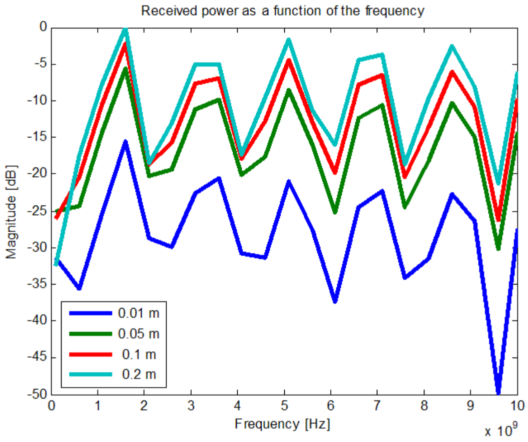

Figure 3.44: Received power as a function of the frequency for several distances

3.2.3 NEC simulations for a wire-simulation bi-conical antenna

Simulations for two wire-simulation bi-conical antennas have been done. The dimension of the antennas is 16 cm diameter and 6.5 cm height. The received power as a function of the distance between 100 MHz and 10 GHz is shown in figure 3.44. From up to down, the curves correspond to 20, 10, 5 and 1 cm. All the curves are normalized to the distance assuming a $1/r^2$ law.

Antennas designated to receive in a small bandwidth, as the dipole antenna, tend to have a flatter response in the near field (the power at the nulls in the far field tends to increase while the power at maxima tends to decrease, see figure 3.37; also some oscillations may happen). Based on this simulations, antennas designed to receive over a large bandwidth, as the wire-simulation bi-conical antenna, tend to have a similar frequency response in the near field but with a received power smaller than the expected.

3.2.4 Real measurements

Now real measurements with two bi-conical antennas (16 cm of diameter and 6.5 cm of height) for several distances are shown. In figure 3.45 the normalized frequency response of the two antennas for different distances is shown. The response has been normalized to the distance assuming a $1/r^2$ law. From down to up, the curves correspond to 0.5, 1, 2, 5, 10, 25, 50, 75 and 100 cm. For distances larger than 25 cm, the curves converge to the same.

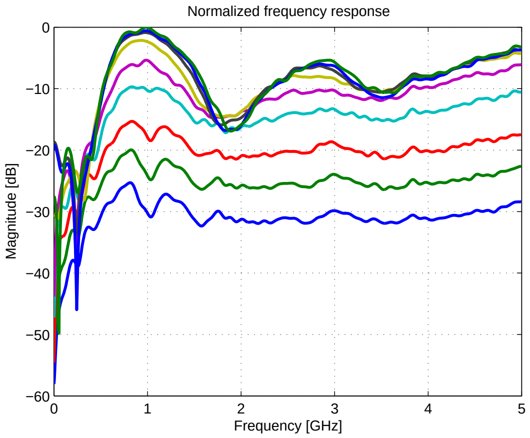

Figure 3.45: Normalized frequency response for several distances

In figure 3.45 it can be seen that for short distances (within the near field), the normalized frequency response is smaller than for large distances. The "null" in the far field (around 1.8 GHz) is not a null in the near field. The frequency response in the near field is more flat than in the far field, and it has some little oscillations (peaks at 1 GHz and 1.5 GHz).

The total amount of power over the entire band (between 0 Hz to 5 GHz) in the measurements as a function of the distance can be seen in figure 3.46.

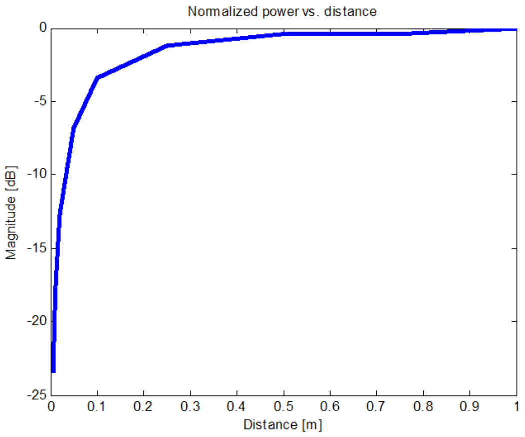

Figure 3.46: Normalized power vs. distance

Figure 3.47 shows the simulation of the total received power for the same band with two wire-simulation bi-conical antennas of the same size.

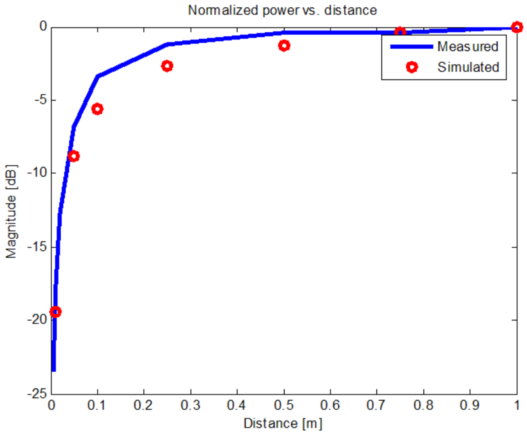

Figure 3.47: Comparison between measured and simulated received power

The model used in the simulations is shown in figure 3.48.

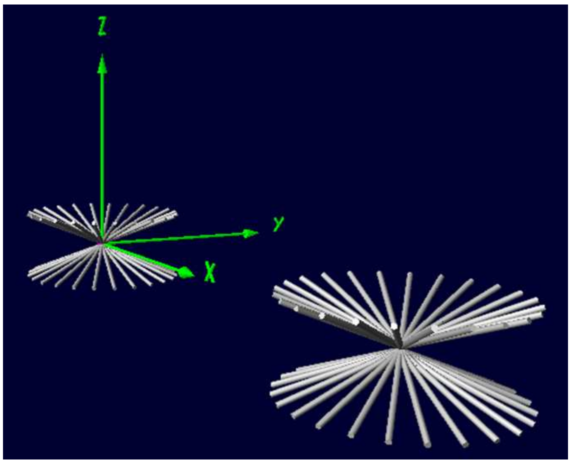

Figure 3.48: Model used in the NEC simulations

3.2.5 XFDTD simulation for a planar diamond antenna

In the previous simulations and measurements, “three-dimensional” antennas have been used. For this antennas, the reference point for the distance is taken at the edge of the antenna. For planar antennas as the diamond antennas there is no ambiguity in the reference point. Here we present the results of the simulations for two diamond antennas in order to ratify the behavior of the received power.

In this simulation, the antennas used are the same as in figure 3.17, but the dimensions of the triangles are 2 cm instead of 6 cm.

Figure 3.49 shows the received power from 3.1 GHz to 10.6 GHz as a function of the distance between the antennas. It can be seen that for short distances, the normalized received power is less than for large distances. No larger distances has been simulated due to the high resources needed for the simulations. It can be seen that the behavior is very similar to that of the bi-conical antennas, except the absolute distances can be much smaller.

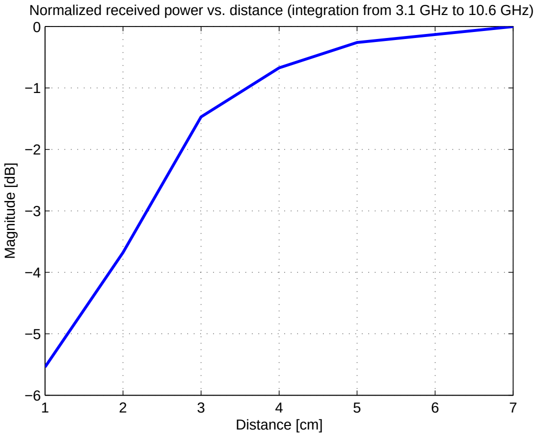

Figure 3.49: Normalized received power vs. distance for diamond antennas

3.3 Radiating and reactive fields

In the near field, the electric and magnetic fields have different behavior than in the far field. In the far field the electric and magnetic fields are related by the free space wave impedance (120π). The field's strength variation with the distance is as $1/r$. The electric and magnetic field's phase is linear with the distance and it varies as e^{-jkr} and both fields are in phase.

From equations (2.13) to (2.17) it can be seen that the electric and magnetic fields for distances within the near field region have a quite different behavior. There are components different of the $1/r$ component ($1/r^2$ and $1/r^3$ for the electric field and $1/r^2$ for the magnetic field). Moreover there is a radial electric field component that is neglected in the far field. Due to the radial component and the $1/r^n$ components the phase of the electric and magnetic fields are not linear with the distance and they are not in phase, in the near field.

The instantaneous Poynting vector $\mathscr{W}$ is defined as [12]:

$$\mathscr{W} = \mathscr{E} \times \mathscr{H}, \tag{3.48}$$

note that script letters are used to denote instantaneous fields and quantities. Where $\mathscr{E}$ is the instantaneous electric field intensity and $\mathscr{H}$ is the instantaneous magnetic field intensity.

For time harmonic variations of the form $e^{j\omega t}$, complex fields E and H are defined which are related to their instantaneous counterparts $\mathscr{E}$ and $\mathscr{H}$ by

$$\begin{aligned} \mathscr{E}(x,y,z;t) &= \mathrm{Re}\left[E(x,y,z)e^{j\omega t}\right], \qquad \text{and} & (3.49)\\ \mathscr{H}(x,y,z;t) &= \mathrm{Re}\left[H(x,y,z)e^{j\omega t}\right]. & (3.50) \end{aligned}$$

Using the above definitions of (3.49) and (3.50) and the identity

$$\mathrm{Re}\left[Ee^{j\omega t}\right] = \frac{1}{2}\left[Ee^{j\omega t} + E^* e^{-j\omega t}\right], \tag{3.51}$$

the time average Poynting vector (average radiated power density) can be written as

$$W_{av}(x,y,z) = \frac{1}{2}\mathrm{Re}\left[E \times H^*\right], \tag{3.52}$$

so, the average radiated power density will be maximum when the fields are in phase.

In this way, the electric and magnetic fields in the near field are higher than in far field (the variation is as $1/r^2$ and $1/r^3$), but the fields are mainly reactive and no radiating.

In this section differences between radiating and reactive fields are given. The effects on the transmission between antennas within the near field due to the reactive fields are explained.

3.3.1 Differences between radiating and reactive fields

Looking at equations (2.13) to (2.17) it can be observed that there are several terms in the electric and magnetic fields. The $1/r$ term is known as the radiating field component and the other terms are known as reactive or storage field components.

The main distinction between them is that storage or reactive fields store energy near the antenna while radiating fields propagate energy away through free space.

Radiating fields have both electric and magnetic field components. They are orthogonal to each other and to the direction of propagation and the ratio of the magnitude between electric and magnetic field is always $120\pi\ \Omega$.

Storage fields can be exclusively electric or magnetic or a combination of both, and the energy density stored in them always decay at a rate quicker than $1/r^2$.

Radiating fields spread out over a spherical surface. The total energy on a sphere of radius r is always the same. This means that the energy is propagating (radiating) through free space [16].

The total energy on a sphere for reactive fields decreases with distance, so it means that the energy is stored near the antenna.

Another distinction between storage and radiating fields is how the source reacts to an observer that absorbs some energy from the field.

For radiating fields, the source is not affected by the observers. Once the radiating field leaves the antenna, it is gone for ever, and the source is not affected if the energy is absorbed or not.

For reactive or stored fields the effect is different. Any time that an observer absorbs a part of the reactive field, extracting or diverting the energy, it will cause a reaction in the source circuit (for example a change in the input impedance of the antenna) [16].

In the far field, the stored or reactive field is negligible and the radiating field predominates ($r \gg \lambda/2\pi$). In the near field the radiating field is negligible compared to the reactive field. Figure 3.50 shows the progression of the different terms in equation (2.16) as a function of the distance. In this figure it can be seen which field predominates in the near and far field. All the terms have the same value at $\lambda/2\pi$.

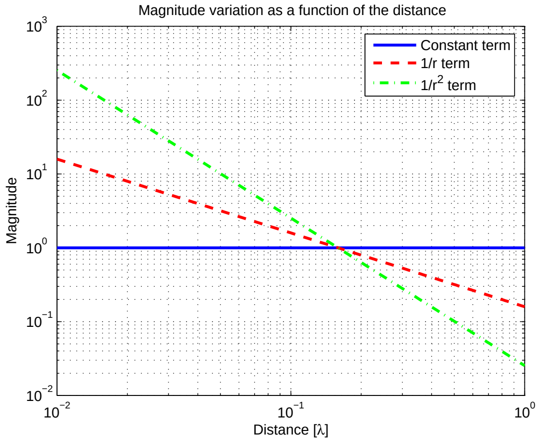

Figure 3.50: Radiating and reactive terms vs. distance

For distances below $\lambda/2\pi$ (point of the intersection) the reactive fields predominate. The coupling of the reactive static field to the receive antenna can be modelled as an electrical and/or magnetic coupling and it will affect the transmit antenna by changing its input impedance. This coupling will vary with the frequency. The changes in the input impedance of the transmit antenna may cause a mismatching for one or several frequencies, and a distortion in the frequency response of the antennas.

3.3.2 Simulations of a diamond antenna

Here we present the simulations of the reflection coefficient of a diamond antenna using XFDTD, and the same antenna when another identical antenna is placed at different distances from it.

Figure 3.51 shows the reflection coefficient of the antenna for different situations. It can be seen that for this antenna, the variations are not very important because the antenna is well matched for all situations. For different antennas the behavior can be different.

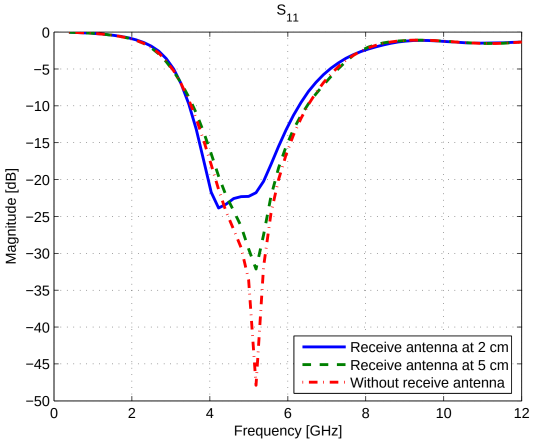

Figure 3.51: Variations of the reflection coefficient as a function of the distance between atennas

3.4 Conclusions

The results of the calculations, simulations and measurements of the received power versus distance are in good agreement. In the near field, due to the phase error and the different behavior of the electric field, the frequency response of the antenna may change. The nulls in the frequency response in the far field tend to disappear in the near field and the total power received over a large bandwidth tends to be less than the expected assuming a $1/r^2$ law although for a single frequency the response can be different (see figure 3.36).

The measurements and simulations for the received power for two bi-conical, wire-simulation bi-conical (see figure 3.47), and diamond antennas have a behavior similar to an exponential. In figure 3.52, the comparison between two simulations with wire-simulation bi-conical antennas of different sizes is shown. The “big antenna” is 16 cm of diameter and 6.5 cm of height. The “small antenna” is 8 cm diameter and 3.25 cm of height.

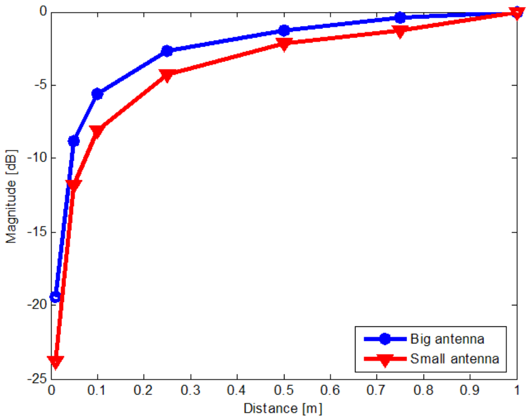

Figure 3.52: Comparison between bi-conical antennas of different sizes

The fact that for the small antenna the near field losses are higher than for the big one is because the frequency band over which the power is integrated is the same for both antennas, so the current distribution will be different for each one. If the comparison was for two different size dipoles, at the resonance frequency, the behavior would be as in figure 3.53 where the larger dipole receives less power.

A model to approximate this behavior will be explained in chapter 4.

On the other hand, the multiple reflections between antennas may cause pulse shape distortion when the antennas are close to each other, mainly for low frequencies and/or high gain antennas. Also it can be important for planar antennas due to the high reflection of the electromagnetic waves on flat structures. If low gain antennas (like bi-conical antennas used in the measurements) or high frequencies are used, the effect can be neglected.

Finally, the presence of other antennas within the near field, in which the reactive fields predominate (electric and/or magnetic fields), can affect the transmit antenna behavior changing its input impedance and radiation resistance [16].

This change in the input impedance of the antenna may cause a high reflection coefficient for some frequencies, and in turn, less radiation power causing distortion of the received signal.

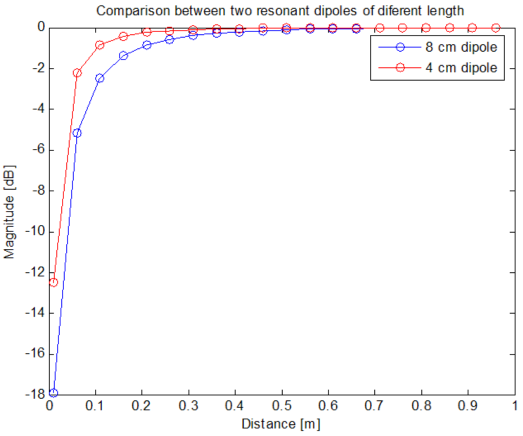

Figure 3.53: Comparison between two different resonant dipoles

Chapter 4

Models

In this chapter different models for very small distances are presented for the link budget and multipath reception. A closed form expression for the pulse shape distortion is not feasible due to the antenna dependence of the effect.

In section 4.1 a link budget model which models the exponential behavior described in section 3.2 is presented. The multipath reception for LOS in the near field is modelled in section 4.2.

4.1 Link budget model

Figure 3.47 and figure 3.52 show an exponential behavior of the link budget between two bi-conical antennas.

Different simulations have been carried out for different antenna sizes, and the distance decay constant τ_d of the exponential in equation (4.2) has been estimated and related to the antenna size for a given frequency band. Then, the total losses in the link budget can be expressed as

$$L_{total}(r) = L_{ff}(r)L_{nf}(r,D), \tag{4.1}$$

where L_{total} is the total loss of the channel, L_{ff} is the channel loss as a function of the distance without taking into account the near field effect (i.e. L_{ff} will be proportional to r^2), L_{nf} is the extra losses due to near field effects and D is the largest antenna size.

The extra losses of the near field effect can be modelled as:

$$L_{nf}(r) = 1 - e^{\frac{-r}{\tau_d(D)}}. \tag{4.2}$$

Figure 4.1 shows the approximation of this model to the simulations in figure 3.52. Higher losses are obtained for the small antenna in these simulations.

4.1.1 Simulations

Simulations for different bi-conical antennas have been done. L_{nf} has been calculated for them over a frequency band between 300 MHz and 5 GHz. The results are shown in figure 4.2.

Smaller antennas have higher losses in the simulations as it is shown in figure 4.2. The size in the legend of the figure corresponds to the diameter of the cones as it is shown in figure 4.3. The angle of the cone has been kept fixed, so, the height of the antenna is changed in the same way as the diameter.

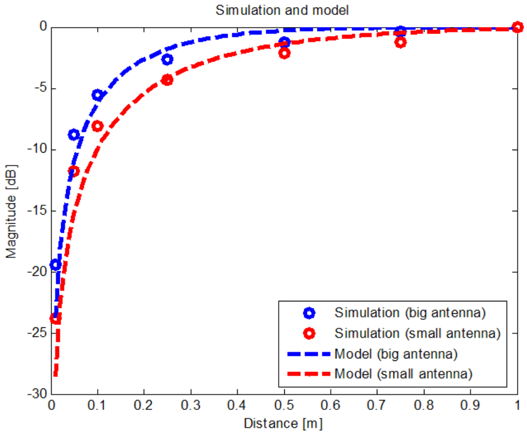

Figure 4.1: Simulation vs. model

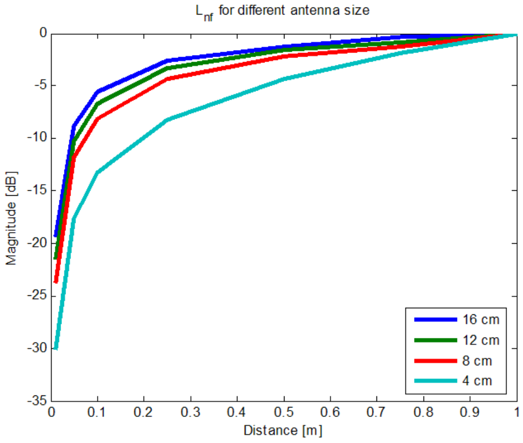

Figure 4.2: L_{nf} for different antenna sizes

The results obtained in figure 4.2 are not the expected results. From this figure it is observed that the L_{nf} is larger for small antennas than for large antennas. Whereas in section 3.2 is explained that the phase error is larger for large antennas. This is due to the fact that the frequency band is the same for all the antennas and the current distribution along the surface of the antenna is different. In a real antenna the frequency band covered by different antenna sizes would be different. In figure 4.4 this effect is depicted for two different dipoles and a single frequency.

For the shortest antenna (left), its obvious that in the near field the received power always will be less than in the far field, because the current distribution along the surface of the antenna has always the same sign. For the largest one (right) this

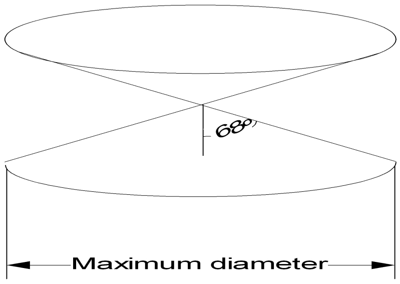

Figure 4.3: Bi-conical antennas dimensions

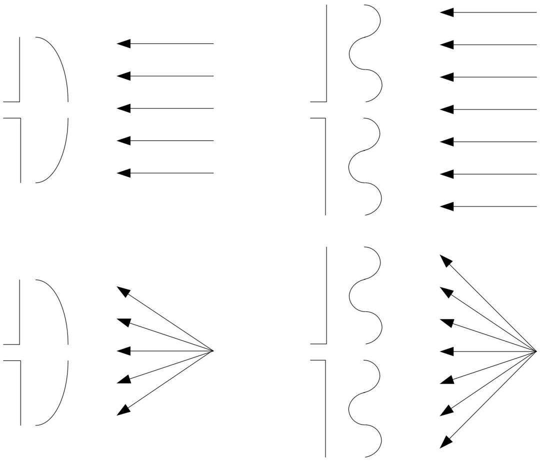

Figure 4.4: Phase error effect for different antennas sizes and a single frequency

is not true, because the current distribution has different phase depending of the position. For the large antenna the phase error in the near field can be compensated (in part) by the phase changes in the current distribution and the L_{nf} for a single frequency can have some oscillations. For these reasons, the L_{nf} can be higher for the small antenna than for the large one. Bi-conical antennas are designed to have a large bandwidth (without nulls for some frequencies as in the case of the dipole) and the L_{nf} tends to increase for small distances without oscillations as can be seen in figure 4.2.

Distance decay constant τ_d has been estimated for the simulated cases in figure 4.2. The comparison between the simulations and the model is shown in figure 4.5 (dotted lines are the exponential model and solid lines are the simulations). From up to down, the curves correspond to 16, 12, 8 and 4 cm.

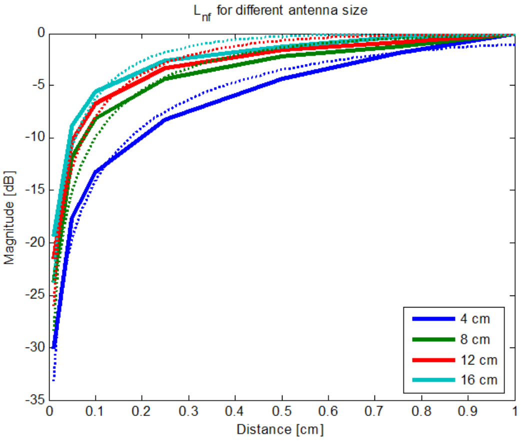

Figure 4.5: Simulations and exponential model for different antenna sizes

In figure 4.6 it can be seen that τ_d tends to increase for small antennas and decrease for large antennas, but there are too few events to extract any conclusions.

The comparison between the results in figure 3.47 and the model can be seen in figure 4.7.

The distance decay constant τ_d for the simulations in figure 4.7 is 0.15 and for the measurement is 0.0875.

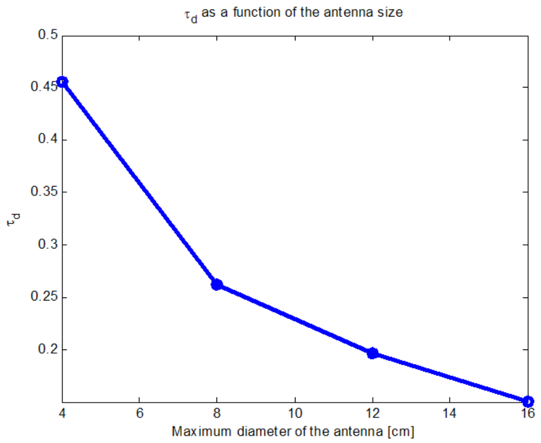

Figure 4.6: τ_d as a function of the antenna size

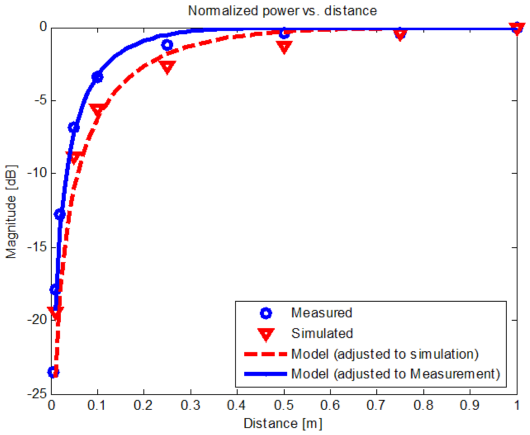

Figure 4.7: Comparison between measurement, simulation and model

4.2 Multipath reception

In several reports an UWB channel model as in equation (4.3) is proposed,

$$h(t) = \sum_{i=1}^{N} a_i \delta(t - \tau_i), \tag{4.3}$$

where $h(t)$ is the time domain channel impulse response and the parameters of n-th path a_n, τ_n and N are amplitude, delay and number of relevant multipath components, respectively.

The multipath components reaching the receive antenna can be subdivided into two main groups: near and far field components. Therefore, the channel impulse response can be written as:

$$h(t) = \sum_{i=1}^{N_{NF}} a_{NF_i} \delta(t - \tau_{NF_i}) + \sum_{j=1}^{N_{FF}} a_{FF_j} \delta(t - \tau_{FF_j}), \tag{4.4}$$

where NF and FF sub-index mean near and far field, respectively, and the parameters are the same as in equation (4.3).

Furthermore, the near field components can be subdivided also into two sub-groups, namely the direct and reflected components. Finally, the time domain impulse response can be write as:

$$h(t) = a_{dir} \delta(t - \tau_{dir}) + \sum_{i=2}^{N_{NF}} a_{NF_i} \delta(t - \tau_{NF_i}) + \sum_{j=1}^{N_{FF}} a_{FF_j} \delta(t - \tau_{FF_j}), \tag{4.5}$$

where the sub-index dir means direct path component.

Based on equation (4.5), the different reflections will be analyzed in the following sub-sections.

4.2.1 Far field reflections

When transmit and receive antennas are close to each other, the received power from the direct path will be very high compared with the reflected power from objects situated in the far field.

For example if both antennas are situated at 10 cm of each other, and there is a metallic object situated at 1 m from both antennas as in figure 4.8, where r_1, r_2 and r_d are the respective distances between the antennas and the object. Assuming that the received power is proportional to $1/r^2$ and polarization matching, the received power from the LOS and reflected ray will be [12]:

$$
\begin{aligned}
P_{LOS} &= L_{NF} P_{tx} G_{tx}(\theta_{tx}, \phi_{tx}) G_{rx}(\theta_{rx}, \phi_{rx}) \left(\frac{\lambda}{4\pi r_d}\right)^2, \quad \text{and} && (4.6)\\
P_{refl} &= P_{tx} G_{tx}(\theta'_{tx}, \phi'_{tx}) G_{rx}(\theta'_{rx}, \phi'_{rx}) \frac{\sigma_{refl}}{4\pi} \left(\frac{\lambda}{4\pi r_1 r_2}\right)^2, && (4.7)
\end{aligned}
$$

where L_{NF} are the extra losses in the near field, σ_{refl} is the radar cross section of the metallic object. Assuming r_1 and r_2 equal to 1 m, r_d (distance between antennas) equals to 10 cm, two isotropic antennas, and the metallic object of 27×27 cm^2 (maximum dimension to fulfill the far field condition $r > 2D^2/\lambda$ at 1 GHz) with a reflection coefficient of 1, the ratio between P_{refl} and P_{LOS} will be:

$$
\begin{aligned}
\frac{P_{refl}}{P_{LOS}} &= \frac{1}{L_{NF}} \frac{\sigma_{refl}}{4\pi} \left(\frac{r_d}{r_1 r_2}\right)^2 = \frac{(A_{obj} \sin\alpha)^2}{\lambda^2} \left(\frac{r_d}{r_1 r_2}\right)^2, && (4.8)\\
\frac{P_{refl}}{P_{LOS}} &= \frac{1}{L_{NF}} \frac{\left(0.27^2 \sin\left(\arctan\left(\frac{1}{0.05}\right)\right)\right)^2}{0.3^2} \left(\frac{0.1}{1}\right)^2 = \frac{0.00059}{L_{NF}}, && (4.9)
\end{aligned}
$$

assuming L_{NF} of -5 dB as for the bi-conical antennas used in the measurements, the reflected power would be about -27 dB below the direct path.

If the metallic object was larger, the antennas would be situated in the near field of the object, and there would be some phase error in the power scattered by the metallic object to the receive antenna, so this formulation would not be valid, as it is explained in section 3.2.

For an UWB signal (assuming a frequency band from 300 MHz to 10 GHz), the maximum dimension to fulfil the far field condition (determined by the maximum

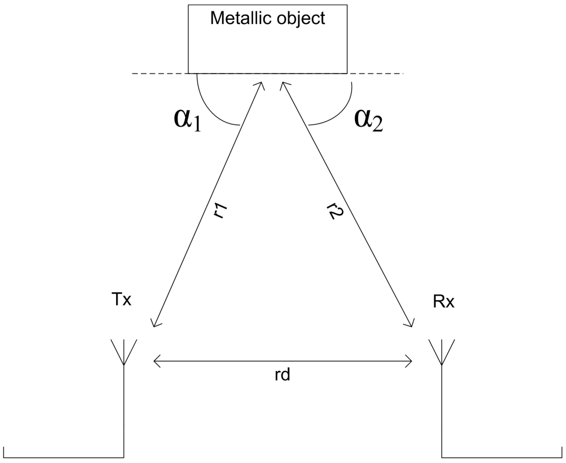

Figure 4.8: Far field reflections

frequency) for a metallic object situated at 1 m from both antennas would be 8.5 × 8.5 cm^2. Now, the received power from the direct and reflected path will be:

$$P_{LOS} = L_{NF} \int_{\lambda_{min}}^{\lambda_{max}} P_{tx} G_{tx}(\theta_{tx}, \phi_{tx}) G_{rx}(\theta_{rx}, \phi_{rx}) \left(\frac{\lambda}{4\pi r_d} \right)^2 \mathrm{d}\lambda, \text{and} \quad (4.10)$$

$$P_{refl} = \int_{\lambda_{min}}^{\lambda_{max}} P_{tx} G_{tx}(\theta'_{tx}, \phi'_{tx}) G_{rx}(\theta'_{rx}, \phi'_{rx}) \frac{\sigma_{refl}}{4\pi} \left(\frac{\lambda}{4\pi r_1 r_2} \right)^2 \mathrm{d}\lambda. \quad (4.11)$$

The Rician K factor, defined as the ratio of the power in the stronger component to the total power in the other components, would be:

$$\frac{P_{LOS}}{P_{refl}} = 6.6 \cdot 10^5 L_{NF}, \quad (4.12)$$

assuming L_{NF} of -5 dB as for the bi-conical antennas used in the measurements, the K factor would be about 53 dB.

4.2.2 Near field reflections

In the previous section, is shown that far field reflections can be neglected because their amplitudes are very small compared with the near field components. A simple derivation is done for a reflection from an object situated in the far field. Such a derivation will be slightly different if the object is situated in the near field. The situation is depicted in figure 4.9.

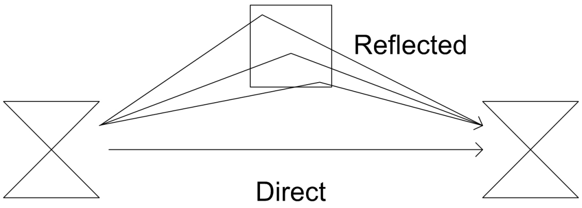

Figure 4.9: Near field reflection

The same phase error effect that appears in the antennas, will appear also in the reflector object. This phase error is translated in different rays reaching the receive antenna with different phase and then, the total amount of power reaching the antenna from the object will be less than the expected if the behavior was as for an object in the far field.

According to the situation depicted in figure 4.9, the direct path power will be:

$$P_{LOS} = L_{NF} \int_{\lambda_{min}}^{\lambda_{max}} P_{tx} G_{tx} G_{rx} \left(\frac{\lambda}{4\pi r_d} \right)^2 \mathrm{d}\lambda, \quad (4.13)$$

where L_{NF} is the extra near field loss, P_{tx} is the transmitted power, G_{tx} and G_{rx} are the transmit and receive antenna gain, respectively, r_d is the distance between the antennas and λ_{min} and λ_{max} are the minimum and maximum wavelength in the frequency band (a constant transmitted power for all the frequencies is assumed).

When the reflecting object is in the near field two effect will appear: one of them is the known phase error (in the electric field radiated by the transmit antenna to the object, and also from the object to the receive antenna), and the other effect is that the incident and reflected angles are not the same as is shown in figure 4.10. These effects will introduce extra losses in the reflected power.

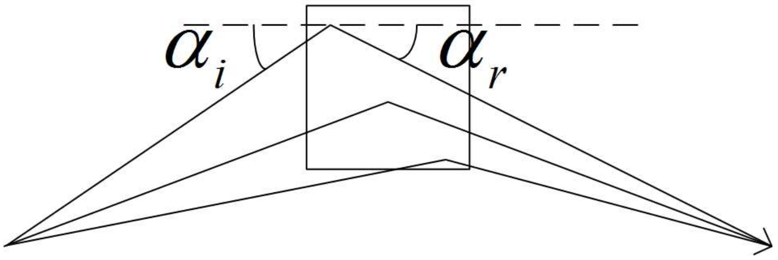

Figure 4.10: Incident and reflected angle

For a small object the incident and reflected angle can be assumed equals. To calculate the reflected power taking into accout the phase error, the situation in figure 4.11 will be assumed.

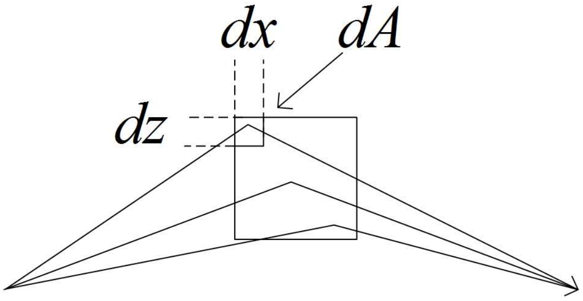

Figure 4.11: Multiple division of the reflecting object

In figure 4.11 dx is the differential in the x axis, dz is the differential in the z axis and dA is the surface differential defined as:

$$\mathrm{dA} = \mathrm{dxdz}. \tag{4.14}$$

The total power reaching the receive antenna can be calculated as an integral of all the reflections on the surface of the object.

Then,

$$\begin{aligned}\mathrm{dE}_{\mathrm{refl}}(\lambda) =& (Z_0P_{tx}(\lambda))^{\frac{1}{2}}\,(G_{tx})^{\frac{1}{2}}\,\frac{e^{-jkd_1(A)}}{\sqrt{4\pi}d_1(A)}(\mathrm{dA})^{\frac{1}{2}}\cdot \\ & \left(\frac{4\pi\mathrm{dA}}{\lambda^2}\right)^{\frac{1}{2}}\frac{e^{-jkd_2(A)}}{\sqrt{4\pi}d_2(A)}\left(\frac{\lambda^2G_{rx}}{4\pi}\right)^{\frac{1}{2}}, \qquad (4.15)\\ \mathrm{dE}_{\mathrm{refl}}(\lambda) =&(Z_0P_{tx}(\lambda))^{\frac{1}{2}}(G_{tx}G_{rx})^{\frac{1}{2}}\frac{e^{-jk(d_1(A)+d_2(A))}}{4\pi d_1(A)d_2(A)}\mathrm{dA}, \qquad (4.16)\\ \mathrm{dP}_{\mathrm{refl}}(\lambda) =&\frac{|\mathrm{dE}_{\mathrm{refl}}(\lambda)|^2}{Z_0} = P_{tx}(\lambda)G_{tx}G_{rx}\left|\frac{e^{-jk(d_1(A)+d_2(A))}}{4\pi d_1(A)d_2(A)}\mathrm{dA}\right|^2, \qquad (4.17)\\ P_{refl}(\lambda) =&P_{tx}(\lambda)G_{tx}G_{rx}\left|\int_A\frac{e^{-jk(d_1(A)+d_2(A))}}{4\pi d_1(A)d_2(A)}\mathrm{dA}\right|^2, \qquad (4.18)\\ P_{refl}(\lambda) =&P_{tx}(\lambda)G_{tx}G_{rx}\Bigg|\int_{z_{min}}^{z_{max}}\int_{x_{min}}^{x_{max}} \\ & \frac{e^{-jk\left((x^2+y^2+z^2)^{\frac{1}{2}}+\left(\left(\frac{R}{2}-x\right)^2+y^2+z^2\right)^{\frac{1}{2}}\right)}}{4\pi(x^2+y^2+z^2)^{\frac{1}{2}}\left(\left(\frac{R}{2}-x\right)^2+y^2+z^2\right)^{\frac{1}{2}}}\mathrm{dxdz}\Bigg|^2, \qquad (4.19)\end{aligned}$$

where E_{refl} is the reflected electric field and d_1 and d_2 are the distances from the transmit antenna to the reflecting object and from the object to the receive antenna, respectively.

The reflected power is not frequency dependent because the frequency dependence of the free space loss is compensated with the frequency dependence of the object's radar cross section. The reflected power over the entire band is then,

$$\begin{aligned}P_{refl} =& \int_{\lambda_{min}}^{\lambda_{max}} P_{tx}(\lambda)G_{tx}G_{rx}\Bigg|\int_{z_{min}}^{z_{max}}\int_{x_{min}}^{x_{max}} \\ & \frac{e^{-jk\left((x^2+y^2+z^2)^{\frac{1}{2}}+\left(\left(\frac{R}{2}-x\right)^2+y^2+z^2\right)^{\frac{1}{2}}\right)}}{4\pi(x^2+y^2+z^2)^{\frac{1}{2}}\left(\left(\frac{R}{2}-x\right)^2+y^2+z^2\right)^{\frac{1}{2}}}\mathrm{dxdz}\Bigg|^2 \mathrm{d}\lambda. \qquad (4.20)\end{aligned}$$

According to equations (4.13) and (4.20), the Rician K factor can be calculated.

Assuming an object situated at 10 cm from both antennas, separated also 10 cm from each other. The dimension of the object is 3 × 3 cm^2 to avoid the incident and reflected angle differences. The two antennas are isotropic with unit gain. This situation is depicted in figure 4.12.

Using the above formulas, the Rician K factor will be:

$$K = \frac{P_{LOS}}{P_{refl}} \approx 27\ dB + L_{NF}. \tag{4.21}$$

Assuming 5 dB of extra losses in the direct path, as for the bi-conical antennas used in the measurements ($L_{NF} = -5$ dB), the K factor would be about 22 dB.

4.2.3 Model

According to the previous results, most of the power is contained in the direct LOS path, and then, the path loss matches up with the link budget.

Then for LOS situations where the antennas are situated in the near field of each other, the channel impulse response in equation (4.3) can be written as:

$$h(t) = a_{dir}\delta(t - \tau_{dir}), \tag{4.22}$$

where a_{dir} will be an aleatory variable with mean given by the link budget model. In UWB channels each resolved multipath components is due to a small number of scatters and then the amplitude distribution of a_{dir} may differ of a Rician distribution (assumed in narrowband channels in this situations). In [17] they present that the best fit is a Nakagami distribution, used to model the magnitude statistics in radio when the conditions of the central limit theorem are not fulfilled.

Based on these results, we can conclude that the direct path will contain the most of the power and the reflections will have a negligible effect.

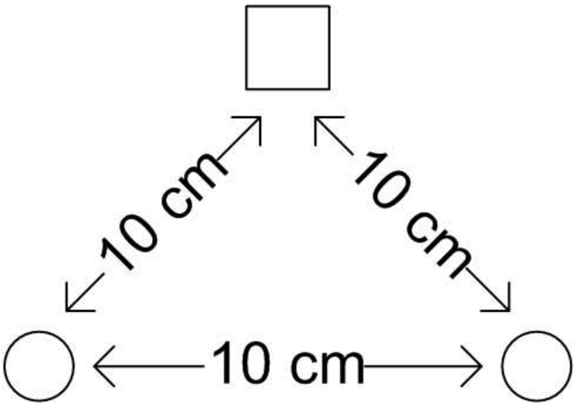

Figure 4.12: Near field reflection situation

Chapter 5

Measurements

THis *chapter presents the results of a set of time domain measurements carried out in order to validate the models given in chapter 4. Link budget measurements were performed where only the direct path was measured in order to extract the variation in the received power as a function of the distance. Also, using the same measurements the pulse shape distortion has been analyzed.*

Channel measurements in an office environment were carried out as well. These measurements comprise both LOS and NLOS situations.

The chapter is organized as follows. Section 5.1 presents the results of the link budget measurements. Section 5.2 analyzes the pulse shape distortion produced in the near field. In section 5.3 a brief explanation of the data processing performed is given in order to obtain the channel parameters. Finally section 5.4 gives the results obtained from the channel measurements.

5.1 Link budget measurements

In this section, link budget measurements for different antennas are shown. These measurements are fitted with the model given in section 4.1.

5.1.1 Big bi-conical antenna

Figure 5.1 shows the measured antennas. The dimension of the antennas is 16 cm diameter and 6.5 cm height. The antennas were situated on several Styrofoam boards in order to keep them at more than one meter from the ground. Also there were no objects at less than one meter from the antennas. In this way, the reflections of the walls and/or objects can be removed using an appropriate time window.

The received power until 10 GHz was integrated in order to obtain the received power as a function of the distance between the antennas.

Figure 5.2 shows the normalized received power as a function of the distance. The received power is normalized to the distance assuming a $1/r^2$ law. The obtained curve is fitted to the model given in section 4.1 (in least squares meaning) in order to obtain the distance decay constant τ_d that best fit the measurements. The curves can be interpreted as the extra losses produced by the near field effects.

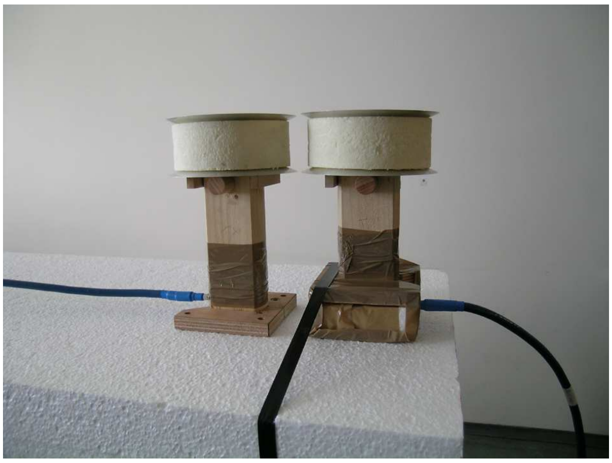

Figure 5.1: Situation of the antennas

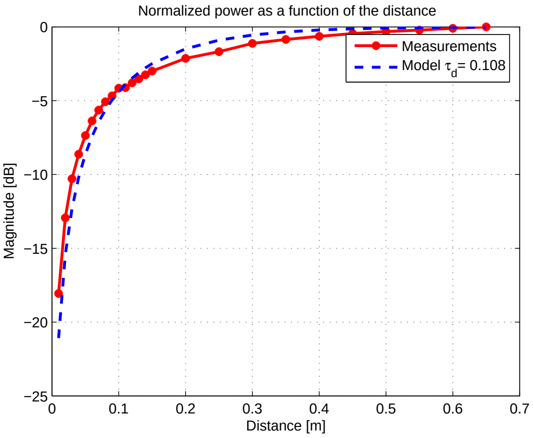

Figure 5.2: Normalized received power as a function of the distance

5.1.2 Middle bi-conical antenna

The middle antenna was 7.5 cm diameter and 3.2 cm height. The measurement procedure was the same as before. The received power is normalized to the distance. The results are shown in figure 5.3. Also the best fit to the link budget model is given.

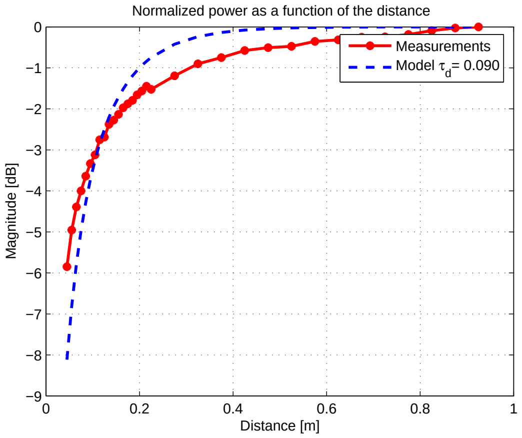

Figure 5.3: Normalized received power as a function of the distance

The behavior of the extra losses for the near field is also an exponential behavior. For the middle antenna, the extra losses are smaller than for the big antenna. This does not agree with the results of the simulations in 4.1 (in such simulations small antennas have higher losses), mainly because in that simulations the antennas were assumed to be working in the same frequency band, and in the real measurements, the frequency band covered by the antennas is different.

5.1.3 Small bi-conical antenna

The small antenna was 2.6 cm diameter and 0.8 cm height. The measurement procedure was the same as before. The received power is normalized to the distance. Figure 5.4 shows the results of the measurements. Also the best fit to the link budget model is presented.

It can be seen that for the small antenna, the extra losses in the near field are quite small. For this reason, the little variations around the model are more clear.

5.2 Pulse shape

In this section the pulse shape distortion is analyzed for different antennas. We want to remark that a closed expression for the pulse shape distortion is not feasible due to the strong dependence on the antenna structure.

5.2.1 Big antenna pulse shape distortion

Figure 5.5 shows the time domain distortion of the received pulse shape for different distances.

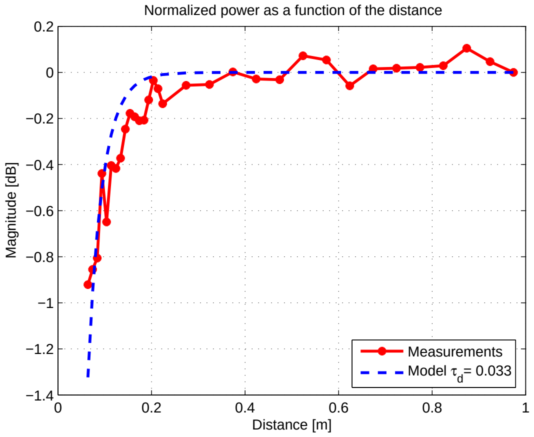

Figure 5.4: Normalized received power as a function of the distance

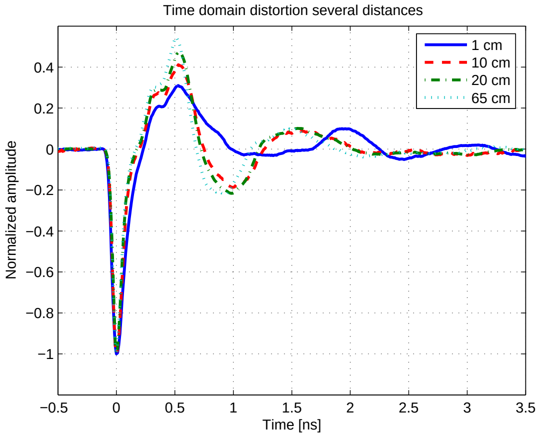

Figure 5.5: Time domain distortion

Figure 5.5 shows the distortion produced when the antennas are very close to each other. For distances larger than 10 cm, the distortion is negligible, but for distances below 10 cm the distortion is quite significant.

The pulse shape distortion can be seen also in frequency domain. The normalized received spectrum for the same distances is represented in figure 5.6.

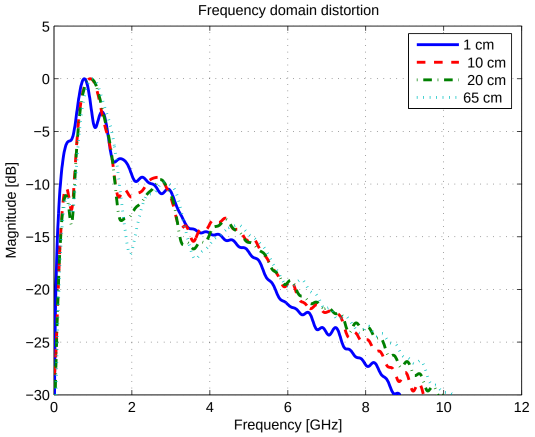

Figure 5.6: Frequency domain distortion

It is observed that for frequencies beyond 5 GHz the spectrum is almost the same. The main distortion is produced around 2 GHz and 3.5 GHz. Namely, these frequencies are attenuated in the far field. This agree with the phase error effect explained in 3.2.

Using the frequency band imposed by the FCC (from 3.1 GHz to 10.6 GHz) the distortion can be reduced since the higher distortion is around 2 GHz.

5.2.2 Middle antenna pulse shape distortion

Figure 5.7 shows the time domain distortion in the received pulse.

It can be seen that the distortion is not as strong as before. Also the minimum measured distance is not as small as before.

Figure 5.8 shows the same effect in frequency domain. As before, the main distortion in the frequency domain is located around the nulls in the far field (about 1 and 4 GHz). This again agrees with the phase error effect explained in section 3.2.

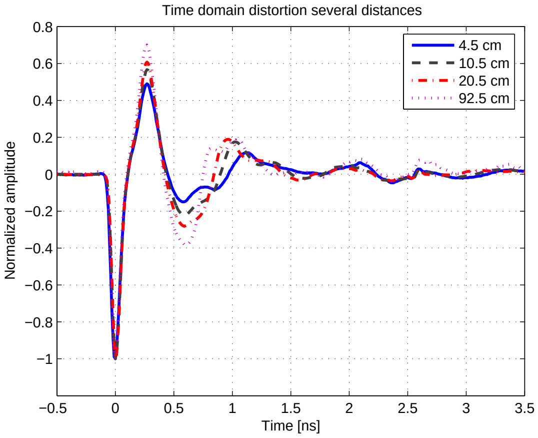

Figure 5.7: Time domain distortion

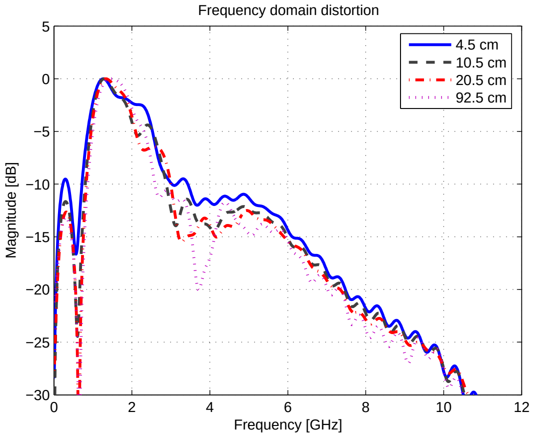

Figure 5.8: Frequency domain distortion

5.2.3 Small antenna pulse shape distortion

For the small antenna, the received pulse shape is shown in figure 5.9. Looking at the time domain distortion one can guess that the main distortion will be at low frequencies.

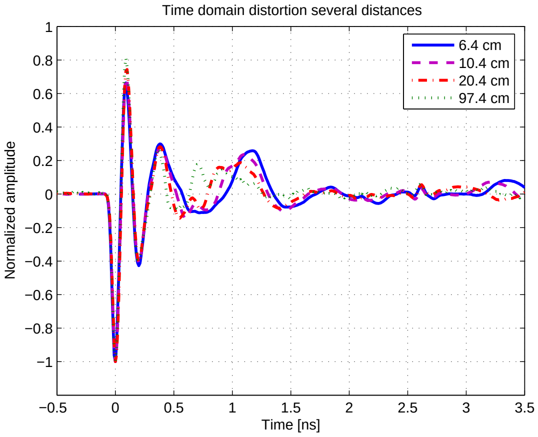

Figure 5.9: Time domain distortion

Figure 5.10 shows the distortion in frequency domain. As it was expected, the received spectrum for frequencies beyond 3 GHz is almost the same. It can be seen also that a null around 1 GHz in the far field is shifted to lower frequencies in the near field, and the received power between 1 and 2 GHz is incremented by almost 10 dB. Again the main distortion is around the far field nulls.

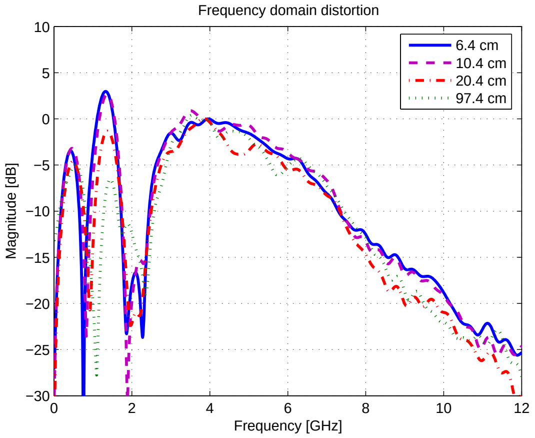

Figure 5.10: Frequency domain distortion

5.3 Data processing

The channel measurements had to be processed to obtain the relevant channel parameters, namely RMS delay spread, Ricean K factor and path loss exponent. These parameters are obtained from the power delay profile (the received power as a function of the excess delay defined as the square of the channel impulse response). In order to obtain the channel impulse response the first step is to process the different measurements taken for each position using the OTI[1] method described in [18] to obtain the complete channel response at each distance, then a digital low pass filter is used to remove the noise above 10.6 GHz; after that a subtractive deconvolution algorithm CLEAN was used as is described in [19]. The CLEAN algorithm was chosen because it gave the better results compared to ESPRIT and Inverse filtering + CLEAN in the simulations carried out. For more detail about the comparison, the reader is referred to appendix A.

5.4 Channel measurements

In this section the results of the channel measurements in an office scenario for different situations (comprising LOS and NLOS) are presented. Table 5.1 shows a summary of the different measurements performed. The DMR field means if the antennas were situated with their maximum direction of radiation directed to each other.

The section is divided into three subsections describing the path loss measurements, K-factor and RMS delay spread, respectively.

5.4.1 Path loss

For the path loss, a simple model is used. It assumes a relation between the average received signal power Pr and the distance d between Tx and Rx antenna, according to the following formula:

$$Pr = Ad^{-\gamma}, \tag{5.1}$$

which in logarithmic scale transforms to:

$$Pr_{[dB]} = A_{[dB]} - \gamma 10 \log_{10}(d). \tag{5.2}$$

From the measured data, the model coefficients were extracted.

Figure 5.11 shows the received power as a function of the distance for scenarios 1, 2 and 3. These scenarios were with both antennas over a desk at 97 cm above the floor. Scenarios 1 and 2 were in LOS and scenario 3 was with the computer display between both antennas.

---

[1] Overlap Time Interval

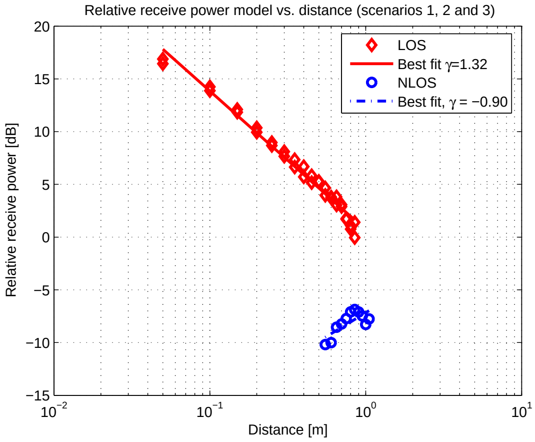

Figure 5.11: Relative received power vs. distance

The path loss exponent in LOS situations is 1.32, that means that the received

Table 5.1: Measurement description

	Num. measurements		Antenna height (cm)		Orientation		
Scenario	LOS	NLOS	Tx	Rx	MDR	Polarity	Obstructing object
1	17	---	97	97	yes	V	---
2	17	---	97	97	yes	V	---
3	---	11	97	97	yes	V	Computer display
4	---	12	21-65	97	no	V	Table
5	---	12	11-55	97	yes	H	Table
6	---	21	21	97	no	V	Table
7	20	---	21-135	97	some	V	---
8	20		21-135	97	some	V	Table/metal drawer
9	12	---	120	120	yes	V	---
10	---	12	120	120	yes	V	Body

power decreases with distance but it decreases slower than in free space (path loss exponent equal to 2). This is mainly due to two reasons. One of them is due to the multipath components reaching receive antenna (wave-guide effect). Another effect is the near field effect modelled in section 4.1. This effect introduces extra losses for short distances, this in turn means that received power will decrease with distance slower than in free space.

It can be seen that for LOS situations the received power does not fit perfectly to a straight line due to the near field effect. The exponential model in section 4.1 can be used in order to obtain a better fit. Figure 5.12 shows the measured data from scenarios 1 and 2 and the best fit of the model in equation (5.2) and the exponential model.

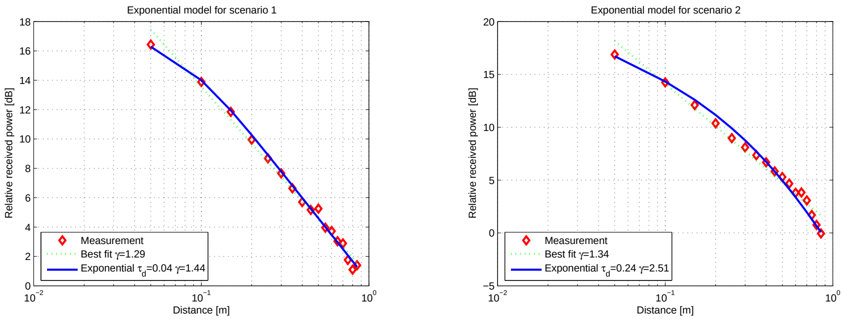

Figure 5.12: Exponential path loss model

Also the variation of the path loss exponent with the bandwidth was analyzed. A center frequency of 6.5 GHz was fixed and the path loss exponent was calculated for different bandwidths around this center frequency. Figure 5.13 shows the results.

As it was expected, the path loss exponent is almost the same for different bandwidths. Only a small variation is observed for NLOS situations.

The variations of the path loss exponent with the frequency for a fixed bandwidth of 1 GHz is also analyzed. A flat path loss exponent is expected. Figure 5.14 shows the results.

LOS situations have a flat path loss exponent for all the frequencies, but path loss exponent for NLOS situations increase with the frequency. In scenario 3, a computer monitor was placed between both antennas. Receive antenna was placed quite close to the monitor, that means that direct path was completely blocked. In this situation, only reflections of the objects surrounding the scenario reached the antenna. The fact that for high frequencies the path loss exponent is higher means that some reflection reached the antenna when the distance was small, only for high frequencies. This can be explained because the different behavior of the reflectors

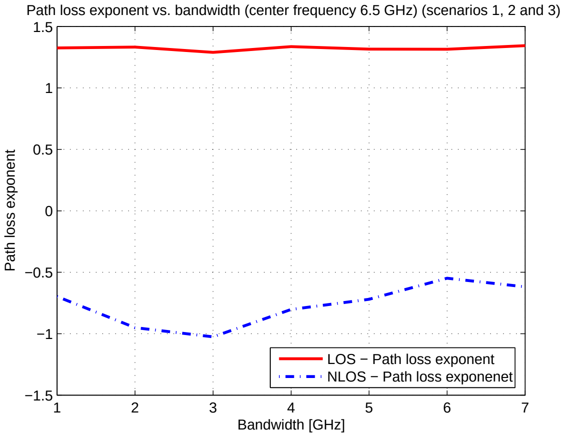

Figure 5.13: Path loss exponent vs. bandwidth

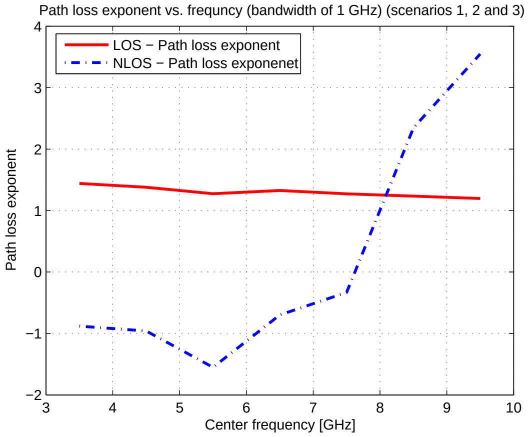

Figure 5.14: Path loss exponent vs. frequency

with the frequency. Some materials may reflect high frequencies better than low frequencies.

In scenarios 4, 5 and 6 the transmit antenna was placed behind the desktop while receive antenna was kept fixed on the desk. In scenario 5, the antennas were placed horizontally, in this way the maximum direction of radiation was directed to each other. In scenarios 4 and 6 the antennas were placed vertically. Transmit antenna (under the desk) was moved vertically. Figure 5.15 shows the variation of the relative received power as a function of the distance. A path loss exponent of 0.6 and 0.32 was found for DMR and N-DMR situation (DMR means that the direction of maximum radiation was directed to the other antenna). It can be seen that the dependence with the distance is stronger for the DMR situation, this is because the direct path is reaching receive antenna through the table. Usually, the path loss exponent for NLOS situations is higher than 2 (path loss of free space). In short distances the behavior is not the same. For short distances, when the direct path is blocked, most of the energy is reaching the antenna from far reflectors (far compared with the distance between antennas). This cause that when the distance between antennas is incremented, the received power does not change very much, and in extreme situations the received power can be higher even for large distances.

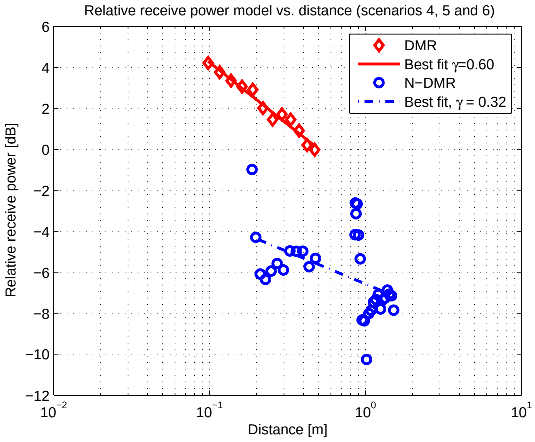

Figure 5.15: Relative received power vs. distance

Another effect can be observed in figure 5.15. The N-DMR situations can be easily divided into two subgroups (scenario 4 and 6). It can be seen that the smallest distances of each subgroup have more energy than the large distances. This can be explained because of the radiation pattern of the antennas. In this situations, the receive antenna was fixed on the desk at 97 cm above the floor, while the transmit antenna was moved vertically. The bi-conical antennas used have an omni-directional radiation pattern in the horizontal plane, so for short distances, the situation of the antennas was approximate to a DMR situation, and then a higher received power was measured.

Figure 5.16 shows the variations of the path loss exponent with the bandwidth.

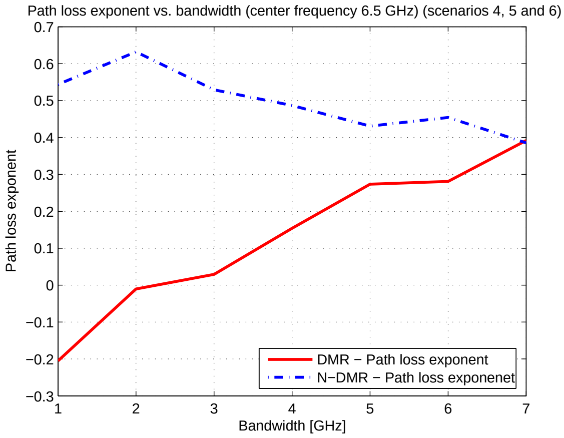

Figure 5.16: Path loss exponent vs. bandwidth

In this situation an almost flat path loss exponent as a function of the bandwidth is measured for the N-DMR situations, but for the DMR situation, it tends to increase with the bandwidth.

Figure 5.17 shows the path loss exponent as a function of the frequency. In this figure it can be seen that in the DMR situation, the path loss exponent is higher for low frequencies and almost zero for high frequencies. This mean that for high frequencies the direct path is completely blocked and the power reaching the antenna was from objects far away from the antennas (maybe the wall). For low frequencies the path loss is about 0.6, that mean that low frequencies can penetrate the wood better than high frequencies.

Figure 5.18 shows the relative received power as a function of transmit antenna height for scenarios 7 and 8. In these scenarios, receive antenna was fixed on the desk at 97 cm while transmit antenna was moved vertically from the ground until 1.35 cm. In scenario 7 both antennas were placed in LOS, but in scenario 8, the antennas were placed in a manner that they would be in LOS or NLOS depending on the height of transmit antenna.

It can be seen that for large heights both situations become LOS and the received power is almost the same. For a height larger than 1 m the received power decreases, but the distance between the antennas is almost the same. This is because of the radiation pattern of the antennas.

Figure 5.19 shows the relative received power as a function of the distance for scenarios 9 and 10. In scenario 10 a human body was obstructing the direct path.

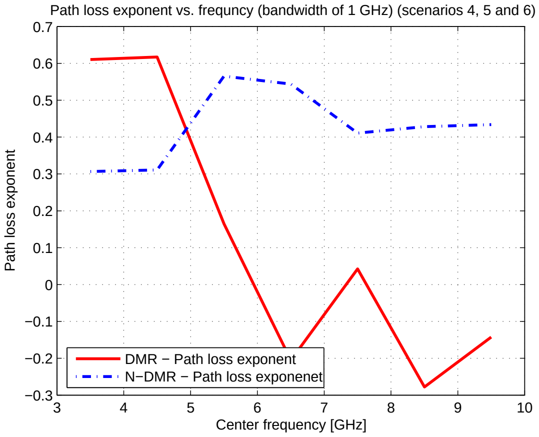

Figure 5.17: Path loss exponent vs. frequency

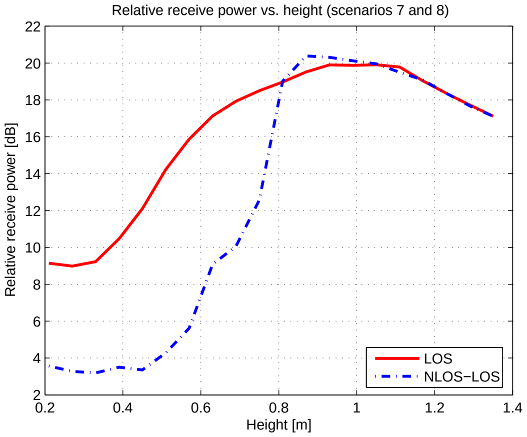

Figure 5.18: Relative received power vs. height

In scenario 9 the antennas were in the same position as in scenario 10 but without any object obstructing the direct path.

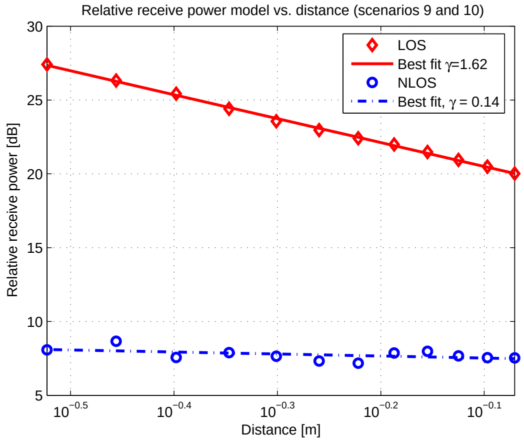

Figure 5.19: Relative received power vs. distance

A path loss exponent of 1.62 and 0.14 are found for LOS and NLOS situations. As before, a path loss exponent smaller than 2 for LOS situations is due to the power picked up by receive antenna from walls and objects added to the direct path, and also to the near field effect. For NLOS situation, the power reaching the antenna is coming from reflections on the wall (situated at more than 1 m), that means that the received power from the reflections is almost the same for different distances (path loss exponent near zero).

Figure 5.20 shows the variation of the path loss exponent with the bandwidth. As it was expected the path loss exponent is almost flat.

The path loss exponent as a function of the frequency is shown in figure 5.21. For LOS situation, the path loss exponent does not vary with frequency, but for NLOS situation it has some variations. It means that the penetration of the obstructing object is different for different frequencies.

5.4.2 K-factor

Rician K-factor is defined as the ratio of the power from the dominant path to the power from other paths.

Figure 5.22 shows the CDF of the K factor for scenarios 1, 2 and 3. As it was expected, the K factor for LOS situations is higher than for NLOS situations. The high difference between LOS and NLOS values is because for very short distances

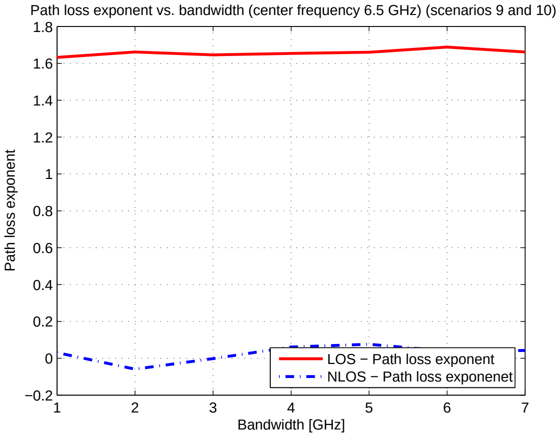

Figure 5.20: Path loss exponent vs. bandwidth

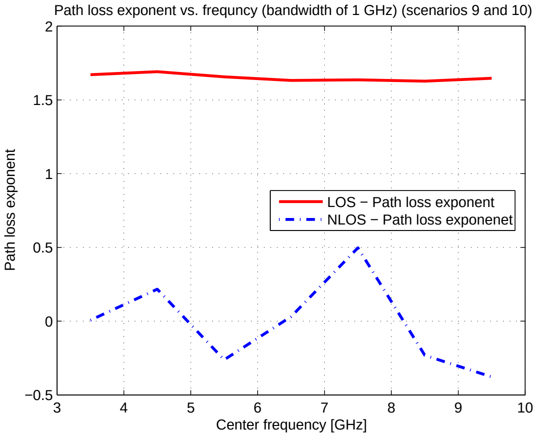

Figure 5.21: Path loss exponent vs. frequency

in LOS situations, the direct path is very strong compared to the reflections from reflectors far away compared to the distance between the antennas.

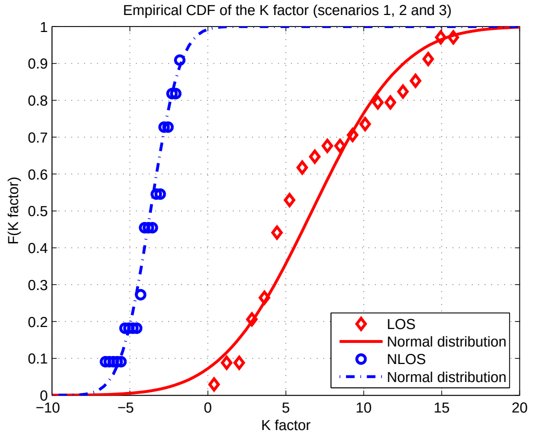

Figure 5.22: CDF of the K factor

Figure 5.23 shows the variation of the K factor with the distance between the antennas. For LOS situations, the K factor decreases with the distance, this is the normal behavior because the number of reflected paths is higher for large distances, and the power in the direct path is lower. For NLOS situations, the behavior is in the other way around. The K factor increases with the distance. Assuming that the direct path is completely blocked, a higher K factor for large distances means that for large distances, one of the multipath reflections is higher than the rest.

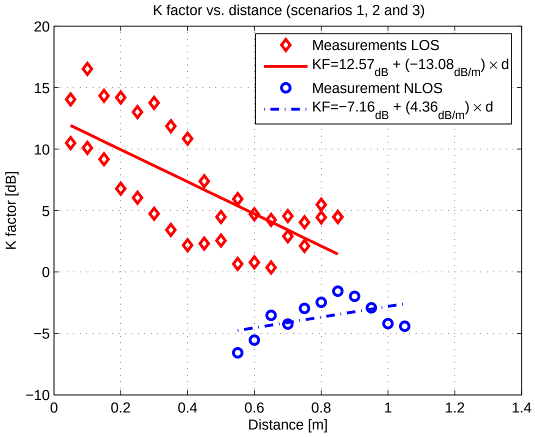

Figure 5.23: Variation of the K factor vs. distance

Figure 5.24 shows the CDF of the K factor for scenarios 4, 5 and 6. It can be seen that the K factor is about 5 dB for DMR situations (NLOS situations but with the maximum direction of radiation of the antennas directed to each other). That means that the direct path is reaching receive antenna through the table and it is quite strong compared to the reflections.

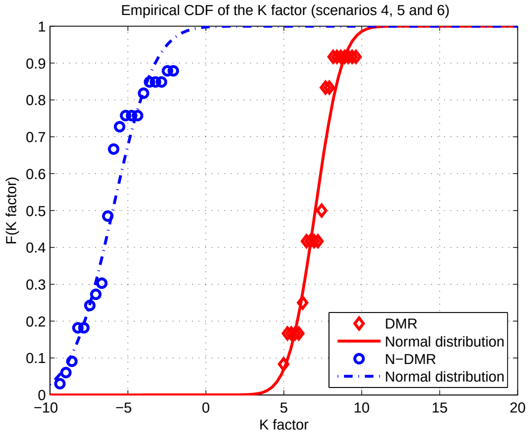

Figure 5.24: CDF of the K factor

The variation of the K factor with the distance for this situation is shown in figure 5.25. The variation of the K factor for DMR situations is as it was expected. It decrease with the distance. For N-DMR situations, there is no correlation between the K factor and the distance.

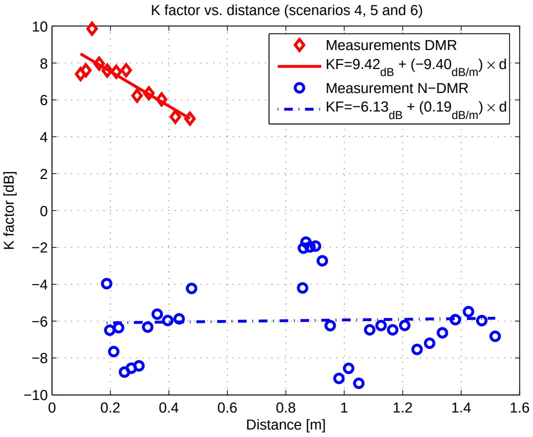

Figure 5.25: Variation of the K factor vs. distance

For scenarios 9 and 10 the CDF of the K factor is shown in figure 5.26. It can be seen that for LOS situations, the K factor is quite high, this means that in this situation the reflections were quite low compared to the direct path. This is normal, because the walls were more than 1 m far away from antennas and also no objects near the antennas were placed. For NLOS situations the K factor is about -5 dB.

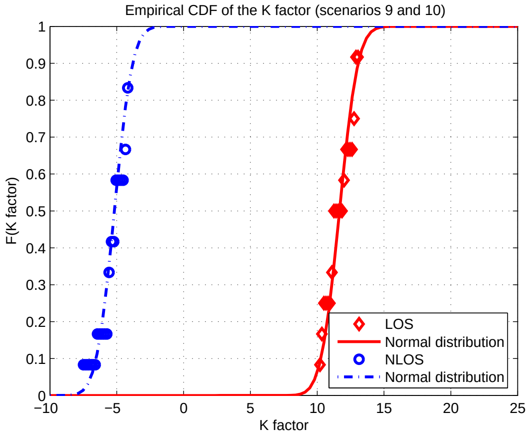

Figure 5.26: CDF of the K factor

Again, the K factor decreases with the distance for LOS situations. For NLOS the K factor tends to increase with the distance.

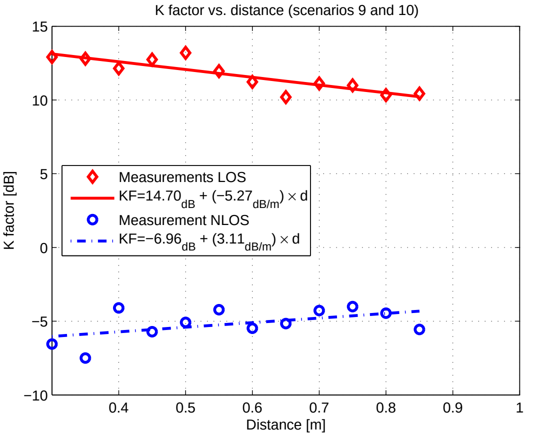

Figure 5.27: Variation of the K factor vs. distance

5.4.3 RMS delay spread

In this sub-section, RMS delay spread results are presented.

Figure 5.28 shows the CDF of the RMS delay spread for scenarios 1, 2 and 3. For LOS situations, the RMS delay spread is about 2.5 ns. For NLOS situations is about 4 times higher.

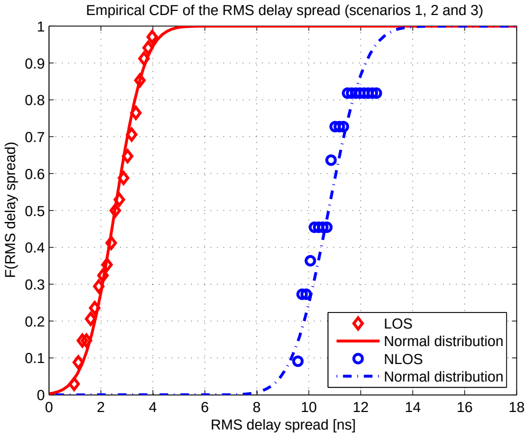

Figure 5.28: CDF of the RMS delay spread

The variation of the RMS delay spread with the distance is shown in figure 5.29. For LOS situations, the RMS delay spread increases with distance, but for NLOS situations it decreases with distance. That means, that for very short distances, when the antennas are very close to the obstructing object, the reflections are coming from far reflectors. When the antennas are separated from the obstructing object, some strong reflections may appear, and this provoke a higher K factor and lower RMS delay spread.

Figures 5.30 and 5.31 show the RMS delay spread for scenarios 4, 5 and 6. As it was expected, the RMS delay spread is higher for N-DMR situations, and it tends to increase with the distance. For N-DMR situations, a strange behavior can be observed for the different scenarios (distances higher than 0.7 m belong to one scenario and distances smaller than 0.7 m belong to the other one). This behavior is the same as that seen in the path loss exponent for these scenarios, and it is due to the radiation pattern of the antennas.

Finally, the RMS delay spread for scenarios 9 and 10 is shown in figures 5.32 and 5.33. In LOS situation, the RMS delay spread increase with the distance, but in NLOS, its variation is negligible.

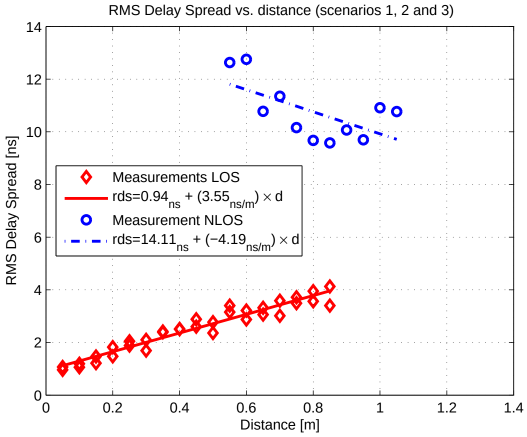

Figure 5.29: Variation of the RMS delay spread vs. distance

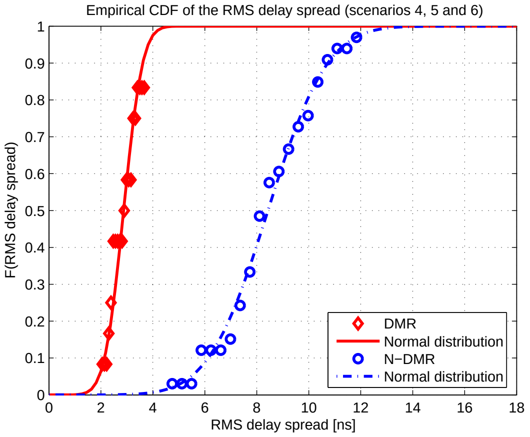

Figure 5.30: CDF of the RMS delay spread

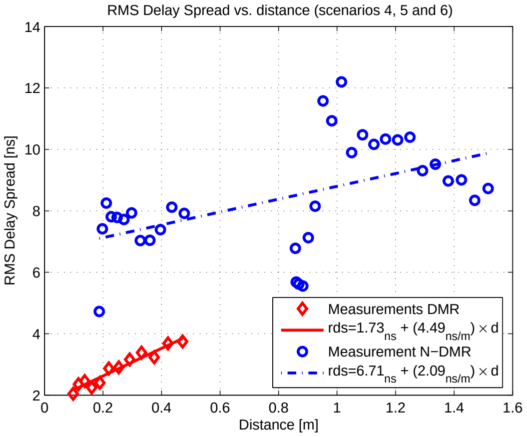

Figure 5.31: Variation of the RMS delay spread vs. distance

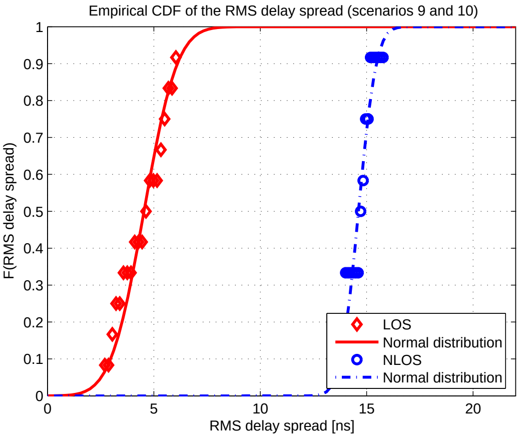

Figure 5.32: CDF of the RMS delay spread

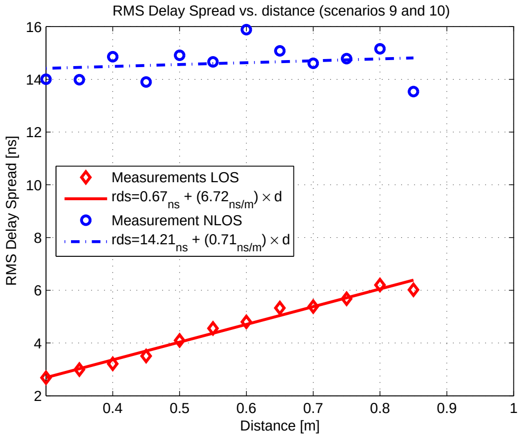

Figure 5.33: Variation of the RMS delay spread vs. distance

Chapter 6

Conclusions and Future Work

6.1 Conclusions

In this thesis, the transmission of UWB signals for very short distances have been analyzed. Different near field effects have been presented, and its repercussions on the UWB transmission are explained. Namely, these effects are multiple reflections between antennas, phase error and reactive fields.

The former can cause a distortion of the received signal that depends on the distance between the antennas. The second one, the phase error, may cause a link budget variation and a pulse waveform distortion due to the variations of the antenna gain for short distances. Finally, the absorption of the reactive fields surrounding the antennas in the near field, may cause a mismatching of the antennas.

For the antennas used in the measurements, bi-conical antennas of different sizes, the multiple reflections between the antennas and the mismatching caused by the absorption of reactive fields can be neglected. The main effect observed in the measurements is the phase error. This effect causes a link budget variation and a pulse waveform distortion.

The link budget variations are stronger for large antennas, this agree with the phase error effect. The pulse waveform distortion in frequency domain is located around the frequencies with "deeps" in the far field, that also agree with the phase error.

The devices used in WPAN applications are laptops, mobile phones and PDA's, among others. For this kind of devices the antennas used have to be small antennas, so the link budget variations would be negligible. As the pulse waveform distortion can be avoided using a filter (analogical or digital filter), no serious problems are expected due to the near field.

However, for different kinds of antennas the near field effects can have a different behavior, and then, the effects that for the bi-conical antennas used in the measurements are negligible, maybe for other antennas become important.

As regards the channel parameters, the main conclusion is that for NLOS situations and short distances, the variations of the RMS delay spread, K factor and path loss is quite small with the distance.

For LOS situations, an elegant extension of the free space path loss model to the near field conditions has been developed and it can be used in order to get a better approximation of the path loss for these situations.

Finally, a publication based on this work has been accepted for presentation [20] at the European Conference on Wireless Technology (ECWT) 2005.

6.2 Future Work

The effects of the near field on the transmission has been investigated and they have shown a strong dependency on the antenna type. All the measurements in this thesis have been done using different kinds of bi-conical antennas. It would be interesting to analyze the effect for different kinds of antennas in order to obtain the characteristics that makes an antenna more suitable for UWB near field transmission.

In this work the radio channel properties for distances from 1 m to 1 cm have been analyzed. For some applications data transmission for distances smaller than 10 cm can be useful. For such applications, it can be interesting to explore the capacitive or inductive coupling (only reactive fields), in order to no interfere with close objects and also to increase security (making difficult the traffic sniffing). The analysis of the properties for this channel can be quite different from the radio channel investigated in this thesis, and it would be an attractive task.

When several multipath components reach the antenna at the same time is not possible to deconvolve them using only a deconvolution algorithm as CLEAN or ESPRIT. One idea in order to deconvolve these multipath components is to use beamforming. In this way several multipath components reaching the antenna at the same time can be separated as a function of their angle of arrival. Usually the beamforming algorithms assume that the antennas are situated in the far field, and the angle of arrival for all the antennas in the array is the same, but for the near field this is not true. A modification of a beamforming algorithm in order to work in the near field region would be useful for this issue.

Bibliography

[1] (2005) FCC regulations, updates and changes adopted and released by the Commissions as of april 5, 2005. [Online]. Available: http://www.fcc.gov/oet/info/rules/part15/part15_4_05_05.pdf 2

[2] Z. Irahhauten, H. Nikookar, and G. Janssen, "Literature survey on the ultra-wideband wireless channel models," March 2003. 2

[3] A. H. Muqaibel, A. Safaai-Jazi, A. M. Attiya, A. Bayram, and R. S. M, "Measurement and characterization of indoor ultra-wideband propagation," in *IEEE Conference on Ultra Wideband Systems and Technologies*. IEEE, November 2003, pp. 295–299. 3

[4] T. B. Welch, R. L. Musselman, B. A. Emessiene, P. D. Gift, D. K. Choudhury, D. N. Cassadine, and S. M. Yano, "The effects of the human body on UWB signal propagation in an indoor enviroment," *IEEE Journal on Selected Areas in Communications*, pp. 1778–1782, December 2003. 3

[5] T. Zasowski, F. Althaus, M. Stäger, A. Wittneben, and G. Tröster, "UWB for noninvasive wireless body area networks: channel measurements and results," in *IEEE Conference on Ultra Wideband Systems and Technologies*. IEEE, November 2003, pp. 285–289. 3

[6] D. Cassioli, M. A. Win, and A. F. Molisch, "A statistical model for the uwb indoor channel," in *Vehicular Technology Conference, 2001. VTC 2001 Spring. IEEE VTS 53rd*, vol. 2. IEEE, May 2001, pp. 1159–1163. 8

[7] S. M. Yano, "Investigating the ultra-wideband indoor wireless channel," in *Vehicular Technology Conference, 2002. VTC Spring 2002. IEEE 55th*, vol. 3. IEEE, 2002, pp. 1200–1204. 8

[8] J. R. Foerster, M. Pendergrass, and A. F. Molisch, "A channel model for ultra wideband indoor communication," 26/02/2005. 8

[9] S. Ghassemzadeh, R. Jana, C. Rice, W. Turin, and V. Tarokh, "A statistical path loss model for in-home uwb channels," in *Ultra Wideband Systems and*

Technologies, 2002. Digest of Papers. 2002 IEEE Conference on. IEEE, May 2002, pp. 59–64. 9

[10] M. Dohler, B. Allen, A. Armogida, S. McGregor, M. Ghavami, and H. Aghvami, “A new twist on uwb pathloss modeling,” in *Vehicular Technology Conference, 2004. VTC 2004-Spring. 2004 IEEE 59th*, vol. 1. IEEE, May 2004, pp. 199–203. 9

[11] H. G. Schantz, “Introduction to ultra-wideband antennas,” in *Ultra Wideband Systems and Technologies, 2003 IEEE Conference on.* IEEE, November 2003, pp. 1–9. 10, 11

[12] C. A. Balanis, *Antenna Theory Analysis and Design*, 2nd ed. John Wiley & Sons, INC, 1997. 12, 13, 14, 36, 41, 42, 43, 44, 56, 67

[13] C. R. Paul and S. A. Nasar, *Introduction to Electromagnetic Fields*, 2nd ed. McGraw-Hill, 1987. 12

[14] J. D. Kraus, *Antennas*, ser. Electrical and Electronic Engineering Series. McGraw-Hill, 1950. 19

[15] X.-Y. Cao, G.-X. Dai, S.-C. Zhen, and J. Gao, “The mutual coupling between horns in the near-field,” in *Microwave and Millimeter Wave Technology Proceedings, ICMMT ’98. 1998 International Conference on.* IEEE, August 1998, pp. 357–359. 20, 22

[16] R. Schmitt, *Electromagnetics Explained.* Newnes, 2002. 57, 59

[17] D. Cassioli, M. Z. Win, and A. F. Molisch, “The ultra-wide bandwidth indoor channel: from statistical model to simulations,” *IEEE Journal on Selected Areas in Communications*, vol. 20, no. 6, pp. 1247–1257, August 2002. 71

[18] Z. Irahhauten, A. Yarovoy, H. Nikookar, G. J. M. Janssen, and L. Ligthart, “Measurement setup for ultra wide band indoor radio channel characterization,” in *IEEE, 11th Symposium on Communications and Vehicular Technology (SCVT).* IEEE, November 2004. 80

[19] R. G. Vaughan and N. L. Scott, “Super-resolution of pulsed multipath channels for delay spread characterization,” *IEEE Transaction on Communications*, vol. 47, no. 3, pp. 781–785, March 1999. 80, 106

[20] Z. Irahhauten, J. Dacuña Santos, G. J. M. Janssen, and H. Nikookar, “UWB channel measurements and modeling for wireless personal area networks applications,” in *European Conference on Wireless Technology (ECWT) 2005.* IEEE, Accepted for publication. 98

[21] A. van der Veen, *Signal Processing for Communications.* Delft University of Technology, Department of Electrical Engineering, Circuits and Systems, 2004. 104

Appendix A

Algorithms comparison

In order to obtain some important parameters of the transmission channel (as the RMS delay spread, K factor, etc...), the channel impulse response has to be obtained. To measure the channel the impulse response, an infinite bandwidth pulse (mathematically called δ) has to be sent. This kind of pulse is not feasible, and a finite bandwidth pulse has to be used.

This chapter presents a comparison between different deconvolution algorithms that can be used in order to obtain the channel impulse response from the channel measurements.

Section A.1 gives a brief description of the problem. Section A.2 describes some deconvolution algorithms. Section A.3 shows the results of the simulations carried out with different algorithms. Finally in section A.4 some conclusions are extracted.

A.1 Introduction

Assuming that the channel behaviour has model

$$h(t) = \sum_{i=1}^{N} a_i \delta(t - \tau_i), \tag{A.1}$$

where N is the number of multipath components and a_i and τ_i are the amplitude and time of arrival of the ith multipath component. Then the received signal will be

$$r(t) = p(t) * h(t) = \sum_{i=1}^{N} a_i p(t - \tau_i), \tag{A.2}$$

where $p(t)$ is the pulse shape of the sent impulse and $*$ denotes convolution.

The channel impulse response $h(t)$ can be obtained from the received signal $r(t)$ using the Fourier transform.

$$R(f) = P(f)H(f), \tag{A.3}$$

where $R(f)$, $P(f)$ and $H(f)$ are the Fourier transforms of $r(t)$, $p(t)$ and $h(t)$, respectively. From A.3, the estimation of the channel impulse response $h'(t)$ can be obtained as

$$h'(t) = \mathscr{F}^{-1}\left\{\frac{R(f)}{P(f)}\right\}, \tag{A.4}$$

where $\mathscr{F}^{-1}$ denotes inverse Fourier transform.

This method is known as "Inverse filtering" The problem of this method is that $P(f)$ can be zero or a very low value for several frequencies. This will cause the noise in $R(f)$ blow up and in turn a not precise impulse channel response $h'(t)$. An illustration of this effect is shown in figures A.1, A.2 and A.3.

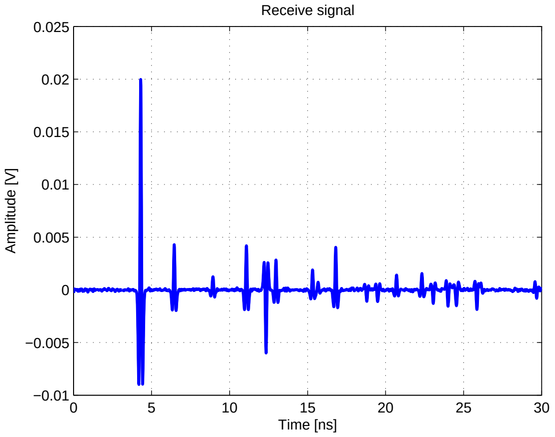

Figure A.1: Simulation of the channel response. The sent pulse is a second derivative of the Gaussian pulse.

A.2 Algorithms description

In this section several deconvolution algorithms will be explained, namely "ESPRIT", "CLEAN" and an extension of the inverse filtering used in the example in section A.2 that uses also "CLEAN" algorithm, it will be called "INV+CLEAN" in this report.

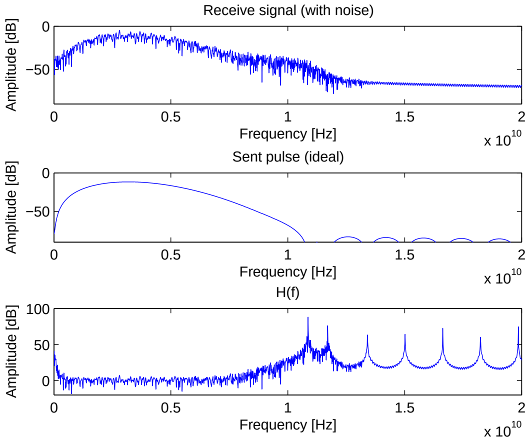

Figure A.2: Fourier transform of the received signal (up), sent pulse (middle) and channel response (bottom)

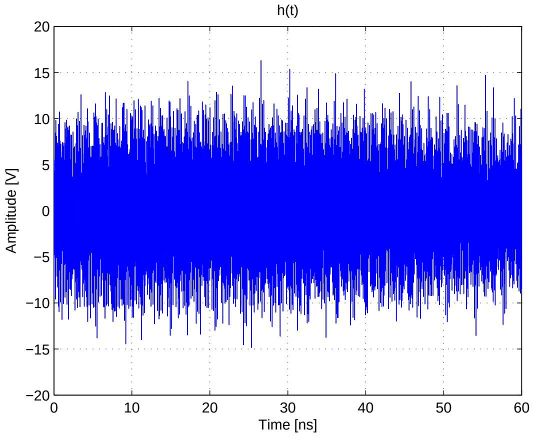

Figure A.3: Noisy channel response obtained using the inverse filtering algorithm

A.2.1 ESPRIT algorithm

In this part a brief explanation of the ESPRIT algorithm is given. A deeper explanation of this algorithms can be found in [21]. ESPRIT algorithm is an estimation algorithm based on the phase of the signal. It can be used to estimate the DOA[1], the multipah delay and spectral frequencies. Here it is explained the delay estimation with a single antenna.

Consider a multipath channel which consists of N delayed copies of $p(t)$, as it was explained in section A.1, so the impulse response is

$$r(t) = \sum_{i=1}^{N} a_i p(t-\tau_i) \qquad \Leftrightarrow$$

$$\mathbf{r} = \sum_{i=1}^{N} \mathbf{p}_{\tau_i} a_i = [\mathbf{p}_{\tau_1}, \cdots, \mathbf{p}_{\tau_N}] \begin{bmatrix} a_1 \\ \vdots \\ a_N \end{bmatrix} =: \mathbf{P}_\tau \mathbf{a}. \tag{A.5}$$

This is the same as in equation A.2 but expressed in a different form. Both $r(t)$ and $p(t)$ are known. The unknowns are the parameters τ_i and a_i. The objective is to estimate these parameters. ESPRIT allows to obtain the τ_i parameters, while the a_i parameters will be estimated from τ_i using the auto-correlation and cross-correlation functions of the reference pulse $p(t)$ and the received signal $r(t)$.

First of all we will define $\tilde{\mathbf{p}}$ as the DFT[2] of $\mathbf{p}$

$$\tilde{\mathbf{p}} = \mathscr{F}\mathbf{p}, \tag{A.6}$$

were $\mathscr{F}$ denotes the DFT matrix of size L (the length of the pulse), defined by

$$\mathscr{F} := \begin{bmatrix} 1 & 1 & \cdots & 1 \\ 1 & \phi & \cdots & \phi^{L-1} \\ \vdots & \vdots & \ddots & \vdots \\ 1 & \phi^{L-1} & \cdots & \phi^{(L-1)^2} \end{bmatrix}, \quad \phi = e^{-j\frac{2\pi}{L}}. \tag{A.7}$$

To avoid the problem explained in section A.1, a selection matrix $\mathbf{J}_{\tilde{p}} : LW \times L$ is defined as

$$\mathbf{J}_{\tilde{p}} = \begin{bmatrix} 0 & \cdots & 0 & I_{LW} & 0 & \cdots & 0 \end{bmatrix} : \quad LW \times L, \tag{A.8}$$

were LW is the number of samples of the DFT greater than a given threshold.

Now we define the vector $\mathbf{z}$ as

$$\mathbf{z} := \{\mathrm{diag}(\mathbf{J}_{\tilde{p}}\tilde{\mathbf{p}})\}^{-1} \mathbf{J}_{\tilde{p}} \mathscr{F}\mathbf{h}, \qquad (LW \times 1). \tag{A.9}$$

---

[1] Direction of Arrival

[2] Discrete Fourier Transform

The vector $\mathbf{z}$ has model

$$\mathbf{z} = \mathbf{F}\mathbf{a}, \qquad \mathbf{F} = [\mathbf{f}(\phi_1), \cdots, \mathbf{f}(\phi_r)], \qquad \mathbf{f}(\phi) := \begin{bmatrix} 1 \\ \phi \\ \phi^2 \\ \vdots \\ \phi^{LW-1} \end{bmatrix}. \tag{A.10}$$

Since there are multiple components in $\mathbf{F}$ and only a single vector $\mathbf{z}$ is not possible to estimate several components from it. In order to do it, and using the shift-invariance property of the vectors $\mathbf{f}()$ it is possible to construct a matrix $\mathbf{Z}$ from $\mathbf{z}$ as

$$\mathbf{Z} = \left[\mathbf{z}^{(0)}, \mathbf{z}^{(1)}, \cdots, \mathbf{z}^{(m-1)}\right],$$
$$(LW - m + 1 \times m), \qquad \mathbf{z}^{(i)} := \begin{bmatrix} z_{i+1} \\ z_{i+2} \\ \vdots \\ z_{LW-m+i} \end{bmatrix}. \tag{A.11}$$

where $\mathbf{z}^{(i)}$ is a subvector of $\mathbf{z}$ containing the $i+1$-st til the $LW-m+i$-th entry. The maximum number of multipath components that can be detected is m. Now split $\mathbf{Z}$ into $\mathbf{X}$ and $\mathbf{Y}$,

$$\mathbf{Z} = \left[\frac{\mathbf{X}}{***}\right] = \left[\frac{***}{\mathbf{Y}}\right] \tag{A.12}$$

where $\mathbf{X}$ contains all but the last rows of $\mathbf{Z}$, and $\mathbf{Y}$ contains all but the first rows. Now we compute the eigenvalue decomposition

$$\mathbf{X}^{\dagger}\mathbf{Y} = \mathbf{T}^{-1}\mathbf{\Phi}\mathbf{T}. \tag{A.13}$$

This determines $\Phi := [e^{j2\pi\tau_1/L}, e^{j2\pi\tau_2/L}, \cdots, e^{j2\pi\tau_N/L}]$ as the eigenvalues of $\mathbf{X}^{\dagger}\mathbf{Y}$, from which the delays $\{\tau_i\}$ can be estimated.

Now the delays of each multipath components are estimated, but still the amplitudes $\{a_i\}$ need to be estimated. The amplitudes will be estimated from the cross-correlation between the pulse $p(t)$ and the receive signal $r(t)$ divided by the auto-correlation of the pulse $p(t)$,

$$a_i = \frac{R_{rp}(\tau_i)}{R_{pp}(0)}, \tag{A.14}$$

where

$$R_{rp}(m) = E\{r_n y_{n-m}\}, \quad \text{and} \tag{A.15}$$

$$R_{pp}(m) = E\{r_n r_{n-m}\}, \tag{A.16}$$

where $E\{\cdot\}$ denotes the expected value operator.

A.2.2 CLEAN algorithm

CLEAN algorithm is an iterative algorithm based on the iterative substraction of the pulse in a dirty map initialized with the received signal. The detailed procedure is as follows [19]:

1. initialize the dirty map with $d(t) = \mathrm{Re}\{r(t)\}$ and the clean map with $c(t) = 0$;
2. from the correlation coefficient function $\Gamma(\tau) = p(t) \odot d(t)$ (normalization understood and $\odot$ means correlation);
3. find peaks, Γ_i, and their positions, τ_i, in $\Gamma(\tau)$;
4. if all $\Gamma_i <$ threshold, stop;
5. clean the dirty map by $d(t) = d(t) - \Gamma_i p(t - \tau_i)$;
6. update the clean map by $c(t) = c(t) + \Gamma_i \delta(t - \tau_i)$;
7. jump to step 2 until stop;
8. the estimated impulse response is then $h'(t) = c(t)$.

A.2.3 INV+CLEAN algorithm

This algorithm is the result of a combination of inverse filtering introduced in section A.1 and CLEAN algorithm described in section A.2.2. The main idea of this method is to use the inverse filtering only for that parts of the spectrum which the power of the reference pulse $p(t)$ is not zero (higher than a given threshold). The rest of the spectrum is filled with zeros (using a rectangular window). This cause that the estimation of the channel impulse response in equation (A.4) is a convolution of the channel impulse response and a rectangular window in frequency domain (a sinc function in time domain).

$$h''(t) = \mathscr{F}^{-1}\left\{\frac{R(f)}{P(f)}W(f)\right\}, \tag{A.17}$$

where $W(f)$ is a rectangular window. Then $h''(t)$ is

$$h''(t) = h'(t) * w(t), \tag{A.18}$$

now, in order to obtain the estimation of the channel impulse response $h'(t)$ from $h''(t)$, the CLEAN algorithm described in section A.2.2 using $h''(t)$ as the receive signal $r(t)$ and $w(t)$ as the pulse reference $p(t)$ has to be applied.

A.3 Simulations

Different simulations to asses the performance of each algorithm (CLEAN, INV+CLEAN and ESPRIT) have been performed. In this section the results of these simulations are presented.

This section is organized in four subsections, one for each simulation (with and without noise and coarse and dense multipath).

A.3.1 Coarse multipath without noise

Simulations with one thousand of different simulated channels have been done in order to obtain the empirical CDF[3] of the most important channel parameters namely, the RDS[4], Ricean K factor, number of multipath components and total received power.

In this case, the simulated channel has an arrival rate of 1 multipath component per nanosecond, a Ricean K factor of 0 (Raileygh channel) and a RDS of 10 ns.

The CDF of the RMS delay spread can be seen in figure A.4. The CDF of RMS delay spread is almost the same for all the algorithms, and they fit very well with the real CDF. A threshold of 50 dB has been used, this mean that only the multipath components until 50 dB under the stronger path are taken into account.

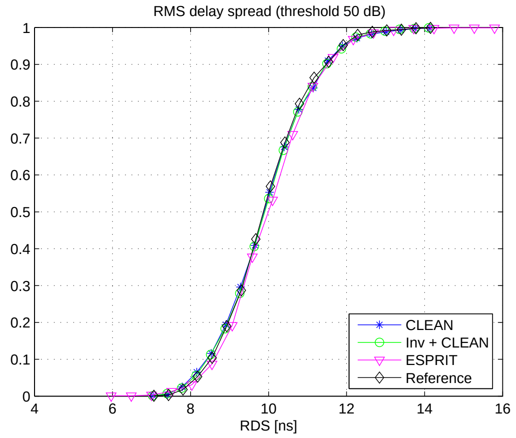

Figure A.4: Simulated CDF of RMS delay spread, for a threshold of 50 dB

The K factor is shown in figure A.5. The difference between the real value and the approximation of the algorithms is about 1 dB.

---

[3] Cumulative Distribution Function

[4] Root-mean-square Delay Spread

The number of paths is shown in figure A.6. CLEAN is the better algorithm to estimate the number of paths in this situation. The others algorithm give a higher number of multipath components detected (about 50 % higher than the real).

In figure A.7 the total received power is shown. As in the case of the RMS delay spread, all the algorithms converge to the real value.

The RMS delay spread and the total receive power is almost the same for all the algorithms. The main differences are in the number of detected paths and the K factor. This is because the extra detected multipath components have very low power.

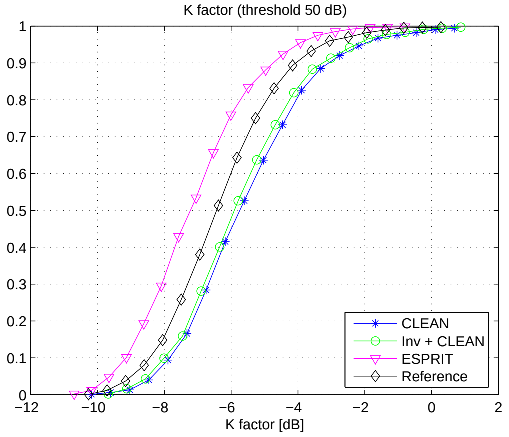

Figure A.5: Simulated CDF of K factor, for a threshold of 50 dB

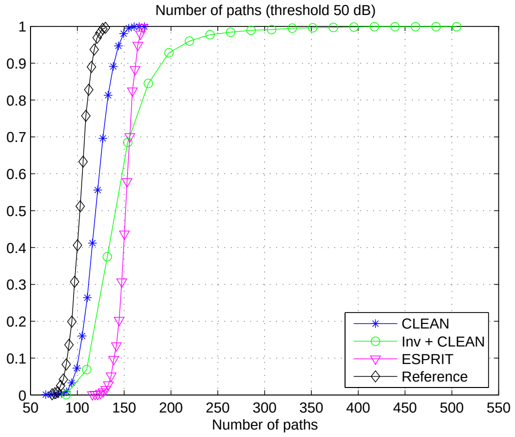

Figure A.6: Simulated CDF of number of paths, for a threshold of 50 dB

The mean value of these parameters (RMS delay spread, K factor, number of paths and total received power) as a function of the threshold give us the better threshold to estimate the parameters without detect extra paths.

The RMS delay spread as a function of the threshold is shown in figure A.8. It can be seen that for a threshold higher than 35 dB, all the algorithms have no variations. This is normal because multipath components below 30 dB have no contribution in the RMS delay spread.

The K factor as a function of the threshold is shown in figure A.9. For a threshold higher than 25 dB, the variations of the algorithms are negligible.

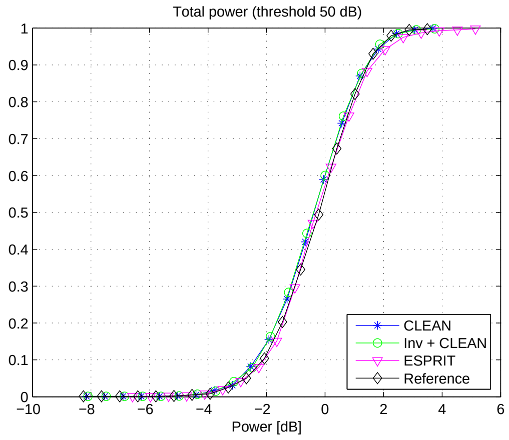

Figure A.7: Simulated CDF of total received power, for a threshold of 50 dB

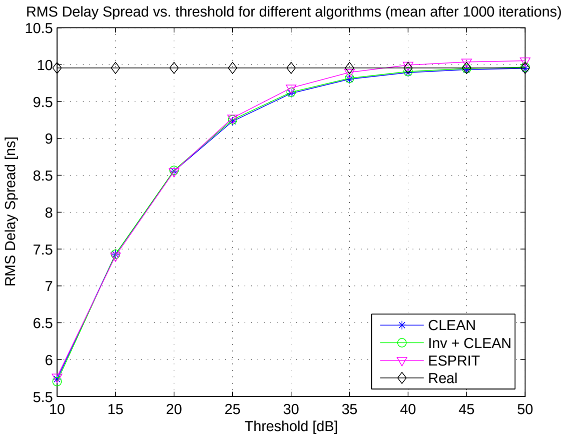

Figure A.8: RMS delay spread as a function of the threshold

The number of paths as a function of the threshold is as it was expected, the higher the threshold, the higher the number of multipath components detected. However, for higher threshold the multipath components is higher than the real number of paths. Figure A.10 shows this behavior.

The variations of the total received power for a threshold higher than 25 dB is negligible. ESPRIT algorithm gives a value slightly higher than the real one while CLEAN and Inv+CLEAN give a result slightly lower than the real one.

A summary of all the values (mean and variance) of each parameter for all the algorithms and thresholds is shown in table A.1.

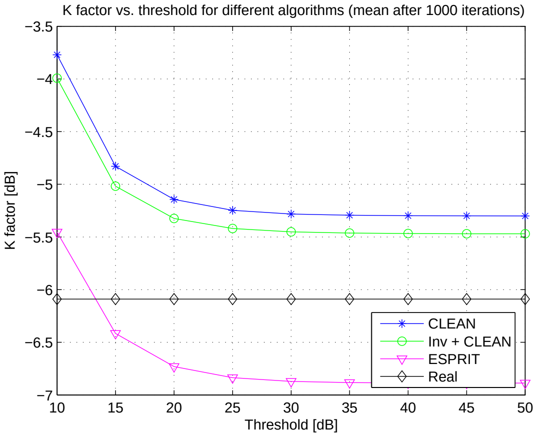

Figure A.9: K factor as a function of the threshold

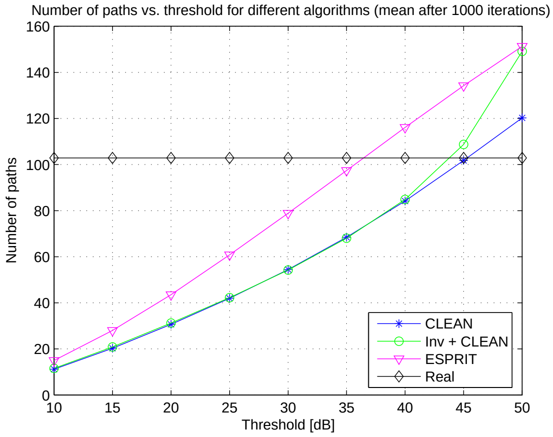

Figure A.10: Number of paths as a function of the threshold

Table A.1: Simulation results for coarse multipath without noise

	Thr.	RDS [ns]		K fac. [dB]		Num paths		Power [dB]	
Alg.	[dB]	Mean	σ	Mean	σ	Mean	σ	Mean	σ
Real	—	9.96	1.12	-6.09	-19.37	102.87	10.16	-0.05	-5.00
	50	9.95	1.18	-5.30	-17.70	120.26	14.50	-0.15	-4.91
	45	9.93	1.18	-5.30	-17.70	101.76	13.17	-0.15	-4.91
C	40	9.89	1.19	-5.30	-17.69	84.20	11.57	-0.15	-4.91
L	35	9.80	1.20	-5.29	-17.68	68.47	9.92	-0.16	-4.92
E	30	9.61	1.21	-5.28	-17.64	54.45	8.47	-0.17	-4.93
A	25	9.23	1.25	-5.25	-17.52	41.95	7.34	-0.19	-4.96
N	20	8.56	1.32	-5.14	-17.15	30.64	6.29	-0.26	-5.04
	15	7.43	1.44	-4.83	-16.04	20.28	5.40	-0.45	-5.26
	10	5.74	1.70	-3.77	-11.87	11.19	4.05	-1.04	-5.85
I	50	9.97	1.17	-5.47	-18.02	149.11	37.61	-0.17	-4.95
n	45	9.95	1.17	-5.47	-18.02	108.73	16.44	-0.17	-4.95
v	40	9.91	1.18	-5.47	-18.02	84.85	11.76	-0.17	-4.95
+	35	9.82	1.18	-5.46	-18.00	68.04	9.73	-0.18	-4.95
C	30	9.63	1.20	-5.45	-17.96	54.23	8.23	-0.19	-4.96
L	25	9.25	1.23	-5.42	-17.85	42.25	7.22	-0.21	-4.99
E	20	8.57	1.30	-5.32	-17.52	31.23	6.19	-0.27	-5.06
A	15	7.43	1.41	-5.02	-16.30	20.87	5.38	-0.46	-5.27
N	10	5.70	1.65	-3.99	-12.41	11.55	4.08	-1.05	-5.81
	50	10.05	1.15	-6.89	-20.51	151.33	8.77	0.06	-4.24
E	45	10.04	1.15	-6.89	-20.51	134.24	9.76	0.06	-4.24
S	40	9.99	1.16	-6.89	-20.50	116.10	9.93	0.05	-4.24
P	35	9.90	1.17	-6.88	-20.49	97.41	9.55	0.05	-4.25
R	30	9.69	1.19	-6.87	-20.45	78.87	9.42	0.04	-4.26
I	25	9.28	1.24	-6.84	-20.33	60.83	8.85	0.02	-4.29
T	20	8.55	1.33	-6.73	-19.96	43.55	8.08	-0.06	-4.38
	15	7.41	1.48	-6.42	-18.84	28.02	6.89	-0.28	-4.59
	10	5.76	1.75	-5.45	-15.72	14.99	5.19	-0.92	-5.15

A.3.2 Coarse multipath with noise

The same simulation done in section A.3.1 is repeated in this section, but adding white Gaussian noise. The signal to noise ratio (SNR) is 20 dB and it is defined as the ratio of the energy of all the received signal to the energy of the noise.

The rest of the parameters of the channel are exactly the same, RDS of 10 ns, Ricean K factor of 0 and arrival rate of 1 multipath component per ns.

The CDF of the RMS delay spread is shown in figure A.12. It can be seen that for this situation, the better fit is given by CLEAN algorithm.

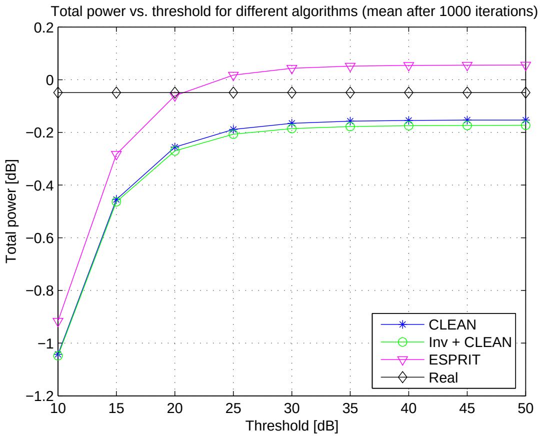

Figure A.11: Total power as a function of the threshold

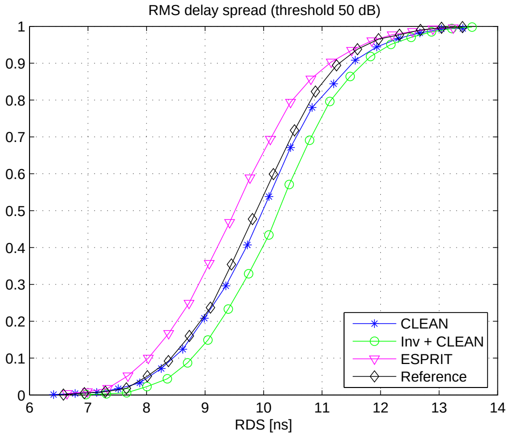

Figure A.12: Simulated CDF of RMS delay spread, for a threshold of 50 dB

The K factor is shown in figure A.13. The result of all the algorithms is almost the same and it is less than 1 dB higher than the reference.

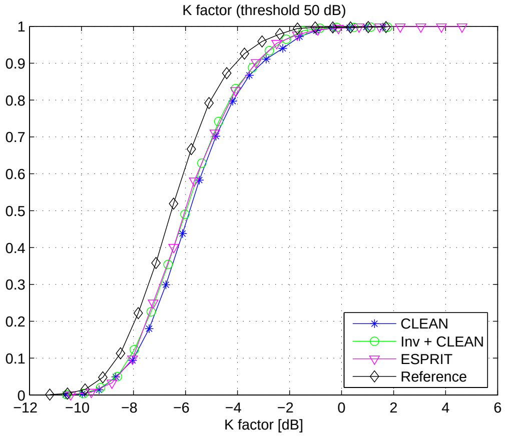

Figure A.13: Simulated CDF of K factor, for a threshold of 50 dB

In figure A.14 the CDF of the number of paths is shown. The better result is given by the ESPRIT algorithm. Algorithms based in CLEAN detect a lot of extra multipath components due to the noise. This extra paths have very low power because they have negligible effect in the estimation of the RDS, K factor and also the received power.

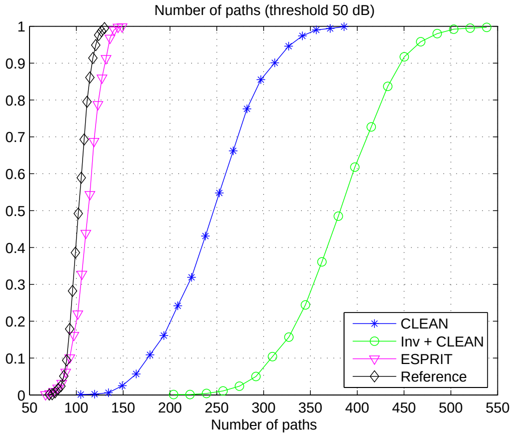

Figure A.14: Simulated CDF of number of paths, for a threshold of 50 dB

The total received power is shown in figure A.15. It can be seen that all the algorithms give a good fit with the reference, but the better result is given by the

CLEAN based algorithms.

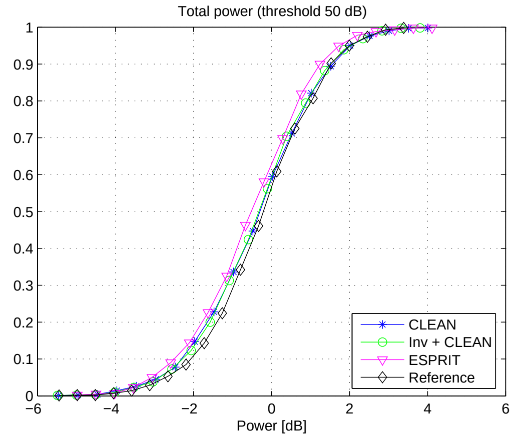

Figure A.15: Simulated CDF of total received power, for a threshold of 50 dB

The mean values of the RMS delay spread as a function of the threshold is shown in figure A.16. The variations of the algorithms for a threshold higher than 40 dB is negligible (except for Inv+CLEAN algorithm).

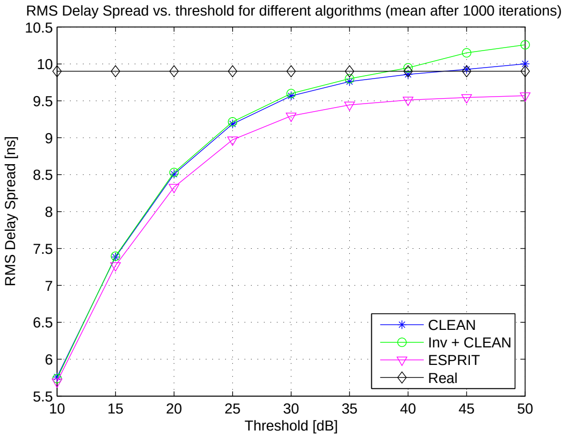

Figure A.16: RMS delay spread as a function of the threshold

The variation in the K factor (figure A.17) for a threshold higher than 25 dB is negligible.

In figure A.18 it can be seen that the number of detected paths in CLEAN based algorithms blow up drastically for a threshold higher 40 dB. That means that the detected paths under 40 dB are due mainly to the noise.

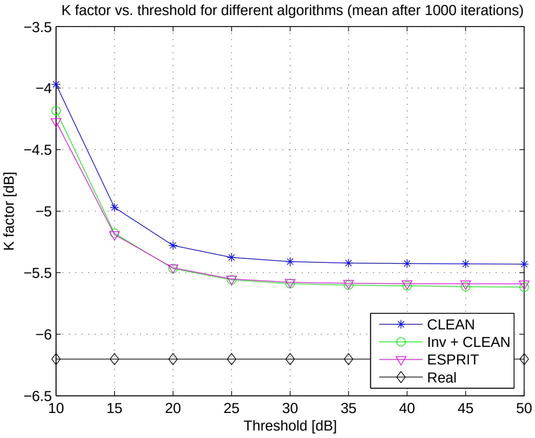

Figure A.17: K factor as a function of the threshold

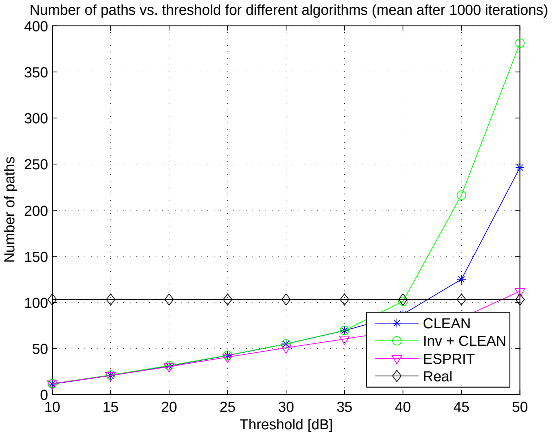

Figure A.18: Number of paths as a function of the threshold

For a threshold higher than 30 dB the received power is the same. This is shown in figure A.19.

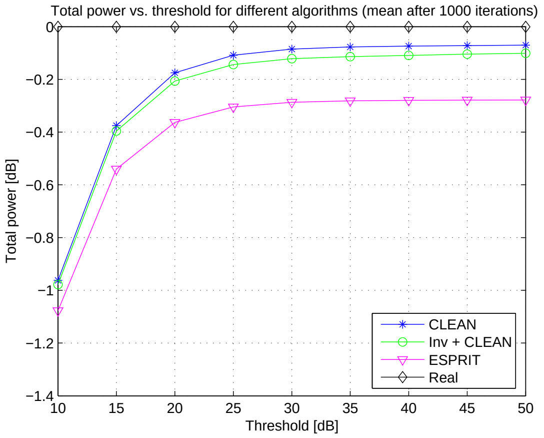

Figure A.19: Total power as a function of the threshold

A summary of all the values (mean and variance) of each parameter for all the algorithms and thresholds is shown in table A.2.

A.3.3 Dense multipath without noise

In this section the same simulations as before are exposed, but for a dense multipath environment. In this case an arrival rate of 5 multipath components per nanosecond is fixed. The other channel parameters are K factor of 0, RMS delay spread of 10 ns and no noise.

Esprit algorithm is limited by the m parameter in equation A.11. In these simulation this parameter is fixed to 200, so the maximum number of detected paths is 200. In this environment the number of multipath components is expected to be higher than 200, so the performance of ESPRIT algorithm in this situation will be limited.

The CDF of the RMS delay spread is shown in figure A.20. CLEAN based algorithms give the best fit to the reference.

In figure A.21 the CDF of the K factor is shown. Again CLEAN based algorithms give the best approximation to the reference; namely Inv+CLEAN gives the best fit.

As was to be expected, the number of paths detected by ESPRIT algorithm is at the most 200 (due to the limitation imposed). All the algorithms give a number of detected paths smaller than the reference, but the better approximation is given by Inv+CLEAN.

Table A.2: Simulation results for coarse multipath with noise

	Thr.	RDS [ns]		K fac. [dB]		Num paths		Power [dB]	
Alg.	[dB]	Mean	σ	Mean	σ	Mean	σ	Mean	σ
Real	—	9.90	1.13	-6.20	-19.31	103.06	10.49	-0.00	-4.89
	50	10.00	1.20	-5.43	-17.97	246.24	50.30	-0.07	-4.63
	45	9.93	1.21	-5.43	-17.96	125.02	26.94	-0.07	-4.63
C	40	9.86	1.22	-5.43	-17.96	87.12	12.58	-0.07	-4.64
L	35	9.76	1.23	-5.42	-17.95	69.35	10.15	-0.08	-4.64
E	30	9.57	1.25	-5.41	-17.91	55.00	8.62	-0.09	-4.65
A	25	9.19	1.30	-5.38	-17.80	42.37	7.51	-0.11	-4.68
N	20	8.51	1.39	-5.28	-17.50	30.95	6.36	-0.18	-4.77
	15	7.38	1.51	-4.97	-16.39	20.57	5.34	-0.38	-5.02
	10	5.76	1.77	-3.97	-13.04	11.36	4.08	-0.96	-5.63
I	50	10.26	1.13	-5.62	-18.43	381.23	53.28	-0.10	-4.78
n	45	10.15	1.15	-5.61	-18.42	216.43	52.44	-0.10	-4.78
v	40	9.95	1.19	-5.61	-18.41	101.14	22.90	-0.11	-4.79
+	35	9.80	1.20	-5.60	-18.39	69.60	10.24	-0.11	-4.79
C	30	9.60	1.23	-5.59	-18.36	55.00	8.39	-0.12	-4.80
L	25	9.22	1.27	-5.56	-18.25	42.62	7.33	-0.14	-4.83
E	20	8.53	1.35	-5.47	-17.94	31.51	6.31	-0.21	-4.91
A	15	7.40	1.46	-5.18	-16.94	21.20	5.40	-0.40	-5.13
N	10	5.74	1.74	-4.18	-13.10	11.84	4.25	-0.98	-5.72
	50	9.57	1.21	-5.59	-18.01	112.12	14.22	-0.28	-4.96
E	45	9.55	1.21	-5.59	-18.01	83.11	10.33	-0.28	-4.96
S	40	9.51	1.22	-5.59	-18.01	70.14	8.25	-0.28	-4.96
P	35	9.44	1.22	-5.59	-18.00	60.24	7.73	-0.28	-4.96
R	30	9.30	1.24	-5.58	-17.96	50.64	7.27	-0.29	-4.97
I	25	8.97	1.27	-5.55	-17.84	40.68	6.75	-0.30	-4.99
T	20	8.33	1.34	-5.46	-17.36	30.36	6.02	-0.36	-5.05
	15	7.27	1.47	-5.19	-16.46	20.64	5.30	-0.54	-5.25
	10	5.69	1.68	-4.27	-13.36	11.77	4.12	-1.08	-5.71

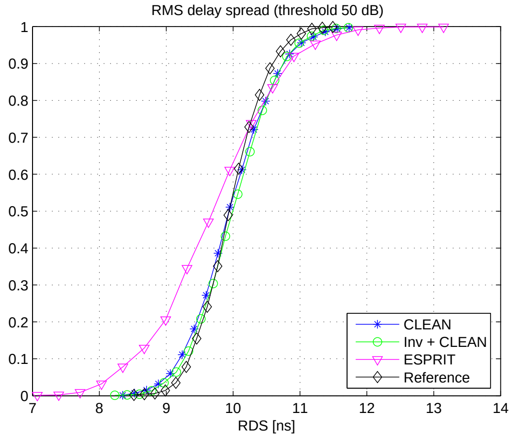

Figure A.20: Simulated CDF of RMS delay spread, for a threshold of 50 dB

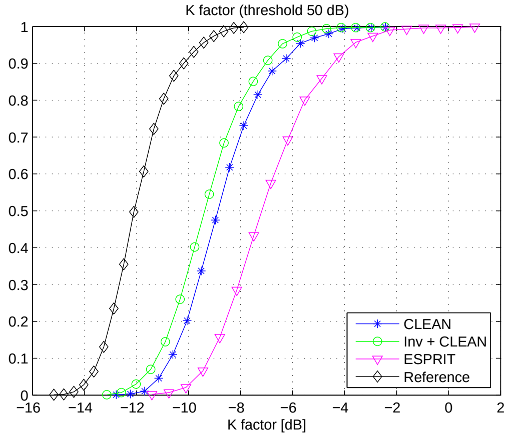

Figure A.21: Simulated CDF of K factor, for a threshold of 50 dB

In figure A.23 the CDF of the total received power is shown. The best fit is given by CLEAN based algorithms. ESPRIT algorithm give a value lower than the real one due to the limitation imposed in the maximum number of detected paths.

The mean value of the RMS delay spread as a function of the threhold is shown in figure A.24. For a threshold higher than 40 dB there are no variations in the value. It can be seen also that the better approximation is given by CLEAN based algorithms.

The mean value of the K factor does not vary for thresholds higher than 30 dB. The better aproximation is given by Inv+CLEAN algorithm, but is almost 3 dB higher than the real value.

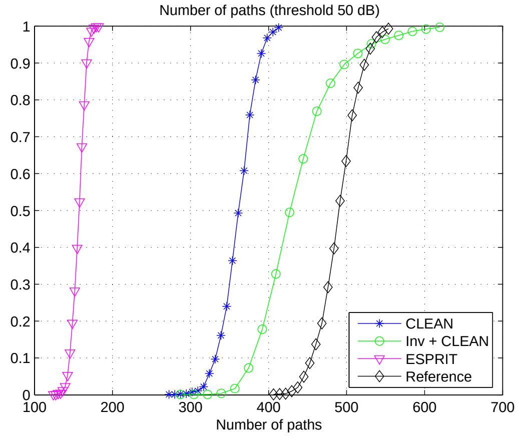

Figure A.22: Simulated CDF of number of paths, for a threshold of 50 dB

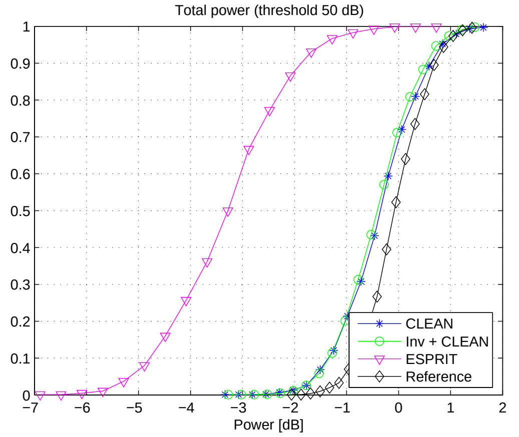

Figure A.23: Simulated CDF of total power, for a threshold of 50 dB

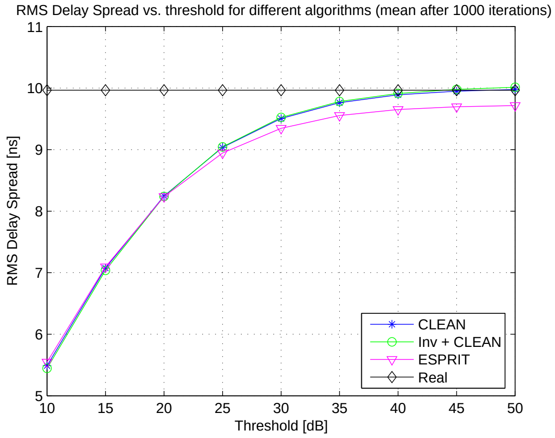

Figure A.24: RMS delay spread as a function of the threshold

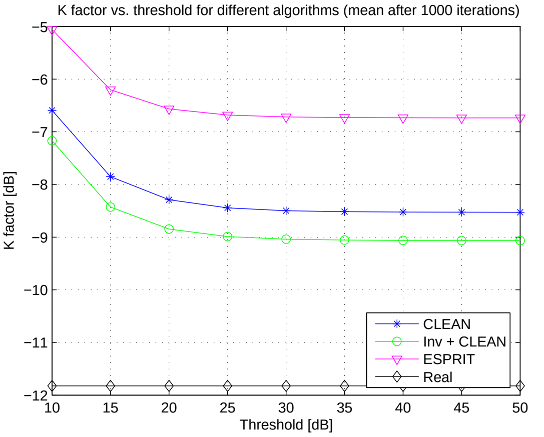

Figure A.25: K factor as a function of the threshold

The number of multipath components detected as a function of the threshold is shown in figure A.26. All the algorithms give a number of detected paths lower than the real. ESPRIT algorithm is limited to 200 multipaths components.

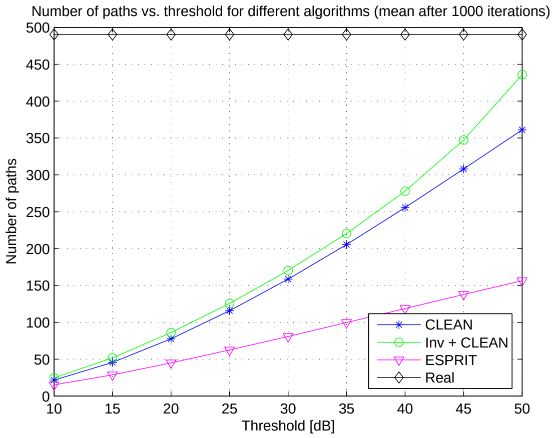

Figure A.26: Number of paths as a function of the threshold

The total received power as a function of the threshold can be seen in figure A.27. For thresholds higher than 25 dB the total power does not vary. It can be seen also that for ESPRIT algorithm the value is almost 3 dB lower than for CLEAN based algorithms. This is due to the limitation imposed in the maximum number of detected paths.

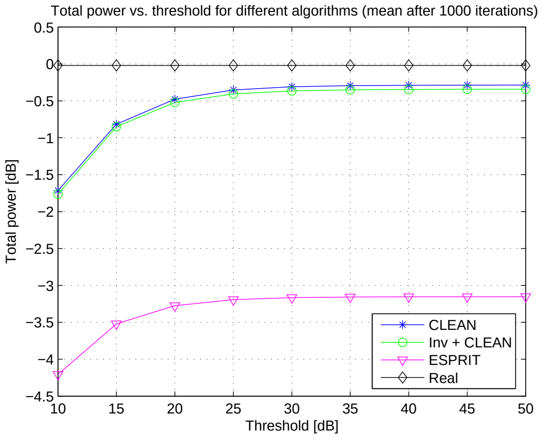

Figure A.27: Total power as a function of the threshold

A summary of all the values (mean and variance) of each parameter for all the algorithms and thresholds is shown in table A.3.

Table A.3: Simulation results for dense multipath without noise

	Thr.	RDS [ns]		K fac. [dB]		Num paths		Power [dB]	
Alg.	[dB]	Mean	σ	Mean	σ	Mean	σ	Mean	σ
Real	—	9.97	0.48	-11.82	-28.20	490.28	26.04	-0.02	-8.67
	50	9.98	0.61	-8.53	-22.45	361.01	21.77	-0.29	-7.91
	45	9.95	0.61	-8.53	-22.45	307.98	21.73	-0.29	-7.91
C	40	9.89	0.61	-8.52	-22.44	255.56	20.68	-0.29	-7.91
L	35	9.76	0.63	-8.52	-22.42	205.54	19.32	-0.29	-7.92
E	30	9.51	0.65	-8.50	-22.35	158.58	17.51	-0.31	-7.94
A	25	9.04	0.71	-8.44	-22.18	115.71	15.48	-0.35	-8.01
N	20	8.25	0.81	-8.29	-21.68	77.61	13.35	-0.48	-8.18
	15	7.08	0.95	-7.85	-20.31	45.72	10.61	-0.82	-8.56
	10	5.49	1.19	-6.59	-16.56	21.61	7.35	-1.72	-8.99
I	50	10.01	0.58	-9.07	-23.10	435.76	49.73	-0.34	-8.18
n	45	9.98	0.58	-9.06	-23.09	347.28	31.46	-0.34	-8.18
v	40	9.91	0.58	-9.06	-23.09	277.86	24.45	-0.35	-8.19
+	35	9.78	0.59	-9.06	-23.07	220.37	21.19	-0.35	-8.19
C	30	9.52	0.62	-9.04	-23.01	170.22	18.56	-0.36	-8.22
L	25	9.05	0.67	-8.99	-22.85	125.63	16.29	-0.41	-8.28
E	20	8.24	0.77	-8.85	-22.37	86.02	14.05	-0.52	-8.44
A	15	7.04	0.91	-8.43	-20.98	51.81	11.72	-0.85	-8.80
N	10	5.44	1.12	-7.17	-16.55	24.69	8.32	-1.76	-9.24
	50	9.72	0.90	-6.74	-19.37	156.43	8.65	-3.15	-8.94
E	45	9.70	0.91	-6.74	-19.36	137.78	9.23	-3.15	-8.94
S	40	9.65	0.91	-6.73	-19.36	118.60	9.48	-3.15	-8.94
P	35	9.55	0.93	-6.73	-19.34	99.66	9.15	-3.16	-8.95
R	30	9.35	0.95	-6.72	-19.30	80.86	9.08	-3.17	-8.96
I	25	8.95	1.01	-6.68	-19.16	62.56	8.70	-3.19	-9.00
T	20	8.24	1.12	-6.57	-18.75	45.05	8.16	-3.27	-9.10
	15	7.09	1.31	-6.20	-17.27	28.75	7.29	-3.52	-9.37
	10	5.55	1.62	-5.06	-12.76	15.10	5.48	-4.21	-9.85

A.3.4 Dense multipath with noise

Now the simulations are repeated adding noise to the dense multipath channel of subsection A.3.3. The signal to noise ration (SNR) is, as in subsection A.3.2, of 20 dB. The rest of channel parameters are: arrival rate of 5 multipath components per nanosecond, Ricean K factor of 0 and RMS delay spread of 10 ns.

The CDF of the RMS delay spread is shown in figure A.28. For this situation, the best fit is given by CLEAN algorithm.

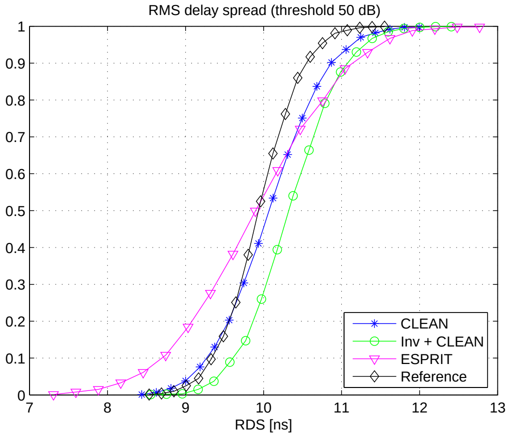

Figure A.28: Simulated CDF of RMS delay spread, for a threshold of 50 dB

On the other hand, the CDF of the K factor is shown in figure A.29. The better fit is also given by CLEAN based algorithms. The limitation imposed in ESPRIT algorithm (explained in subsection A.3.3) makes ESPRIT algorithms to fail in dense multipath environments.

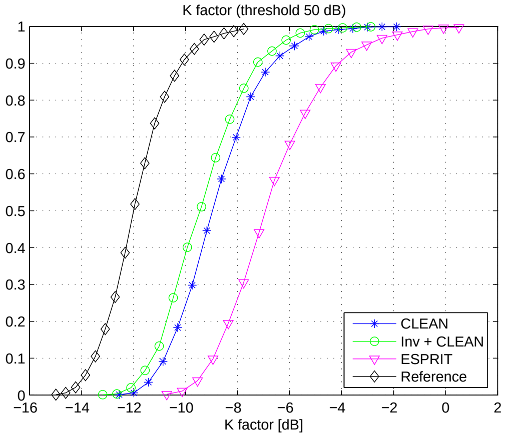

Figure A.29: Simulated CDF of K factor, for a threshold of 50 dB

Figure A.30 shows the CDF of the number of paths. The approximation of CLEAN based algorithms is good. It can be seen also the limitation of 200 detected paths for ESPRIT algorithm.

The CDF of the total received power is shown in figure A.31. As it was expected, the value given by ESPRIT algorithm is quite low with respect to the real value and the CLEAN based algorithms approximation due to the limitation imposed.

The mean value of the RMS delay spread as a function of the threshold is shown in figure A.32. For a threshold higher than 40 dB, the variation in the value given by all the algorithms does not vary.

The mean value of the K factor as a function of the threshold is shown in figure A.33. The K factor is stable for all the algorithms for thresholds higher than 25 dB.

The number of detected paths as a function of the threshold increase with the th-

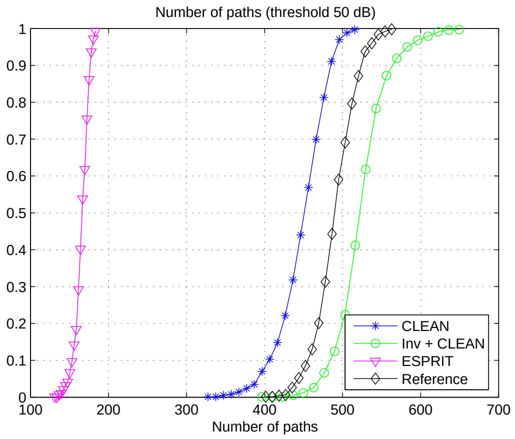

Figure A.30: Simulated CDF of number of paths, for a threshold of 50 dB

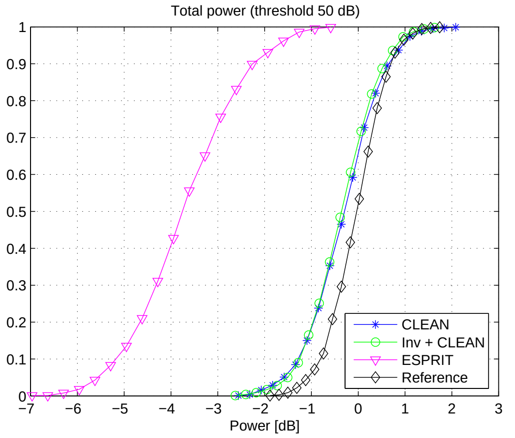

Figure A.31: Simulated CDF of total power, for a threshold of 50 dB

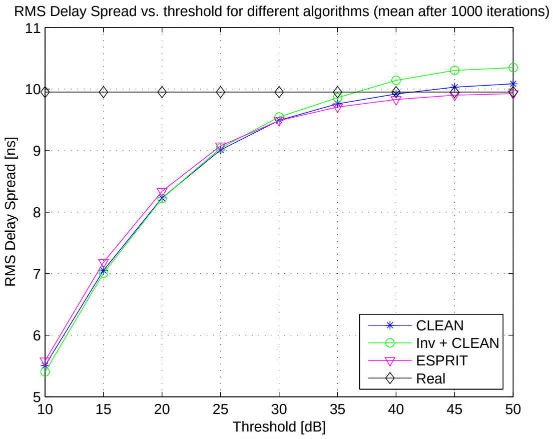

Figure A.32: RMS delay spread as a function of the threshold

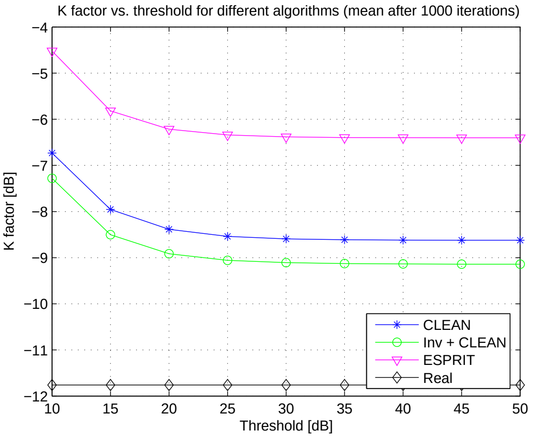

Figure A.33: K factor as a function of the threshold

reshold. This is shown in figure A.34.

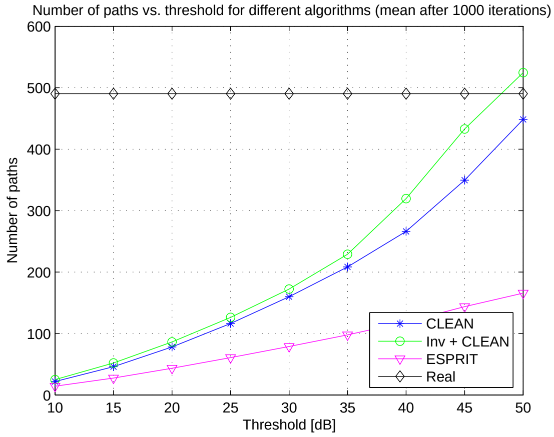

Figure A.34: Number of paths as a function of the threshold

Figure A.35 shows the total received power. For thresholds higher than 30 dB the total received power does not vary due to the low power of the detected paths (30 dB lower than the stronger one). As it was expected, the total received power given by ESPRIT algorithm is about 3 dB lower than the real one due to the aforementioned limitation.

A summary of all the values (mean and variance) of each parameter for all the algorithms and thresholds is shown in table A.4.

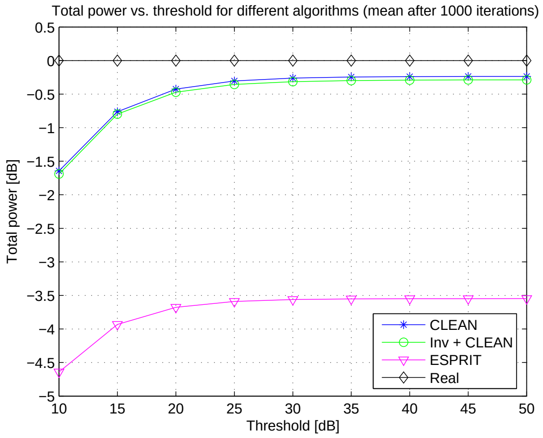

Figure A.35: Total power as a function of the threshold

Table A.4: Simulation results for dense multipath with noise

	Thr.	RDS [ns]		K fac. [dB]		Num paths		Power [dB]	
Alg.	[dB]	Mean	σ	Mean	σ	Mean	σ	Mean	σ
Real	—	9.95	0.47	-11.76	-27.67	490.39	26.44	-0.00	-8.67
	50	10.09	0.62	-8.62	-22.47	448.50	31.05	-0.24	-7.81
	45	10.03	0.63	-8.62	-22.47	349.58	33.09	-0.24	-7.81
C	40	9.92	0.64	-8.62	-22.46	266.18	24.53	-0.24	-7.81
L	35	9.76	0.65	-8.61	-22.44	208.40	20.15	-0.24	-7.82
E	30	9.49	0.68	-8.59	-22.37	159.97	18.31	-0.26	-7.85
A	25	9.01	0.74	-8.54	-22.19	116.36	16.16	-0.30	-7.91
N	20	8.23	0.83	-8.39	-21.71	78.26	13.74	-0.43	-8.09
	15	7.05	0.95	-7.96	-20.42	46.03	10.90	-0.76	-8.48
	10	5.50	1.16	-6.73	-16.45	21.82	7.40	-1.64	-8.97
I	50	10.35	0.56	-9.14	-23.18	524.62	33.03	-0.29	-8.15
n	45	10.30	0.57	-9.14	-23.17	432.86	36.05	-0.29	-8.15
v	40	10.14	0.59	-9.14	-23.16	319.55	35.90	-0.29	-8.15
+	35	9.86	0.61	-9.13	-23.14	229.08	24.24	-0.30	-8.17
C	30	9.55	0.63	-9.11	-23.08	172.36	18.90	-0.31	-8.19
L	25	9.04	0.68	-9.06	-22.92	126.34	16.59	-0.36	-8.25
E	20	8.22	0.77	-8.92	-22.48	86.34	14.05	-0.47	-8.39
A	15	7.01	0.91	-8.50	-21.12	51.99	11.85	-0.80	-8.75
N	10	5.40	1.09	-7.28	-17.13	25.01	8.38	-1.69	-9.14
	50	9.93	0.94	-6.40	-18.51	165.83	9.23	-3.55	-9.32
E	45	9.90	0.95	-6.40	-18.51	143.74	11.66	-3.55	-9.32
S	40	9.83	0.96	-6.40	-18.51	118.77	10.94	-3.55	-9.32
P	35	9.71	0.97	-6.40	-18.49	97.74	9.53	-3.55	-9.32
R	30	9.49	1.00	-6.38	-18.44	78.98	9.05	-3.56	-9.34
I	25	9.08	1.06	-6.34	-18.28	60.86	8.64	-3.59	-9.38
T	20	8.34	1.16	-6.22	-17.82	43.44	7.93	-3.68	-9.49
	15	7.19	1.35	-5.82	-16.21	27.53	7.03	-3.93	-9.78
	10	5.58	1.66	-4.52	-10.99	14.28	5.33	-4.64	-10.29

A.4 Conclusions

Simulations with different algorithms and channels have been done in section A.3. In this section some conclusions are given.

CLEAN algorithm gives, in general, the best approximation to the real value in all the situations simulated (dense and coarse multipath environments with and without noise).

It gives a good approximation to the RMS delay spread for all situations using a threshold of 40 dB. For estimate the K factor a threshold of 25 dB is enough and 30 dB for the total power.

The main problem of CLEAN is the estimated number of paths. It gives a number of paths that increase with the threshold mainly when the noise is not null. Due to this problem the number of paths maybe higher or lower than the real one depending of the noise and threshold. This problem in the number of paths estimation does not affect to the others parameters (RMS delay spread, K factor and total power) because the extra or missed paths are low power paths.

To obtain the better results in the simulations performed in section A.3, CLEAN algorithm using a threshold of 40 dB is the best choice.

The problem with ESPRIT is that it was limited to 200 paths in the simulations performed. For coarse multipath environments (about 100 multipath components in the simulations), ESPRIT gives also a good approximation, but its performance makes worse when the number of paths is increased. For this reason ESPRIT algorithm is not recommended if the approximate number of paths is not known.

Curriculum Vitae

Javier Dacuña Santos was born in Granollers, Spain, the 7th of March of 1981. In 2000 he began his studies at the *Universitat Politècnica de Catalunya* (UPC). He received his bachelor degree in Electrical Engineering speciality in Telecommunications Systems in 2003, and he obtain the first national price to the best academic expedient in Spain from the Education and Science Ministery (MEC). He was working as a programmer from 2002 to 2003 in Tempos 21, programming location applications for mobile devices.

In 2003 he started his MSc studies in Electrical Engineering at the *Universitat politècnica de Catalunya*. At the same time he was working in the Ubiquitous Systems Laboratory of the university in projects related to location, telemetry and radio frequency identification (RFID) involving tasks of programming, electronic circuit and antenna design.

In February 2005 he started his thesis project at Delft University of Technology (TU Delft), The Netherlands, in the Wireless Mobile Communications group under the supervision of prof. dr. ir. Gerard J.M. Janssen. His MSc thesis is entitled: “Statistical Characterization of UWB Channels for Wireless Personal Area Networks Applications”.

His research interests include: digital signal processing, artificial intelligence, location, telemetry and radio frequency identification.